

Design and Evaluation of Robust Control Methods for Robotic Transfemoral Prostheses

Nitish Thatte
April 12, 2019

The Robotics Institute
Carnegie Mellon University
Pittsburgh, PA 15213

Thesis Committee:
Hartmut Geyer (Chair)
Christopher Atkeson
Aaron Johnson
Steven Collins, Stanford University
Elliott Rouse, University of Michigan

*Submitted in partial fulfillment of the requirements
for the degree of Doctor of Philosophy*

Copyright ©2019 Nitish Thatte.

Abstract

Amputees face a number of gait deficits due to a lack of control and power from their mechanically-passive prostheses. Of crucial importance among these deficits are those related to balance, as falls and a fear of falling can cause an avoidance of activity that leads to further debilitation. In this thesis, we investigate the role that prosthesis control strategies play in maintaining balance with a powered robotic transfemoral prosthesis. Our approach involves comparing state-of-the-art prosthesis controllers on a common platform and learning from this experiment to propose two new prosthesis control strategies that directly address observed causes of falls in both the swing and stance phases.

We begin by designing and manufacturing our own powered transfemoral prosthesis capable of large torques for stumble recovery and accurate reproduction of desired torques from different control strategies. We also propose a pair of optimization methods that allow us to select prosthesis control parameters using qualitative preference feedback from the user.

Next, we test a hypothesis that a stance control approach based on a model of the human neuromuscular system may help improve gait robustness and user satisfaction over the commonly used impedance control method. This hypothesis stems from previous research applying neuromuscular control to simulated biped models and to powered ankle prostheses that suggest that this approach can adapt to changes in speed, incline, and rough ground. While our experiment did not find a significant reduction in falls using neuromuscular control, it did reveal that a lack of robust gait phase estimation caused a large number of falls for the impedance control strategy and that both controllers suffered from trips during swing.

Therefore, we next proposed and tested two new control strategies that directly address these causes of falls. In the first, we use information from an inertial measurement unit and LIDAR distance sensor to estimate the position, orientation and future trajectory of the hip. This information is then used to plan trajectories for the prosthesis' knee and ankle that avoid tripping during swing. Second, we pro-

pose using an extended Kalman filter to improve phase estimation during stance. We show the resulting control strategy significantly reduced the number of falls compared impedance control, when users are asked to step on uneven terrain. These results demonstrate the importance of state estimation for improving gait stability.

Acknowledgements

First, I would like to thank my advisor, Hartmut Geyer, for taking a chance and letting me pursue this line of research and for his mentorship and patience over the last six years. I would like to also thank my committee members Christopher Atkeson, Aaron Johnson, Steven Collins, and Elliott Rouse for their many helpful suggestions.

I would also like to thank my collaborators, Helei, Timothy, Nandagopal, Tanvi, and Alex, for assisting me with my research endeavors, and helping me keep the prosthesis and the lab in working order.

Thanks to my friends for making these years enjoyable despite the difficulties a PhD brings. Michael and Arun, thanks for being great roommates for so many years. Will and Akshara, thanks for the dinners at bad restaurants followed by even worse movies.

Thanks to my parents for their guidance early in my life that made this accomplishment possible.

And most of all, to my wife Jennifer, thank you for your love, companionship and support over the last ten years. Finishing this thesis would not have been possible without you.

Funding

This thesis contains work supported by a National Science Foundation Graduate Research Fellowship (grant number 0946825); a Robert Samson Graduate Fellowship; the Eunice Kennedy Shriver National Institute of Child Health & Human Development (award no. 1R01HD075492); the National Science Foundation (grant number 1527140)

Contents

1	<i>Introduction</i>	19
1.1	<i>Motivation</i>	19
1.2	<i>Challenges in Transfemoral Prosthesis Control</i>	21
1.3	<i>Approach and Contributions</i>	22
2	<i>Background</i>	25
2.1	<i>Prosthesis Design</i>	25
2.2	<i>Prosthesis Walking Control</i>	31
2.3	<i>High-Level Control</i>	36
2.4	<i>Prosthesis Optimization</i>	37
3	<i>Transfemoral Prosthesis Development</i>	41
3.1	<i>Mechanical Design</i>	41
3.2	<i>Series Elastic Actuator Control</i>	47
3.3	<i>Performance Evaluation</i>	49
4	<i>Neuromuscular Model</i>	55
4.1	<i>Mechanical Model</i>	55
4.2	<i>Hill Muscle Models</i>	57
4.3	<i>Stance Reflexes</i>	59
4.4	<i>Swing Leg Control</i>	61
4.5	<i>Control for Simulation Experiments</i>	63
4.6	<i>Control for Prosthesis Experiments</i>	63

5	<i>Simulated Comparison of Neuromuscular and Impedance Controllers</i>	67
	5.1 <i>Methods</i>	67
	5.2 <i>Results</i>	69
	5.3 <i>Discussion</i>	71
6	<i>Preference Based Optimization</i>	73
	6.1 <i>Bayesian Approach Introduction</i>	73
	6.2 <i>Bayesian Approach Methods</i>	76
	6.3 <i>Bayesian Approach Results</i>	79
	6.4 <i>Bayesian Approach Discussion</i>	81
	6.5 <i>Bandit Approach Introduction</i>	82
	6.6 <i>Bandit Approach Methods</i>	83
	6.7 <i>Bandit Approach Results</i>	87
	6.8 <i>Bandit Approach Discussion</i>	90
7	<i>Experimental Comparison of Neuromuscular and Impedance Controllers</i>	95
	7.1 <i>Introduction</i>	95
	7.2 <i>Methods</i>	96
	7.3 <i>Results</i>	101
	7.4 <i>Discussion</i>	105
8	<i>Reactive Swing Control for Trip Avoidance</i>	111
	8.1 <i>Classification Approach Introduction</i>	111
	8.2 <i>Classification Approach Methods</i>	113
	8.3 <i>Classification Approach Results</i>	117
	8.4 <i>Classification Approach Discussion</i>	119
	8.5 <i>Planning Approach Introduction</i>	121
	8.6 <i>Planning Approach Methods</i>	122
	8.7 <i>Planning Approach Results</i>	131
	8.8 <i>Planning Approach Discussion</i>	133

9	<i>Robust and Adaptive Stance Control via Extended Kalman Filter-based Phase Estimation</i>	137
	9.1 <i>Introduction</i>	137
	9.2 <i>Phase Based Control Implementation</i>	138
	9.3 <i>Methods</i>	142
	9.4 <i>Results</i>	148
	9.5 <i>Discussion</i>	151
10	<i>Conclusion</i>	155
	<i>Bibliography</i>	159

List of Figures

- 1.1 Examples of microprocessor-controlled mechanically-passive knee prostheses 19
- 1.2 Vanderbilt University's Robotic Transfemoral Prostheses 20
- 1.3 BiOM Robotic Ankle Prosthesis 21

- 2.1 Vanderbilt University's Robotic Transfemoral Prostheses 26
- 2.2 Torque vs angle relationship for the ankle during level ground walking 27
- 2.3 Series elastic actuator diagram 29
- 2.4 Torque vs angle relationship for the knee during level ground walking 31
- 2.5 Example finite state machine for the impedance control 32
- 2.6 Neuromuscular model used by Eilenberg et al. [2010] to control an active ankle prosthesis. 35

- 3.1 Render of proposed powered knee and ankle prosthesis design 41
- 3.2 Knee motor torque required for running 42
- 3.3 Internal and external design of the knee joint. 43
- 3.4 Impact simulation we used to determine appropriate series spring stiffness. 43
- 3.5 Ankle torque vs angle curve during steady, level-ground walking 45
- 3.6 Ankle motor torque required to take the trip recovery action 45
- 3.7 Ankle motor torque required to reproduce a running trajectory 46
- 3.8 Internal and external design of the ankle joint. 46
- 3.9 Impact simulation we used to determine appropriate series spring stiffness. 47
- 3.10 GRF sensor readings compared to ground truth GRF data 47
- 3.11 Dynamics model used to derive sea control 48
- 3.12 Prosthesis configuration used for experiments 49
- 3.13 Fixture for testing bandwidth of actuators 50
- 3.14 Experimentally obtained bode plots of knee and ankle actuator torque 51
- 3.15 Zero torque tracking of knee and ankle joints 52
- 3.16 Knee and ankle torque tracking during a typical step 52

4.1	The skeletal model we use to simulate neuromuscular reflex control	55
4.2	Hill-type muscle tendon unit diagram	57
4.3	Force-length relationship of the CE.	57
4.4	Force-velocity relationship of the CE.	57
4.5	PE and SE force length relationship	58
4.6	Biped walking model with labeled muscles.	58
4.7	The idealized swing leg control guides the leg towards a desired landing leg angle α_{tgt} through three phases	61
4.8	Interaction between transfemoral prosthesis and neuromuscular control	64
4.9	Universal stance/swing state machine	65
5.1	Simulated control performance of prosthesis on rough terrain	70
5.2	Simulated tripping response of the amputee model with neuromuscular and impedance control	71
6.1	Learning from preferences with PES-P	75
6.2	Comparison of Preference-based Bayesian optimization methods	79
6.3	Results of offline optimization to fits neuromuscular model to intact-subject gait data at different speeds	86
6.4	Total Copeland score achieved by each parameter set across all five subjects.	87
6.5	Median angles and moments for all parameter sets for all subjects.	88
6.6	Average net ankle work for each subject at each speed	89
7.1	Example of fit to subject data achieved by neuromuscular model.	96
7.2	Finite state machine used for impedance control scheme	97
7.3	Example of fit to subject data achieved by impedance control model	98
7.4	Average user ratings	101
7.5	Total number of falls	101
7.6	Torso pitch angle variation	102
7.7	Torso roll angle variation	102
7.8	Fraction of steps for which impedance control successfully transitions through all three stance phases	103
7.9	Comparison of user scores of optimal versus suboptimal parameters sets	104
7.10	Comparison of number of falls of optimal versus suboptimal parameters sets	104
8.1	Comparison of minimum jerk and adaptive swing controls when stepping over obstacle	112
8.2	Forward-Backward Classifier Overview	114
8.3	Knee Angle Regression Feedback	115
8.4	Bang-bang obstacle avoidance and minimum jerk swing trajectories	116

8.5	Obstacle height vs backwards classifier score, knee angle training data, realized knee angles	119
8.6	Kinematic model of the user and prosthesis used for state estimation and motion planning	123
8.7	Trajectories of extended Kalman Filter (EKF) estimate of the position of the leg during swing compared to ground truth data from motion capture system	126
8.8	Example of hip angle and height trajectory predictions	127
8.9	Planning Algorithm Steps	128
8.10	Knee and ankle trajectories produced during normal walking and while eliciting trips	132
8.11	Kernel density estimate of the probability landing knee flexion angles	133
8.12	Kernel density estimate of the probability of integrated ground reaction force	134
8.13	Average toe height vs average hip height	135
9.1	Phase angle over eight seconds of walking.	140
9.2	Results from test of unified phase variable controller.	141
9.3	Examples of learned control surfaces	145
9.4	Powered prosthesis attached to amputee's personal socket	146
9.5	Ability to reproduce normal walking characteristics	148
9.6	Average kinematic and kinetic errors	149
9.7	Robustness to ground height disturbances	150
9.8	Adaptability of phase estimate	150
9.9	Example of EKF-based phase estimation versus time-based phase estimation for one subject	151
9.10	Response to sudden treadmill stops	152
9.11	GP-EKF phase control with fixed control surfaces and increased ankle impedance.	153

List of Tables

2.1	knee and ankle torque, velocity, and power for walking	25
2.2	Estimated reflected inertia of Generation 3 Vanderbilt Prosthesis	28
3.1	Designed and achieved prosthesis design specifications	42
3.2	Median root mean squared (RMS) torque tracking error during stance and swing	53
4.1	Skeletal model parameter values	55
4.2	Joint limits for the hip, knee, and ankle joints	56
4.3	Neuromuscular parameters for shared entities (left) and the hamstring muscle (right)	58
6.1	Parameters optimized to generate parameter sets for dueling bandits optimization	85
7.1	Parameters optimized for parameter set generation for experiment comparing neuromuscular and impedance control	96
7.2	Tally of observed reasons for falls	103
8.1	Obstacle avoidance classifier performance, able-bodied	117
8.2	Obstacle avoidance classifier performance, amputee	118
8.3	Obstacle avoidance success rates	118
8.4	Online and Offline Forward Classifier Performance, Amputee	118

1

Introduction

1.1 Motivation

Six hundred thousand lower-limb amputees currently live in the United States according to recent estimates [Ziegler-Graham et al., 2008]. People undergo amputations due to a variety of reasons including traumatic injuries from workplace accidents, traffic collisions, and as casualties of war. In addition, a large percentage (54%) suffer from the loss of a limb due to complications arising from dysvascular disease associated with diabetes. Consequently, largely due to the expected increase in diabetes in the coming years, Ziegler-Graham et al. [2008] estimate that by 2050 the number of amputees living in the United States will likely double.

Currently, prosthetists often prescribe transfemoral amputees (those with amputations between the hip and knee joints) an energy storage and return composite foot such as the Thrive Foot (Freedom Innovations; Irvine, CA; fig. 1.1c) along with a microprocessor-controlled, mechanically-passive knee prosthesis. These knee prostheses feature control algorithms that adjust the knee's resistance in response to kinematic and force data measured by sensors embedded in the device. Examples of microprocessor-controlled prosthetic knees include the C-Leg (Otto Bock; Duderstadt, Germany; fig. 1.1a), which has an adjustable hydraulic damping system, and the Rheo Knee (Össur; Reykjavik, Iceland; fig. 1.1b), which achieves variable damping via a magnetorheological fluid. While Johansson et al. [2005] show microprocessor-controlled knees can improve amputee gait characteristics by decreasing metabolic energy consumption, decreasing peak hip torque, and increasing gait smoothness compared a fully-passive knee prosthesis, these prostheses still cannot fully replicate healthy leg behavior as they are incapable of providing positive net power during the gait cycle and are may be limited to providing positive power only during fixed portions of the gait cycle.

Control of positive power generation is important as positive



(a) C-Leg™ Knee ©Ottobock



(b) Rheo™ Knee ©Össur



(c) Thrive™ Foot ©Freedom Innovations

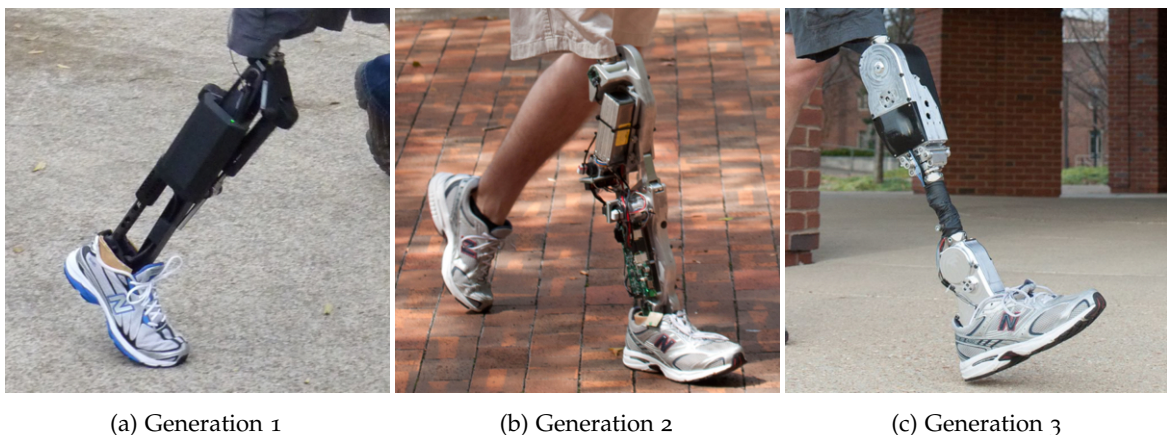
Figure 1.1: Examples of microprocessor-controlled mechanically-passive knee prostheses (a,b) and a energy storage and return ankle-foot prosthesis (c).

power is evident in a number of locomotion tasks. In the knee joint, we see positive power during level walking [Perry and Burnfield, 2010], walking up stairs [Nadeau et al., 2003], running [Buczek and Cavanagh, 1990], and jumping [Hubley and Wells, 1983]. In addition, active knee flexion and extension muscle activations have been noted during stumble recovery [Eng et al., 1994]. At the ankle joint, passive spring-like prostheses cannot replicate the positive net work seen in the ankle joint during level ground walking, which is essential for push-off and forward propulsion [Perry and Burnfield, 2010].

Consequently, lower-limb amputees and especially *transfemoral amputees*, those with above the knee amputations, equipped with mechanically-passive prostheses suffer from a number of issues including markedly increased energy consumption [Waters et al., 1976], abnormal gait kinematics [Jaegers et al., 1995], and an increased likelihood of falling [Miller et al., 2001]. Specifically, large percentages of transfemoral amputees report they are unable to complete tasks such as walking outside in inclement weather (47.4%), walking while carrying a load (42.7%), walking up or down stairs without a handrail (38.5%, 37.9%), walking outside on uneven terrain (29.5%), picking up an object from the ground (28.1%) or getting up from the floor after a fall (22.8%) [Gauthier-Gagnon et al., 1999].

To help remedy this situation, in the past decade academic research groups and companies have developed robotic powered knee and ankle prostheses for lower-limb amputees. These prostheses feature actuators at the knee and/or ankle that, if controlled correctly, could potentially restore the kinetics, kinematics, and reactions of the healthy human leg. Notable examples include three generations of transfemoral prostheses developed by Vanderbilt University (fig. 1.2) [Sup et al., 2009, Lawson et al., 2013, 2014] and the BiOM powered ankle (fig. 1.3) [Herr and Grabowski, 2011]. These powered pros-

Figure 1.2: Vanderbilt University's Robotic Transfemoral Prostheses. Images courtesy of Michael Goldfarb.



theses have helped amputees walk on level ground more naturally and efficiently, as well as walk up stairs and slopes [Sup et al., 2011, Lawson et al., 2013], run [Huff et al., 2012, Shultz et al., 2015], perform sit-to-stand [Varol et al., 2009], and dance [Rouse et al., 2015]. These results illustrate the benefits of powered prostheses as many of these tasks require positive joint power and thus would be difficult to perform with mechanically-passive prostheses.

1.2 Challenges in Transfemoral Prosthesis Control

It still remains an open research question how best to control active prostheses to achieve natural and robust gaits. Prosthesis controllers should address a number of important challenges:

Challenge 1: Control must ensure stability of prosthesis and amputee Miller et al. [2001] found that 49.2% of lower limb amputees feared falling and that of those afraid of falls 76% avoided physical activity as a result. Avoidance of physical activity is eminently concerning as it may lead to reduced strength, endurance, and balance, feeding a positive feedback loop that causes further debilitation. Therefore, to improve amputee quality of life it is imperative that powered prosthesis control strategies reduce the risk of falling.

In a traditional robotic system, this goal translates to ensuring the stability of the states of the robotic system. However, for a robotic prosthesis, the stability of the prosthesis state is insufficient to guarantee amputee stability. It is possible for all prosthesis states to be nominal while its user faces a precarious situation. Consequently, prosthesis controllers should ensure, either empirically or formally, that both the prosthesis and amputee states remain stable in the presence of myriad of disturbances. We investigate the robustness of proposed prosthesis controllers in chapters 5 and 7 to 9.

Challenge 2: Control should ideally only use information that can be garnered from sensors on the prosthesis itself Prosthesis control is complicated by sensing restrictions in a practical prosthetic device. While full instrumentation of the amputee's limbs and the prosthesis may help guarantee the stability of the overall system, in a practical prosthesis device, donning and doffing these sensors may be overly burdensome for amputees in the real world. Therefore, in this thesis, we only consider approaches that use information that could be reasonably garnered from sensors on the prosthesis and its socket.

Challenge 3: Control must adapt to suit the needs of individual users Variations in gait between amputees arise due to a number of factors



Figure 1.3: BiOM Robotic Ankle Prosthesis. Photo by Steve Jurvetson, CC BY 2.0, Link (cropped from original).

including the amputee's limb-lengths, weight, strength, endurance, reason for amputation, time since amputation, experience, and personal preferences. Consequently, prostheses and controllers should be optimized to suit individual users. In this thesis we explore methods for optimizing prosthesis parameters from user preferences (chapter 6) and in latter work propose control methods that automatically adapt to the user's gait (chapters 8 and 9).

Challenge 4: Control should allow the prosthesis to interact dynamically with the amputee and environment In human walking, during stance the leg acts in a compliant, spring-like manner [Geyer et al., 2006] and significant time is spent in statically-unstable contact on the heel or toe, suggesting the importance of mechanical stability achieved via foot placement [Perry and Burnfield, 2010]. During swing, ballistic motion explains much of the leg trajectory [Monchon and McMahon, 1980]. Indeed, much of the entire gait cycle can be explained via passive dynamics as evidenced by passive-dynamic walkers that can stably walk down slight inclines with no onboard power source [McGeer, 1990, Collins et al., 2005].

Consequently, in order to ensure that amputee gaits are natural, efficient, and robust to disturbances, it is essential that the design and control of robotic prostheses admit and leverage the inherent dynamics of walking. Therefore, in chapter 3 we detail the mechanical design and low-level control of a prosthesis that can precisely track torques. Furthermore, all controllers proposed in this thesis command desired torques to the prosthesis to allow for compliant interaction with the amputee and the environment. This is either accomplished via controllers that directly command torques as a function of sensor inputs, as in the case of neuromuscular control (chapter 4), or, when kinematic objectives are specified, accomplished via the use of feedforward torque commands and low-gain feedback, as in the case of our proposed swing (chapter 8) and phase-based stance controllers (chapter 9).

In this thesis, we primarily focus on addressing challenge 1 by evaluating the robustness of various prosthesis controllers, learning from those evaluations and proposing new methods to improve gait stability. However, in all presented work we make sure to keep challenges 2 to 4 in mind.

1.3 Approach and Contributions

We first investigate whether a novel neuromuscular transfemoral prosthesis control can improve gait robustness. This control approach seeks to mimic the underlying dynamics and control of the human

neuromuscular system. Unlike the popular finite state impedance control methods, which we review in section 2.2.2, during stance, the neuromuscular control approach provides smooth torque outputs that do not vary drastically due to discrete phase transitions. We are motivated to evaluate this control approach by simulations of biped walking models driven by neuromuscular control that demonstrate its robustness [Song et al., 2013, Song and Geyer, 2015] and potential for improvement over finite state impedance control (chapter 5 [Thatte and Geyer, 2016]) and by previous work demonstrating the adaptability of neuromuscular control on powered ankle prostheses [Eilenberg et al., 2010, Markowitz et al., 2011].

To objectively compare the proposed neuromuscular prosthesis control approach to other methods we required a transfemoral prosthesis capable of accurately reproducing desired torques. To this end, in chapter 3 we detail our first contribution: the design of a transfemoral prosthesis that uses series elastic actuators to achieve accurate torque control and is capable of large joint torques to allow for behaviors such as running and stumble recovery. We evaluate the proposed design by measuring its torque tracking bandwidth, zero torque tracking capability, and ability to track torques during normal walking.

Also needed to objectively compare control methods, is a method of finding parameters that suit individual subjects. There are two main issues that must be overcome to solve this problem. First, it is unclear which metric of gait we should be optimizing. There are a myriad of qualities necessary for a “good” gait including gait robustness, naturalness, energy efficiency, and comfort. Some of these metrics such as naturalness can be easily quantified, others, such as robustness and energy efficiency are quantifiable but only with considerable data, and others, such as comfort, are less easily quantifiable. Even if these metrics can be quantified their relative importance is unknown and may be unique to each user. The second issue is that many prosthesis control methods have a large number of parameters, which makes optimization of their parameters difficult due to the curse of dimensionality. For example, to find parameters for the neuromuscular control scheme we propose in section 4.6, we optimize at least 18 parameters.

We present two contributions in chapter 6 to tackle these issues. Both approaches utilize preference feedback between pairs of control parameters that allow the user to implicitly define the cost function via their qualitative feedback. In the first approach, we examine a Bayesian optimization scheme that chooses, at each iteration, a pair of parameter vectors to compare that is expected to maximize information gained about the location of the user’s optimum. Our

experimental results show that this approach is unable to address problems of large enough dimensionality. Therefore, in the second contribution, we propose an alternative approach that utilizes offline optimizations to generate a discrete library of control parameter sets from which the user chooses their optimum, again through pairwise preference feedback.

With the prosthesis and parameter selection method in place, in chapter 7, we present the results of an objective comparison between neuromuscular and impedance control strategies. Based on the simulations results comparing neuromuscular and impedance control presented chapter 5, we hypothesized that neuromuscular control would be less susceptible to falls than impedance control. While we could not verify this hypothesis at the $p < 0.05$ level, we were able to identify failure modes that were unique to impedance control and found that identifying trips during swing could have a major impact on gait robustness.

Based on the results of the preceding experiment we make three additional contributions. The first two, presented in chapter 8 are motivated by the observation that trips account for a significant number of falls recorded in the above experiment. Prosthesis swing controls that reduce the risk of tripping is a largely unexplored area. We explore two distinct approaches to tackle this problem. In the first, we employ online learning to train a classifier that can detect the user's obstacle avoidance intent and switch the prosthesis swing trajectory to a safer one. In the second approach, we attach a laser distance sensor to the prosthesis and develop an extended Kalman filter to estimate the user's hip height and orientation. We use this state estimate to explicitly plan swing trajectories for the knee and ankle joints that avoid premature toe and heel contact.

Finally, in the last contribution presented in chapter 9, we propose a new stance control strategy that seeks to rectify the observed issues with impedance control without the complexity of neuromuscular control. Moreover, this new proposed strategy seeks to rectify the issues we faced when implementing a previously proposed phase-based control [Quintero et al., 2016]. In the proposed control method, we obtain a continuous phase estimate using a multitude of measurements and an extended Kalman filter. We evaluate the robustness, naturalness, and adaptability of the proposed control in experiments with seven able bodied subjects and one amputee subject.

2

Background

2.1 Prosthesis Design

We can trace efforts to build an active knee-ankle prostheses to the seventies when Flowers [1974] created an active knee-ankle prosthesis to test potential control schemes. This prosthesis used a hydraulic actuator capable of producing $90 \text{ N} \cdot \text{m}$ of torque and 0.5 rev/s of no-load speed. With this device, Donath [1974] tested a controller based on EMG measurements. This line of research proved to be far ahead of its time, as most relevant research in active lower-limb prostheses design has occurred only in the last ten years. The recent interest in active knee ankle prostheses has been spurred by hardware improvements that allow designs to approach the strength, speed, and low weight of the biological leg. Enabling technologies include power-dense brushless motors, motor controllers, and lithium-ion batteries, inexpensive microcontrollers and inertial measurement units (IMUs), and strong but light composite materials such as carbon fiber. With these advancements, engineers have successfully designed prostheses to meet or exceed the requirements for walking (table 2.1).

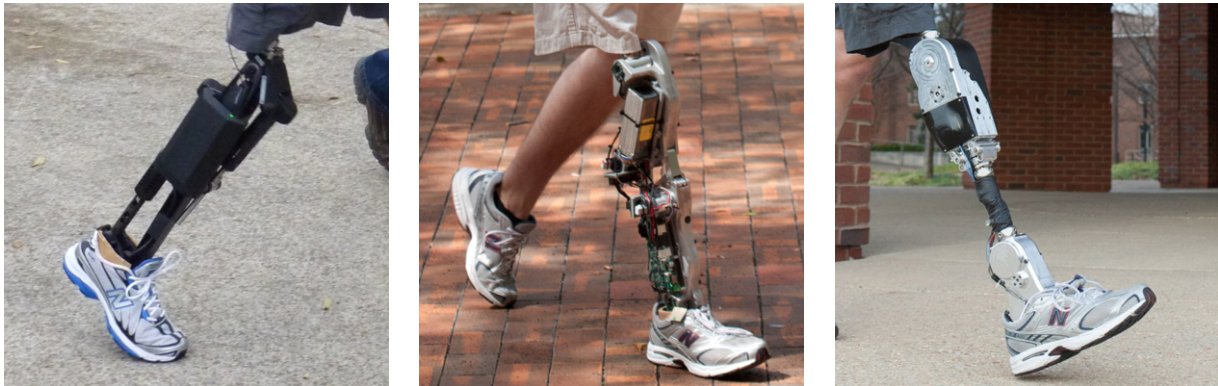
In this section, we review a number of recent prosthesis designs and analyze their ability to enable dynamic locomotion. To address this challenge, prostheses should be able to regulate their output joint torques and behave as though they have inertial properties similar to that of a normal human leg. Doing so ensures that a prosthesis can emulate the energy efficient gaits of normal walking and remain compliant to unforeseen disturbances and uneven terrain.

2.1.1 Rigid Transmission Transfemoral Prostheses

The most common approach for active transfemoral prosthesis design employs electric motors with transmissions that are rigidly coupled to the knee and ankle joints. The transmissions may utilize a combination of gears, chains, belts, ball screws, and four-bar-mechanisms

	Ankle Max	Knee Max
Velocity	0.72 rev/s	1.17 rev/s
Torque	$130 \text{ N} \cdot \text{m}$	$57 \text{ N} \cdot \text{m}$
Power	350 W	120 W

Table 2.1: Required knee and ankle torque, velocity, and power for walking (1.40 m/s average speed, scaled to 85 kg subject, data from Winter [2009])



(a) Generation 1 used ball screw transmissions, 200 W brushless motors, and a unidirectional parallel spring in the ankle that reduced motor torque requirements [Sup et al., 2009]. (b) Generation 2 replaced ball screws with custom gear-based transmission and a linear torsion spring in the ankle that is less noisy and more durable [Lawson et al., 2013]. (c) Generation 3 features a modular design with separable knee and ankle units [Lawson et al., 2014].

in order to increase the torque output of the actuator, at the expense of speed, in order to satisfy the requirements listed in table 2.1. A successful line of transfemoral prostheses following this design paradigm comes from Vanderbilt university. The first prosthesis in this line (fig. 2.1a) used a pair of ball screw transmissions and brushless motors capable of 200 W of continuous power output to drive its knee and ankle joints [Sup et al., 2009].

With these actuators, the knee motor can achieve the required peak torque and peak power intermittently (table 2.1). However, the ankle motor may be overly stressed due to the high requirements of walking. To remedy this, this prosthesis includes a unidirectional parallel spring in the ankle that reduces the required ankle motor torque. As shown in figure fig. 2.2, during level ground walking, a linear torsion spring accounts for a significant portion of the ankle's torque versus angle relationship. Therefore, incorporating a spring into the ankle offloads this portion of the torque from the motor. The ankle motor only needs to provide the difference between the desired output torque and the linear spring. As a result, the spring reduces motor energy consumption, heat generation, and transmission wear.

Further improvements resulted in two more generations of prostheses (fig. 2.1b,c) [Lawson et al., 2013, 2014]. These versions replaced ball screw transmissions with a multi-stage belt/chain which improved packaging and reduced noise and wear. With these prostheses, researchers have extensively tested a variety of control strategies including finite state impedance/quasi-stiffness control [Sup et al., 2009, 2011, Lawson et al., 2013, 2014, Lenzi et al., 2014b], EMG-based control [Ha et al., 2011, Varol et al., 2010], minimum jerk trajectory following [Lenzi et al., 2014a], and virtual constraint control [Gregg

Figure 2.1: Vanderbilt University's Robotic Transfemoral Prostheses.

et al., 2014].

Additional prostheses in the rigid transmission category include AMPRO [Zhao et al., 2016], and a commercially available active knee and ankle prostheses: the Össur Power Knee and Proprio Foot. The AMPRO prosthesis features two 374 W motors coupled to Harmonic Drive transmissions. Zhao et al. [2016], use this prosthesis to assess the merits of a virtual constraint controller. The Össur Power Knee features an electric motor that can provide torque to facilitate sit-to-stand motions, stair climbing, and active extension and flexion during walking. The Proprio Foot also features electric actuation that allows it to adapt to terrain and dorsiflex the ankle during swing to help avoid trips.

Torque Control Strategies for Rigid Transmission Prostheses

In order to achieve dynamic locomotion capabilities, it is crucial that prosthesis designs allow for closed loop control of torques. To do this, the control system must be able to accurately measure the torque at the joint output. There are two main strategies for torque measurement used by prostheses with rigid transmissions.

The first strategy is to measure the current draw of the motors windings, which is related linearly to the motor torque. One can then multiply this measurement by the gear ratio to obtain an estimate of the output joint torque. This is the method used by Generations 2 and 3 of the Vanderbilt prosthesis as well as the AMPRO prosthesis. The benefit of this method is that it utilizes existing hardware and allows one to use high frequency current control modes of motor drivers. However, a drawback of this method is that it measures the torque before the transmission. Consequently, it does not account for frictional losses, which can be difficult to model, especially for geared systems. A strategy that deals with this problem is to install load cells in series with the motor after the transmission, as was done on Generation 1 of the Vanderbilt prosthesis. With this method, the closed-loop control can compensate for frictional losses as they are included in the torque measurement.

However, this method may still not address a second problem: sluggish passive dynamics caused by reflected inertia and damping. Reflected inertia refers to the apparent magnification of motor rotor and gearing inertia on the outside of gearbox. We can derive this effect through Newton's second law for the geared motor

$$J_i \ddot{\theta}_i = \tau_i - b_i \dot{\theta}_i. \quad (2.1)$$

Here, θ and its derivatives refer to angular states of the motor, b is the damping constant, J is the inertia and τ is the motor torque.

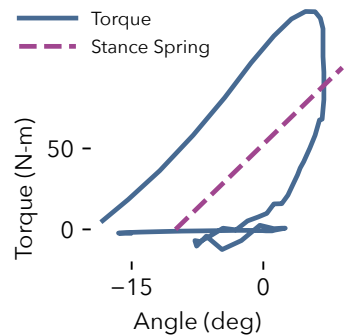


Figure 2.2: Torque vs angle relationship for the ankle during level ground walking. A linear spring relationship captures a significant portion of ankle function during stance. Data from Winter [2009] scaled to 85 kg subject.

	Knee	Ankle
rotor inertia	$0.035 \text{ kg} \cdot \text{cm}^2$	$1.210 \text{ kg} \cdot \text{cm}^2$
gear ratio	176:1	115:1
reflected inertia	$0.11 \text{ kg} \cdot \text{m}^2$	$1.6 \text{ kg} \cdot \text{m}^2$
human inertia	$0.66 \text{ kg} \cdot \text{m}^2$	$0.019 \text{ kg} \cdot \text{m}^2$
percent increase	17%	8400%

We use subscript i to refer to these quantities as seen before the gear reduction, and subscript o to refer to those quantities reflected outside of the motor. Substituting $\theta_i = n\theta_o$ and $\tau_i = \frac{1}{n}\tau_o$, where n is the gear ratio, and multiplying through by n yields

$$J_i n^2 \ddot{\theta}_o = \tau_o - b_i n^2 \dot{\theta}_o \quad (2.2)$$

$$\implies J_o \ddot{\theta}_o = \tau_o - b_o \dot{\theta}_o. \quad (2.3)$$

These equations show that the inertia and damping of the motor rotor are amplified by the square of the gear ratio. As prostheses may often use gear ratios in excess of 100:1, this effect can be substantial.

For example, table 2.2 shows the calculated reflected inertias of the Maxon Motors used in Generation 3 of the Vanderbilt prosthesis and compares the values to the estimated inertia of the shank and foot about the knee and the foot about its center of mass. We see that at the knee, the reflected inertia is roughly 17% of that of the human shank and foot. In practice, this value is likely several times higher after including the inertia of the encoder, bearings, and gearing. Consequently, we can estimate that the reflected inertia may be on the order of the leg itself. At the ankle, the reflected inertia of the rotor alone is several orders of magnitude more than that of the foot and more than twice that of the shank and foot. When we also consider reflected damping and friction, the dynamics of prosthesis system may be significantly slower than assumed.

The increase in joint impedance created by transmissions could present an issue when attempting to execute dynamic behaviors involving impact such as running or trip recovery. In an impact event, the impulse will move through the system at the speed of sound through metal, roughly 6420 m/s for aluminum [Lide, 2004]. If the prosthesis is 0.5 m long, the shock will traverse its length in 0.00008 seconds. This is about 10 times faster than the typical 1000 Hz control frequency of prosthesis control systems, rendering closed loop torque control with load cells unresponsive. The impact shock could cause damage to gearing and discomfort for the amputee.

Table 2.2: Estimated reflected inertia at knee and ankle joints of Generation 3 Vanderbilt Prosthesis [Lawson et al., 2014]. Motor data taken from Maxon Motors Catalog [Motor, 2016b,a] Knee reflected inertia compared to inertia of human shank and foot about knee. Ankle inertia compared to human foot about its center of mass. Human inertias estimated from Winter [2009] for an 85 kg, 1.7 m tall person.

2.1.2 Design of Dynamic Prostheses

In contrast to the rigid transmission actuation discussed in the previous subsection, prostheses that employ series elastic actuation may be better poised to achieve dynamic locomotion [Pratt and Williamson, 1995]. This actuation scheme (illustrated in fig. 2.3) aims to solve the torque measurement and impedance amplification caused by transmissions by placing a spring in series with the actuator. Measuring the deflection of the spring allows for accurate closed-loop control of the joint torque. Moreover, the spring low-pass filters external impulses, granting the control system more time to move the motor rotor in response to the external load. Due to these properties, designers have integrated series elastic actuators into a number of bipedal robots that seek to achieve dynamic locomotion such as M2V2 [Pratt and Krupp, 2008] and ATRIAS [Grimes, 2013].

Series elastic actuators have found use in a variety of transtibial and transfemoral prostheses. We can further split these applications into two categories, those that optimize the spring stiffness for control bandwidth subject to shock tolerance and those that optimize spring stiffness to optimize efficiency.

Springs for Bandwidth and Shock Tolerance

Adding a spring between the gear and load introduces additional dynamics between external torques and torques applied to the gearbox as external torques must physically displace the load before they generate torque on the motor. This property can improve the shock tolerance of SEA actuators over that of direct drive motors [Robinson, 2000]. However, by the same token, the SEA also introduces additional dynamics between motor torque and load torque, hence reducing force control bandwidth. Therefore, a trade-off exists between the compliance of the actuator and speed with which it can generate desired torques.

Au et al. [2007], Au and Herr [2008] design powered ankle prostheses with this trade off in mind. In these publications, the authors find that using a SEA spring soft enough to protect the ball screw transmission results in insufficient closed loop torque control bandwidth. To overcome this shortcoming, the authors incorporate a parallel spring into the ankle as was done for some of the knee and ankle prostheses discussed in section 2.1.1. Because the parallel spring offsets the motor's torque requirements, Au and Herr find that it also improves the bandwidth of the system from 4 Hz to 20 Hz, thereby exceeding the requirement for walking.

Caputo and Collins [2013] also used series elastic actuators in a robotic prosthesis testbed. This system uses a large, 1.61 kW offboard

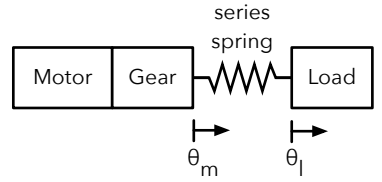


Figure 2.3: Series elastic actuation inserts a spring between the gear output and the load (here drawn as linear actuator for simplicity). Torque is measured via the spring deflection, $\tau = k(\theta_l - \theta_m - \theta_0)$ where τ is the output joint torque, k is the spring constant, and θ_l and θ_m are the load and motor positions and θ_0 is the spring's rest length.

motor connected to a light-weight prosthesis end-effector via a Bowden cable transmission. The Bowden cable applies forces to one end of a fiberglass leaf spring strain gauges measure its deflection. The author's note that the series springs isolate the prosthesis end effector from the motor's rotor inertia. With this system the authors achieve a large peak output torque ($175 \text{ N} \cdot \text{m}$) and high bandwidth (17 Hz), allowing them to rapidly test the effects of different control strategies and emulate prosthesis hardware [Caputo et al., 2015].

Springs for energy efficiency

Designers can also tune series elasticity in order to improve energy efficiency by mimicking the role of tendons in the biological human leg. In the human ankle, the Achilles tendon, which is in series with the ankle plantarflexor muscles, stores energy throughout stance and releases it just prior to toe-off, producing a surge of mechanical power. During this process, the ankle plantarflexor muscles hold the proximal end of the tendon nearly stationary via isometric contraction. This kind of length-preserving muscle contraction consumes relatively little metabolic energy compared to concentric or length-shortening contractions [Rall, 1984]. Consequently, ankle elasticity helps store and release energy, thereby improving metabolic cost of walking [Sawicki et al., 2009].

Similarly, the SPARKy prosthesis uses a *Robotic Tendon* comprised of helical springs in series with the motor to store and release energy ankle energy during stance [Hitt et al., 2007, Bellman et al., 2008, Holgate et al., 2008]. Adding a series spring changes the ankle motor movement to that required to generate desired output torque given the stiffness of the spring and trajectory of the ankle joint¹. Therefore, with a properly tuned series spring the design reduces motor movement and thus required motor power from 250 W to 77 W [Hitt et al., 2007].

Transfemoral prosthesis designs have also sought to use springs in the knee joint in order to improve energy efficiency. However, these prostheses require more sophisticated designs due to the complex behavior of the knee. Whereas a single spring relationship explains a significant portion of ankle joint behavior (fig. 2.2), as shown in fig. 2.4, the knee joint requires two springs: one for early stance and one for pre-swing and swing. Two prostheses that tackle this design problem are AAAKP (agonist-antagonist active knee prosthesis) [Martinez-Villalpando et al., 2008, 2011] and the CSEA (clutchable series elastic actuator) knee [Rouse et al., 2014, 2015].

The AAAKP prosthesis uses two unidirectional springs, one for extension and one for flexion, each in series with its own actuator.

¹ $\theta_m = \theta_l - \tau/k - \theta_0$, where τ is the desired ankle torque, θ_l is the ankle trajectory, and k and θ_0 are the spring stiffness and offset

With this setup, AAAKP is able to store energy during the knee flexion phase just after heel strike, and transfer it to a flexion spring for use during pre-swing and swing. The prosthesis consumes just 5.6J/stride. However, the downside of this design is inefficient use of actuator mass, as two electric motors are required, one for extension and one for flexion.

A second concept is to use a series elastic actuator with a clutch on the motor [Rouse et al., 2014, 2015] The clutch saves energy by holding the motor side of the series spring stationary while the spring is loaded in early stance; no electrical energy is consumed holding the rotor in place. In this design the spring-like behavior of the knee during swing is reproduced by the electric motor alone unlike in the AAAKP prosthesis. Despite this, the CSEA knee consumes less energy than the AAAKP, just 3.6J/stride. Moreover, the simplified design of the CSEA has a mass of 2.7 kg vs 3.6 kg for the AAAKP.

A potential drawback of SEA designs that are tuned for energy efficiency is that they typically tune the spring stiffness to match observed quasi-stiffness of the biological joint during a certain phase of the gait. However, this stiffness value is not necessarily that which maximizes torque control bandwidth. Therefore, while prostheses tuned for efficiency can consume less energy, which is desirable for a product needing long battery life, they may not represent the most versatile design for evaluating new control ideas or different gait modes.

2.2 Prosthetic Walking Control

2.2.1 Time Based Control

The earliest proposed robotic prosthesis control strategy, termed *echo control*, records the kinematics of the sound-side as a function of time leg on each step and then executes an identical trajectory on the prosthesis side on the following step [Grimes et al., 1977, Grimes, 1979]. Such a control strategy has a number of drawbacks. First, the control strategy requires measurement of the sound-side leg, thus burdening the amputee with additional sensors that need to be donned and doffed daily. Second, the control is unable to take an odd number of steps, and all steps must be initiated with the sound leg. Third, the control is primarily kinematic as measuring torques of the sound side leg to use as a feedforward control on the prosthesis is infeasible. Consequently, it may require high-gain feedback, which may cause discomfort and gait instability due to a lack of compliance to the environment.

Another form of time-based control, which we will use later in

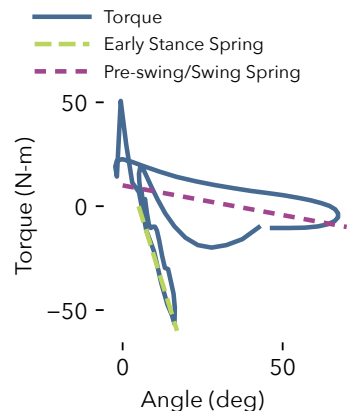


Figure 2.4: Torque vs angle relationship for the knee during level ground walking. Knee displays more complicated functionality than the ankle (see fig. 2.2), with two distinct springs need to explain early stance and pre-swing/swing behavior. Data from Winter [2009] scaled to 85 kg subject.

this thesis, is the minimum jerk trajectory swing control presented in Lenzi et al. [2014b]. This swing control strategy calculates at toeoff three minimum jerk trajectories, parameterized by 5th order polynomials, which dictate the movement of the knee and ankle joints. For the knee joint, two trajectories are computed, one that starts at the position, velocity, and acceleration of the knee at toeoff and goes to a peak flexion angle with zero velocity, and one that starts at the peak flexion state and goes to a final state of zero angle, velocity and acceleration. The peak knee angle is tuned to ensure adequate foot clearance while the acceleration at the peak angle is based on able-bodied data. For the ankle, one minimum jerk trajectory is used that starts at the position and velocity at toeoff and proceeds to a final position, velocity, and acceleration of zero. The durations of the trajectories are based on fixed percentages of the stance duration thereby automatically adapting swing phase to different gait speeds. Unlike the previously described echo control, this control strategy takes advantage of the simple double-pendulum dynamics during swing to derive a strong feedforward term that allows the use of small, compliant feedback gains.

2.2.2 Finite State Impedance Control

To alleviate issues with the time-based echo control, researchers later proposed *finite state impedance control*, which has become the most widely used control for robotic legged prostheses. In this strategy, the gait cycle is split into a sequence of discrete states or phases. During walking, a state machine switches between the phases based on sensor data meeting certain conditions, usually in the form of thresholds on joint angles, joint velocities, or ground reaction forces. Within each phase, the controller specifies an impedance relationship between the output torque at each joint and the angle and angular velocity of that joint.

For example, Sup et al. [2009], proposes a specific instantiation of this control paradigm in which the gait cycle is segmented into three stance states and two swing states as shown in fig. 2.5. In each state, the impedance of a joint is governed by

$$\tau = -k(\theta - \theta_0) - b\dot{\theta}, \quad (2.4)$$

where τ is the desired torque of a joint, k is a stiffness parameter θ_0 is the joint angle offset, b is a damping parameter and $\dot{\theta}$ is the joint velocity. If the stiffness, damping, and angle offset for each joint and the transition rules are tuned appropriately, this control scheme can be made to suit sloped walking [Sup et al., 2011] and speed variations [Shultz et al., 2016] including running [Shultz et al., 2015].

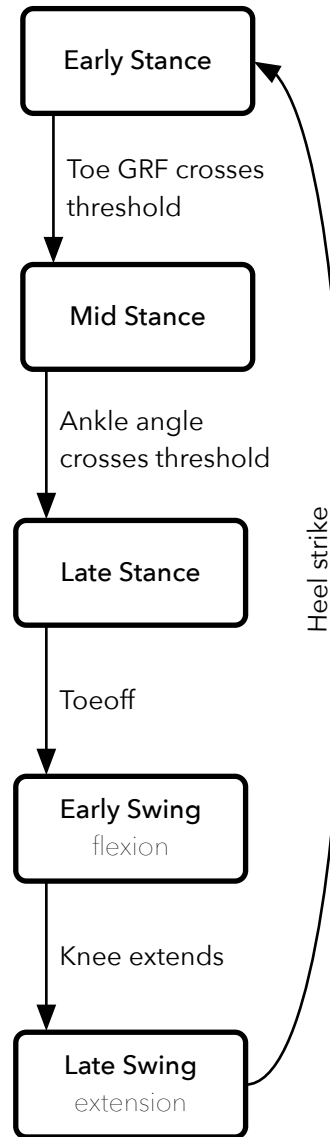


Figure 2.5: Finite state machine used for the impedance control scheme proposed in Sup et al. [2009]. In each state the control employs linear impedance functions that determine the behavior of the ankle and knee joints of an active transfemoral prosthesis.

There have also been a number of variations on this general control scheme including those with nonlinear impedance functions at the ankle [Sup et al., 2007, Shultz et al., 2014] and some using high-gain position control for the late stance push off phase of gait [Lawson et al., 2014]. Lenzi et al. [2014b] presents a similar strategy named *quasi-stiffness control* that substitutes the parameterized impedance functions given by eq. (2.4) with lookup tables that provide the torque vs angle relationship at different gait speeds.

A potential drawback of the impedance control paradigm may be its sensitivity to the rules that govern transitions between phases. A premature transition or delayed transition may cause inappropriate joint torques leading to gait instabilities and falls. For this reason, prior works have experimented with a wide variety of transition rules based on joint angles, velocities, and ground reaction forces measured by the prosthesis. Alternatively, If one is willing to instrument the sound-side leg, then Liu et al. [2014] provides a method to improve transition rules by using online learning and gait events of the sound-side leg. In this thesis, however, we focus on control strategies that do not require extra instrumentation of the body. Therefore, in later chapters we will explore, through simulations (chapter 5) and experiments with our robotic prosthesis (chapters 7 and 9), the consequences of mistimed phase transitions in a finite state impedance control scheme that does not use external sensing.

2.2.3 Continuous Phase Control

Another approach to walking control in active prostheses is to estimate or measure a continuous phase variable. This may avoid the gait instabilities that can be caused by joint torques that change discontinuously in finite state impedance control. Previous work in this area has focused on deriving phase variables from single information sources. For example, Gregg et al. [2014] enforce virtual constraints on the effective rollover shapes during walking. The rollover shapes are the locations of the center of pressure (COP) in frames attached to the shin and thigh. Proportional derivative control or feedback linearization can be used to drive the error between the measured rollover shape and desired rollover shape to zero. Typically, during walking the COP progresses monotonically from heel to toe, making it an effective phase variable. However, when walking on uneven terrain this assumption could be violated. Additionally, this definition of phase is only applicable during stance.

To obtain a phase variable that is applicable in a wider variety of situations, Quintero et al. [2016] propose using the thigh angle and its integral to derive a continuous phase variable. In this approach,

one starts by plotting in a chart the thigh angle on the x -axis and its (normalized) integral on the y -axis. Assuming the thigh angle approximately follows a cosine trajectory during gait, and with the right normalization and shift parameters, the thigh angle/thigh angle integral form a circle over one gait cycle. Therefore, one can use the polar angle of the thigh angle integral vs thigh angle as a phase variable. However, in order for the method to calculate a phase angle that increases at a predictable constant rate, the thigh angle/integral plot should be centered about the origin and the correct normalization needs to be applied to the thigh integral. Furthermore, in order for the thigh integral to reach zero again at the end of a gait cycle, the average thigh angle must be subtracted from the thigh angle before integration. The thigh angle shift, integral shift, integral normalization, and angle average must be estimated online in order to use this method. Incorrect estimation of these parameters can cause the phase estimate to diverge. Consequently, using this method for non-periodic motions is difficult. In section 2.2.3 we present our attempt to implement this style of control on our robotic prosthesis. We found that the variability from step to step alone was enough to cause significant drift in the thigh angle integral. Thus we were not able to achieve a consistent gait with this control scheme.

As a possible solution, Rezazadeh et al. [2018] recently proposed a method that eliminates the thigh angle integral and instead uses the thigh angle only. This method relies on the insight that, for the most part, during gait the thigh angle decreases monotonically from heel strike to shortly before toeoff, and then increases from that point until the next heel strike. Therefore, one can define two different relationships between the hip angle and phase for these two portions of gait and use a finite state machine to transition between them. However, reintroducing a finite state machine into the controller necessitates tuning of transitions rules between phases and may cause similar issues as in finite state impedance control.

Finally, Azimi et al. [2019] propose another approach to continuous phase-based control of prostheses uses the forward translational hip position to parameterize the desired gait trajectory. The trajectory is designed in simulation subject to a partial hybrid zero dynamics constraint that allows one to use adaptive, control Lyapunov function-based, controllers with convergence guarantees. However, to date, this control has only been used to actuate the knee of a powered prosthesis while the ankle remained passive, perhaps due to the additional complexity of dealing with multiple hybrid dynamics transitions between swing, heel contact only, heel and toe contact, and toe contact only.

In chapter 9, we propose an alternative approach to continuous

gait phase estimation that uses an extended Kalman filter to derive the phase estimate. Unlike these reviewed approaches, the proposed approach can fuse information from any combination of sensors that produce continuous output and does not need a finite state machine. Moreover, we show the resulting control can use the phase estimate to adapt to different gait speeds and enable automatic transitions to standing mode.

2.2.4 Non Phase-Based Control

So far, all walking controllers we reviewed keep track of either a discrete or continuous estimate of phase during gait. However, researchers have also proposed prosthesis controllers that do not take this approach. For example the complementary limb motion estimation (CLME) approach proposed by Vallery et al. [2011] uses linear regression to learn a direct mappings between the angles and velocities of the user's limbs to the prosthesis' joint angles and velocities. However, this approach used many IMUs mounted to the torso and sound side leg to measure the user's kinematics, and thus may be impractical for everyday use by an amputee.

Another class of non-phase based control uses neuromuscular models that simulate the dynamics of the muscle tendon units in the leg and hypothesized reflex pathways to generate the desired torques for walking. Prior work in simulation of biped walking controlled by neuromuscular models has demonstrated that this control approach can produce very natural and robust gait patterns [Geyer and Herr, 2010, Song et al., 2013, Song and Geyer, 2015].

Motivated by the robustness and natural gait achievable by neuromuscular reflex control, past research has applied this model to active ankle prostheses. Eilenberg et al. [2010] applied a simplified version of the control to a powered ankle prosthesis (fig. 2.6). In this work, the neuromuscular model was reduced to a single ankle plantarflexor muscle driven by a positive force feedback reflex during stance. During swing, the control applies torque to dorsiflex the ankle according to a virtual spring-damper model. In amputee testing of a prosthesis controlled by the neuromuscular model the control produced ankle kinematics and kinetics similar to those observed in healthy human walking. Significantly, Eilenberg et al. found evidence that the robustness properties observed in neuromuscular model simulations may carry over to amputee gait as well. The author's note that the prosthesis automatically adapts torque output when walking on slopes, producing more plantarflexion torque when walking up slopes and less when walking down slopes. Additionally, Markowitz et al. [2011] found that a similar neuromuscular reflex model automatically pro-

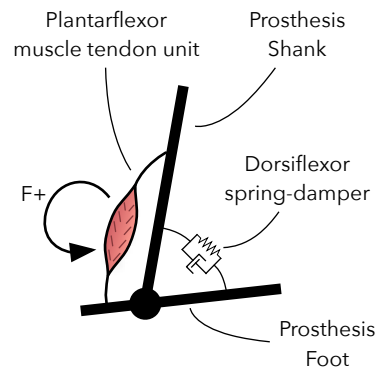


Figure 2.6: Neuromuscular model used by Eilenberg et al. [2010] to control an active ankle prosthesis. During stance, a virtual muscle driven by positive force feedback, generates plantarflexion torque. During swing, a virtual spring and damper provides dorsiflexion torque to prevent toe scuffing.

duced more ankle plantarflexion work as the amputee increased his gait speed.

The inclusion of user intent recognition via surface electromyography (EMG) signals represents an interesting extension of neuromuscular reflex prosthesis control. In these approaches, muscle activity in the residual limb is directly measured via EMG sensors embedded in the amputee's prosthesis socket. These EMG sensors are then used to control the torque generation of the amputee's leg prosthesis. Because neuromuscular models describe how joint torque is generated in response to muscle activations, a natural approach is to use the EMG signal in reflex pathways in order to activate virtual muscles. This is the approach proposed by Wu et al. [2011]. In this work, Wu et al. control an active transfemoral prosthesis using EMG sensor readings from the residual thigh to activate virtual knee flexor and extensor muscles according to a linearised Hill muscle model. The resulting prosthesis control allowed an intact subject wearing the prosthesis via an able-bodied emulator to achieve nearly normal gait. In a similar approach, Wang et al. [2013] use EMG signals to modify the gain on a positive torque feedback loop in order to control ankle plantarflexion torque. As seen in healthy human walking, toe off angle and ankle net work increased with increasing walking speed.

2.3 *High-Level Control*

In the previous section we reviewed mid-level controllers that produce desired torques given a specific mode of walking. Here, we describe high-level controllers that classify the current walking mode, such as standing, level ground walking and stair and ramp ascent/descent, so that the appropriate control parameters or type of mid-level control can be selected.

A variety of classifiers have been used to detect gait modes including artificial neural networks [Huang et al., 2009], linear discriminant analysis [Huang et al., 2009, 2011, Hargrove et al., 2015, Young et al., 2014a], Gaussian mixture models [Varol et al., 2010], support vector machines [Huang et al., 2011, Massalin et al., 2017, Yan et al., 2018], dynamic Bayesian networks [Young et al., 2014a, Hargrove et al., 2015, Spanias et al., 2018]. Additionally, papers have suggested using different sensors including electromyography (EMG) [Huang et al., 2009], prosthesis mechanical sensors [Varol et al., 2010, Young et al., 2014a,b], a combination of EMG and mechanical sensors [Huang et al., 2011, Spanias et al., 2018, Hargrove et al., 2015], and laser range finders/depth sensors [Zhang et al., 2011b, Liu et al., 2016, Massalin et al., 2017, Yan et al., 2018].

In some of the early works on gait mode recognition, a single set

of training data was collected in which modes were switched either manually or using hand-tuned rules. Using this dataset, the mode recognition classifier was trained a single time, and offline classification accuracy was reported [Huang et al., 2009, 2011, Young et al., 2014a]. However, Hargrove et al. [2015] show that when classifiers trained in this fashion are deployed on the real prosthesis, classification errors are worse in the online setting than in the offline setting. This is because the high level-controller governed by the classifier, effects the behavior of the system, and changes the distribution of data from that on which the classifier is trained. To overcome this issue, Spanias et al. [2018] provide a method for updating the classifier online so that the training and testing data distributions converge. In this method a forwards classifier, provides labels for gait modes for use in real time and a backwards classifier labels gait modes in hindsight with more data. The labels from the backwards classifier are then used to update the forward classifier.

2.4 Prostheses Optimization

Optimizing control policies for prostheses presents a challenging task due to four key issues. First, there is significant variability gait characteristics that precludes using the same parameters for all users. Recently, Zhang et al. [2017] demonstrated the effect of gait variability on lower limb assistive device optimizatoin. In this work the researchers optimized an ankle exoskeleton's torque trajectory for specific users. The authors found that optimized torque trajectories could reduce metabolic energy consumption beyond that provided by a generic assistance strategy.

Second, to optimize prostheses and exoskeletons, it is necessary to define an objective function that includes and correctly assigns importance to all characteristics that determine system performance. Most prior work in this area assumes a certain form for the objective function. For example, in the work described above, the author's assume that the metabolic energy consumption of the user is the only important factor. The authors then use the Covariance Matrix Evolution Strategy [Hansen, 2006] to optimize the parameters of the exoskeleton. In other work, Huang et al. [2016] optimize a transfemoral leg prosthesis assuming the objective is to improve the ability of the knee to track an able-bodied trajectory. In this work, the authors use a *cyber-expert system* (CES) that encodes how a human expert's tuning of impedance parameters effects the trajectory error. With this strategy, the author's improved trajectory tracking of a knee prosthesis, but also note that other metrics might be important such as metabolic energy, symmetry, and disturbance rejection. This approach was later

improved by using adaptive reinforcement learning to circumvent predefining the tuning rules [Wen et al., 2016, 2019].

If we choose to optimize more than one outcome simultaneously, we need to assign weights to each feature to each feature that reflect the users individual needs. Moreover, other aspects of gait may also be important but difficult to quantify, such as the amputee's comfort and sense of stability. In any case, measuring gait features require a high level of technical expertise and equipment to measure, and therefore preclude an amputee tuning his or her own prosthesis.

To solve the problem of defining and measuring objective functions for robotic systems that human operators can directly control, researchers have proposed *learning from demonstration* (LfD) [Argall et al., 2009]. In this paradigm, one can either circumvent learning the objective function by directly learning a policy that matches the distribution of state-action pairs recorded during human demonstrations of the desired behavior [Pomerleau, 1991, Schaal, 1999], or one can learn a reward function consistent with the demonstrator's actions and visited states and use it to derive an optimal control [Ng et al., 2000, Ratliff et al., 2006, Ziebart et al., 2009]. LfD methods are attractive because they allow non-experts to specify both the quantifiable and qualitative aspects of the desired robot behavior via the non-technical language of demonstration.

For robot behavior that people cannot demonstrate, such as the optimal behavior of an amputee's prosthesis, or the desired behavior of complex, dynamic robots, we can alternatively query human users for qualitative feedback in order to shape the robot policy. For example, the TAMER framework [Knox and Stone, 2009, Knox et al., 2013] utilizes good/bad assessments of a robot's recent actions to optimize its policy. Pilarski et al. use this method to allow subjects to optimize the policy of an EMG-controlled prosthesis arm via their positive and negative feedback signals [Pilarski et al., 2011]. Another paradigm in qualitative feedback is to obtain *preference feedback* between two or more policies or sequences of actions, which may provide more nuanced feedback than absolute ratings. For example, Jain et al. and Akroud et al. propose methods that learn a user's trajectory scoring function based on his rankings of possible policies [Jain et al., 2013, Akroud et al., 2014]. Similarly, Wilson et al. provide a method to directly identify a user's preferred policy based on her preferences between pairs of demonstrated trajectories [Wilson et al., 2012]. These prior works demonstrate that we may be able to use qualitative feedback, such as preferences, from non-expert users to program robot behavior, without prescribing an objective function. However, a drawback of the aforementioned methods that learn from preference feedback is their reliance on simulators to predict system

behavior. Human-in-the-loop systems, such as lower-limb prostheses and exoskeletons, are challenging to simulate accurately, making these methods difficult to apply.

The third issue an operator tasked with optimizing control policies for human-in-the-loop systems faces is the expense, in terms of time and effort, of repeatedly executing policies. Consequently, stochastic sampling approaches may be less applicable in this domain. To minimize the number of trials needed, researchers have proposed black-box *Bayesian Optimization* (BO) methods that model both the objective function and its uncertainty. In these methods, the uncertainty informs an acquisition function that speeds up the optimization by exploiting regions of the parameter space with believed high objective value while still exploring regions where the objective function is uncertain. For example, researchers have successfully employed BO methods to efficiently optimize the gait parameters of a robotic snake [Tesch et al., 2011] and a dynamic bipedal robot [Calandra et al., 2014]. In chapter 6 we present a new Bayesian optimization method that uses learning from preferences between pairs of control parameters to avoid priori definition of features and to consider unquantifiable qualities of the desired behavior. We apply this method to optimize several simulated tasks.

However, we also find through these experiments that the proposed Bayesian optimization approach, cannot scale to the dimensionality required for prosthesis optimization. This highlights the fourth challenge of prosthesis optimization, which is that prosthesis controllers typically have dozens of parameters, causing optimization routines to suffer from the curse of dimensionality. Therefore, in chapter 6 we also explore using a dueling bandits [Yue et al., 2012] approach to optimizing the prosthesis parameters. This approach uses significant offline computation to generate a discrete library of viable parameter sets from which the user can choose.

3

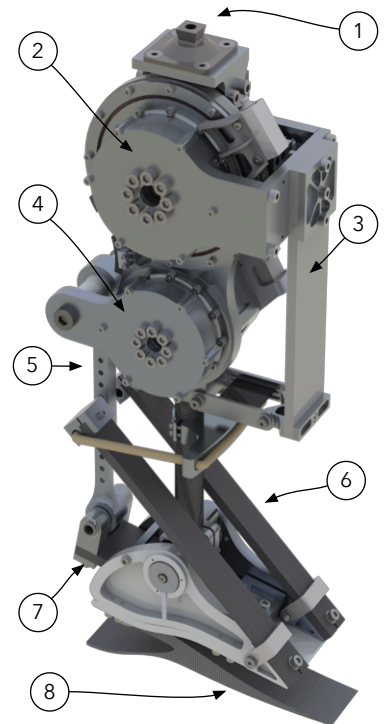
Transfemoral Prosthesis Development

3.1 Mechanical Design

To test our proposed control approaches and compare to the state of the art, we have built a custom transfemoral prosthesis capable of reproducing dynamic locomotion tasks. The prosthesis design, shown in fig. 3.1, uses brushless electric motors coupled to harmonic drive gear sets to drive both the knee and ankle joints. Additionally, the joints employ series elastic actuation to enable accurate torque control and to protect the prosthesis' gear sets from sudden impacts. The design also features optional unidirectional parallel springs in the ankle that can partly offset the torque demands on the ankle motor. We design both joints to meet the demands of dynamic locomotion tasks such as running and trip recovery.

The overall design concept sits in a niche between low powered prostheses designed with commercial applicability in mind [Sup et al., 2007, 2009, Lawson et al., 2014, Rouse et al., 2015, Martinez-Villalpando et al., 2011] which feature onboard actuation and power sources, and high-powered tethered systems [Caputo and Collins, 2013, Caputo et al., 2015] with off-board actuation designed exclusively for use in lab environment. Our design features onboard actuators that are more powerful than those used in standalone devices, but less capable than those employed in tethered devices. To ensure a reasonable overall weight the device's batteries, motor drivers, and computers are off-board. With this design, we expect to be able to test control ideas without encountering hardware performance limitations as with a tethered device. At the same time the device is capable of functioning outside of the lab environment like a standalone prosthesis.

Table 3.1 shows the desired design specifications for the transfemoral prosthesis, the design's theoretical specifications, and the experimentally confirmed values of the manufactured device. Section 3.3 provides details on the experimental evaluation of the pros-



- 1) Pyramid Adaptor
- 2) Knee Motor
- 3) Knee Series Spring
- 4) Ankle Motor
- 5) Adjustable Height
- 6) Unidirectional Parallel Spring
- 7) Ankle Series Spring
- 8) Composite Foot

Figure 3.1: Render of proposed powered knee and ankle prosthesis design. The prosthesis includes series elastic actuators to enable accurate torque control and an optional unidirectional parallel ankle spring to offset the required angle torque.

Specification	Desired Value	Theoretical Value	Achieved Value
Maximum Knee Torque	160 N · m	170 N · m	
Maximum Knee Speed	1.80 rev/s	1.93 rev/sec	
Knee Torque Bandwidth	4 Hz	11.7 Hz	24 Hz
Maximum Ankle Torque	200 N · m	170 (+120*) N · m	
Maximum Ankle Speed	1.14 rev/s	1.22 rev/s	
Ankle Torque Bandwidth	3.5 Hz	5.9 Hz	7 Hz
Mass	6.8 kg	5.9 kg	
Minimum Height	42.5 cm	42 cm	42 cm

thesis' torque bandwidth.

We specify desired joint torque and speed values to meet the requirements of demanding tasks such as trip recovery and running. The maximum knee torque specification comes from the findings of Whitley [2008], who tested the joint torques used during recovery from a simulated fall. The maximum knee speed requirement comes from Grabiner et al. [1993], who tested subjects' responses to simulated trips induced by unseen obstacles on a walkway. We obtain the maximum ankle torque requirement from Pijnappels et al. [2005], who tripped subjects using obstacles that could suddenly emerge through the floor. The maximum ankle speed requirement comes from the running data of Novacheck [1998]. We set the minimum height specification, measured between the center of the knee and bottom of the foot, to accommodate the 10th percentile female [Gordon et al., 1989]. Finally, the required mass corresponds to the mean leg mass of a 50th percentile male [Winter, 2009].

3.1.1 Knee Joint

In addition to achieving the maximum speeds and torques found in table 3.1, we design the knee joint so that it can reproduce the torque and speed required for a 80 kg person to run at 3.2 m/s as measured by Novacheck [1998]. To reproduce this trajectory in the knee joint, we utilize a RoboDrive ILM 85 × 13 HS-SP motor coupled to a Harmonic Drive Gear set with a 50:1 reduction (CSG-25-50). Figure 3.2 shows the motor torque and speed required to reproduce a running trajectory assuming a gear efficiency of 75%. In this plot, we see that the running trajectory lies within the speed-dependent torque limit of the motor. Moreover, the root mean squared torque of this trajectory (1.46 N · m) exceeds the torque rating of the motor (1.43 N · m) by just 2%. Therefore, the knee joint should be able to provide the necessary torque to enable running for a short amount

Table 3.1: Designed and achieved design specifications.

*Maximum total ankle torque is 290 N · m if the optional unidirectional springs are used. This torque is achieved at 10° of dorsiflexion.

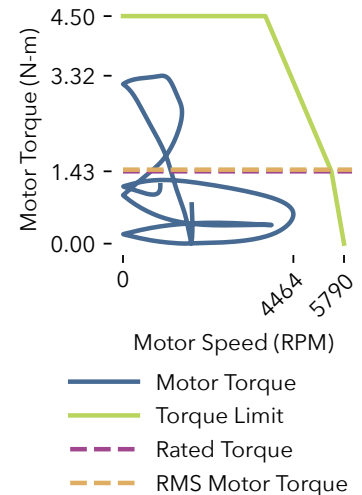
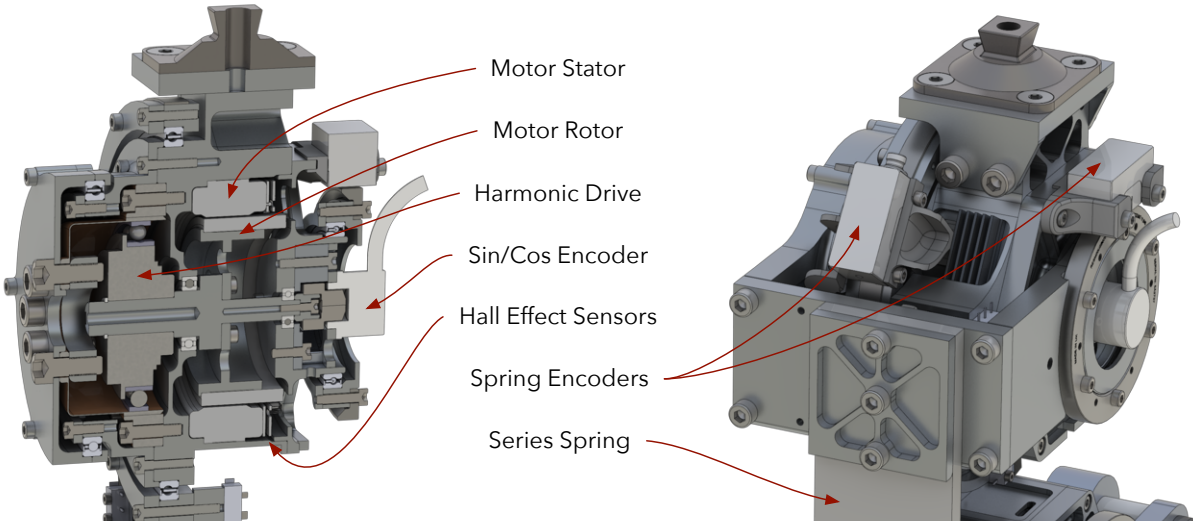


Figure 3.2: Knee motor torque required for running



of time, or continuously for lighter subjects or at a slightly reduced speed.

Figure 3.3 shows the internal and external design of the knee joint. The primary component in the knee joint is the stator housing. On top of the housing is a standard pyramid adaptor that allows the prosthesis to connect to amputee's sockets. Within the stator housing, lies the brushless motor stator, rotor, and harmonic drive gear set. We sense absolute rotor angle for commutation of the brushless motor via hall effect sensors and a magnetic complementary sin/cos encoder. To incorporate series elasticity, we take inspiration from the design of the bipedal robot Atrias [Grimes, 2013], which uses fiberglass series leaf springs. In our design, the output of the gear set drives the proximal end of a fiberglass leaf spring in series with the shank. Two Renishaw Resolute absolute encoders measure the deflection of this spring.

In addition to allowing for accurate torque control, as shown by Au et al. [2007], Au and Herr [2008], the series elasticity also plays a crucial role in protecting fragile gear components from impact loads. To choose the spring stiffness for the knee joint, we simulate the prosthesis impacting a rigid wall with the foot during swing. To do this, we construct a model of the prosthesis in Matlab Simulink Simscape Multibody that includes the series elasticity, gear dynamics, and motor electrical dynamics. Figure 3.4 shows the simulation environment. The prosthesis is attached to the distal end of a thigh segment with a fixed hip position. We control the hip via the swing leg control outlined in section 4.4 (eq. (4.30)) and consider the case where the external voltage applied to the motor is zero. This simu-

Figure 3.3: Internal and external design of the knee joint.

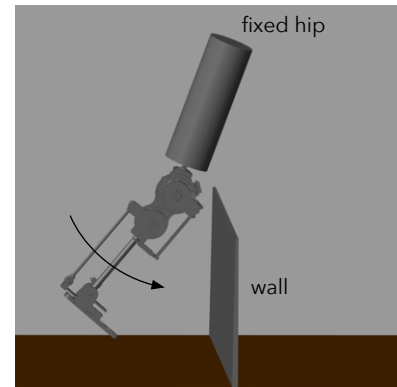


Figure 3.4: Impact simulation we used to determine appropriate series spring stiffness.

lation suggests that a spring stiffness under $2300 \text{ N}\cdot\text{m}/\text{rad}$ will ensure that the peak impact torque remains lower than the peak allowable impact torque of the Harmonic Drive of $242 \text{ N}\cdot\text{m}$.

We can also estimate the torque bandwidth of the actuator by analyzing the SEA dynamics for the system depicted in fig. 2.3. Assuming the load is fixed, the transfer function between the motor and load torques is given by

$$\frac{\tau_l}{\tau_m} = \frac{k/J_m}{s^2 + k/J_m} \quad (3.1)$$

where τ_l and τ_m are the load torque and post-gearbox motor torque respectively. J_m is the sum of the reflected motor rotor inertia and inertia of components that form the motor-side attachment of the spring, which has stiffness k . From this equation we calculate the bandwidth of the system to be

$$f_{3dB} = \frac{\sqrt{k/J_m}}{2\pi}. \quad (3.2)$$

For a spring stiffness of $2300 \text{ N}\cdot\text{m}/\text{rad}$ we estimate the torque bandwidth is 11.7 Hz . This value exceeds the required torque bandwidth of 4 Hz given by Sergi et al. [2012]¹. However, it should be noted that this is a very crude estimate of bandwidth. On the one hand, it may underestimate the true value, as it assumes that to achieve a desired output torque, the motor control applies the same torque to the motor side of the spring. In practice, a closed-loop torque control can transiently apply much larger torques to the motor side in order to achieve faster convergence to a desired steady-state output torque. On the other hand, this value may also underestimate the true bandwidth, as it does not consider the motor's voltage-current dynamics or gear friction.

¹ obtained by analyzing the torque data for walking reported by Winter [2009]

3.1.2 Ankle Joint

In the ankle joint we utilize a RoboDrive ILM 70×10 HS-SP motor coupled to a Harmonic Drive Gear set with a $100:1$ reduction (CSG-20-100). As with the knee joint, we designed the ankle joint to satisfy the requirements listed in table 3.1. Specifically, for the ankle joint we pay considerable attention to the tripping condition described by Pijnappels et al. [2005], in which the ankle generates a peak torque of $202 \text{ N}\cdot\text{m}$.

To avoid using a large and heavy motor to achieve this peak torque, we take inspiration from previous prosthetic ankle designs that employ a unidirectional parallel spring in the ankle joint that performs the conservative portion of the ankle's torque versus angle trajectory during normal walking [Au et al., 2007, Au and Herr, 2008,

Sup et al., 2009, Lawson et al., 2014]. The parallel spring offsets the required motor torque, as the actuator only needs to provide the difference between the desired torque and the torque provided by the parallel spring. Figure 3.5 shows the torque versus angle curve during level ground walking (Winter [2009], scaled to 80 kg person). In green we show the torque generated by a $700 \text{ N}\cdot\text{m}/\text{rad}$ parallel spring optimized to minimize the root-mean-squared motor torque for this trajectory. From this plot, we see that with the parallel spring, the peak torque is lower than the repeated peak torque limit of the Harmonic Drive Gear set.

The tripping data obtained by Pijnappels et al. [2005] shows that the ankle kinematics during trip recovery are similar to those seen during normal walking. Therefore, the parallel spring, should be able to contribute torque during the tripping case as well. To confirm this, fig. 3.6 shows the motor torque required for trip recovery (obtained by scaling walking torque data from Winter [2009] to have a peak torque of $202 \text{ N}\cdot\text{m}$) We see that the inclusion of the parallel spring allows the prosthesis to produce enough net torque to reproduce the trip recovery trajectory without exceeding the torque limit of the motor.

Finally, fig. 3.7 shows the torque and speed required of the motor for running [Novacheck, 1998]. In this case, we use an ankle parallel stiffness of $267 \text{ N}\cdot\text{m}/\text{rad}$. From this plot, we see that this combination of ankle motor and spring is nearly sufficient for running. Increasing the voltage of the prosthesis from 48 V to 60 V or decreasing the gear ratio from $100:1$ to $80:1$ will allow the torque trajectory to fit completely within the motor limits.

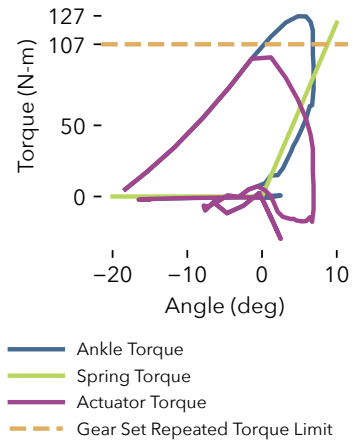


Figure 3.5: Ankle torque vs angle curve during steady, level-ground walking (blue) (Winter [2009] scaled to 80 kg person). A unidirectional parallel spring can provide a portion of this torque (green) and reduces the required actuator torque (purple) to lie under repeated torque limit of the Harmonic Drive Gear set (orange).

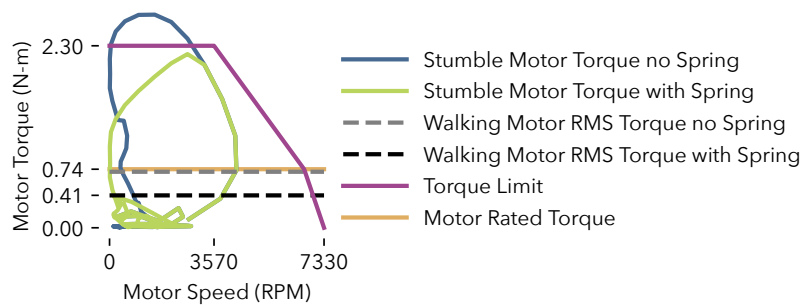


Figure 3.6: Ankle motor torque required to take the trip recovery action observed by Pijnappels et al. [2005] (blue, trajectory obtained by scaling walking data from Winter [2009] to a peak torque of $202 \text{ N}\cdot\text{m}$, 75% gear efficiency assumed). Using a parallel spring allows the motor to produce the required torque (green) while remaining within its torque limit (purple).

Figure 3.8 shows an internal view of the ankle actuator and external views of the actuator and foot mechanism. In the ankle design, the output of the actuator actuates the foot through a four-bar mechanism. The actuator pulls or pushes on the proximal end of a length-adjustable tendon. The distal end of the tendon attaches to one end of a fiberglass series elastic leaf spring that is also connected to the foot. To measure torque in the ankle joint, we measure the deviation from the nominal relationship between the ankle motor encoder and ankle encoder under the zero torque condition.

We perform a calibration routine with the prosthesis mounted sideways

The design of the ankle actuator represents a second iteration of the knee actuator design and features two main improvements. First, it has increased space on the side of the motor for cable routing. Second, the ankle actuator has a solid rotor shaft. In contrast, the knee actuator's shaft is comprised of two parts: one that held the motor rotor and transferred power through the gear set, and another that held the sin/cos encoder's magnetic shaft component. In practice, these two components proved difficult to align, causing degraded performance of the sin/cos encoder. The ankle actuator's solid shaft ensures the encoder magnet stays aligned with the read head.

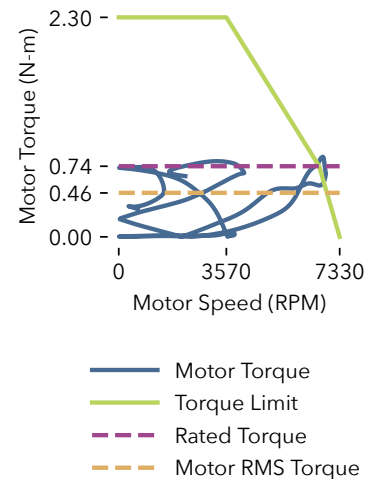


Figure 3.7: Ankle motor torque required to reproduce the running trajectory recorded by Novacheck [1998] assuming a parallel spring stiffness of $267 \text{ N}\cdot\text{m}/\text{rad}$ and a gear efficiency of 75%.

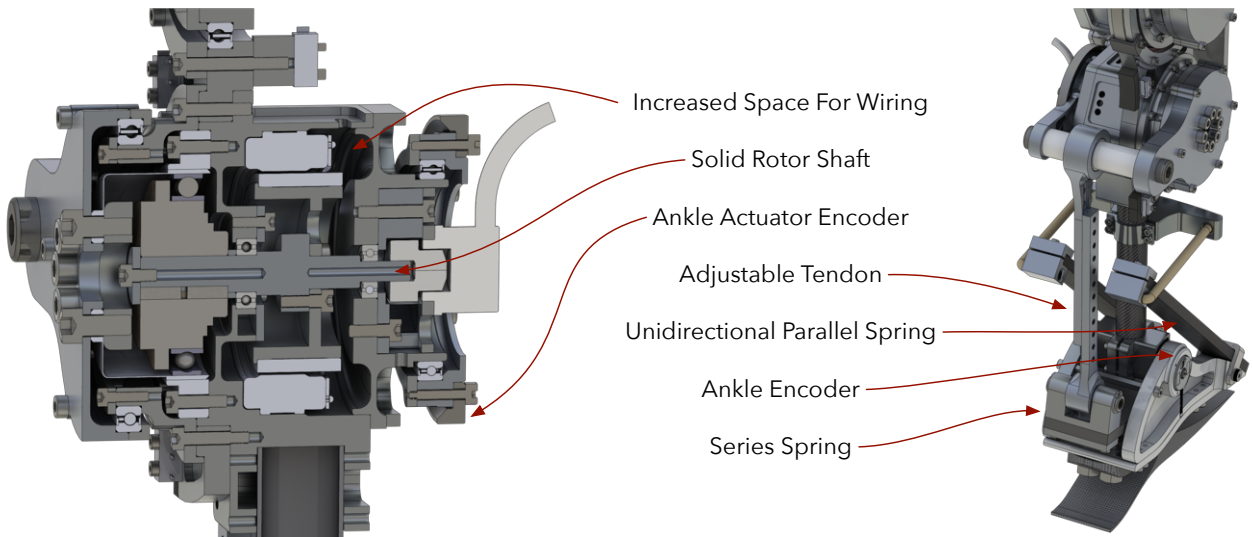


Figure 3.8: Internal and external design of the ankle joint.

As we did for the knee series spring, we again determine an acceptable ankle spring stiffness by performing an impact simulation. For the ankle, we simulate an 80 kg person stepping on the prosthesis when the motor driver provides the ankle motor with zero applied voltage. Figure 3.9 shows the simulation environment. From this simulation we find that a spring stiffness of about $1000 \text{ N}\cdot\text{m}/\text{rad}$ should sufficiently protect the ankle gear set from impacts. This estimate is likely softer than necessary due to the additional series compliance in the amputee's socket and the composite foot that are not included in the simulation. Repeating the bandwidth calculation we performed for the knee spring, we estimate the ankle bandwidth may be around 5.9 Hz. This value exceeds the required torque bandwidth of 3.5 Hz given by Au and Herr [2008] (obtained by analyzing the torque data for walking reported by Winter [2009]).

3.1.3 Ground Reaction Force Sensing

To measure ground reaction forces, we measure the deflection in the prosthesis' fiberglass foot (Freedom Innovations Pacifica LP). We measure this deflection by embedding Hall effect sensors and magnets in the foot. Figure 3.10 shows the measured heel and toe GRF signals during a single walking stride.

3.2 Series Elastic Actuator Control

To control the prosthesis we use Simulink Real-Time (Mathworks, USA), which samples all sensors (joint encoders, IMU on thigh, force sensors in foot), computes the desired torques for the knee and ankle joints using a mid-level control strategy (section 2.2), runs the low-level SEA control, which calculates the motor velocity needed to achieve these desired torques, and finally sends the velocity commands to the motor controllers at a rate of 1 KHz. Here, we describe the low-level SEA control.

First, in order to ensure the safety of both the user and the prosthesis, the SEA controller saturates the desired torque commanded by the mid-level controller. During normal operation, we allow a maximum of $\pm 100 \text{ N}\cdot\text{m}$ of torque at the knee and $\pm 150 \text{ N}\cdot\text{m}$ of torque at the ankle. Furthermore, when either joint passes within 5 degrees of its joint limits, a software joint limit stop is activated that calculates torques that prevent the actuator from damaging itself. The joint limit torque is inspired by the limit torque used in the neuromuscular model simulation presented in section 4.1 and takes the form

$$\tau_{\lim} = k_{\lim} \Delta\theta_{\lim} (1 + \dot{\theta}_{\lim}/\dot{\theta}_{\max}) (\Delta\theta_{\lim} > 0) (\dot{\theta}_{\lim}/\dot{\theta}_{\max} > -1), \quad (3.3)$$

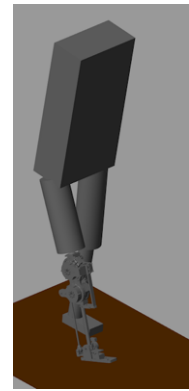


Figure 3.9: Impact simulation we used to determine appropriate series spring stiffness.

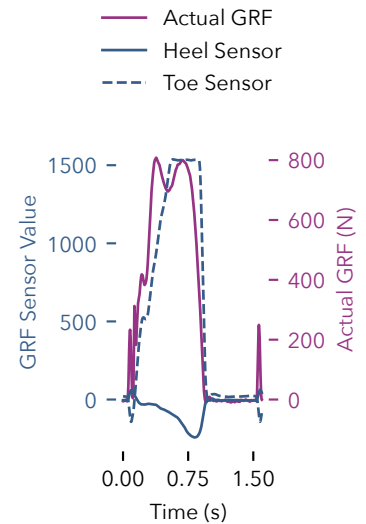


Figure 3.10: GRF sensor readings compared to ground truth GRF data

where k_{lim} is the joint limit stiffness, $\Delta\theta_{\text{lim}}$ is the penetration of the joint into the limit region, $\dot{\theta}_{\text{lim}}$ is the penetration velocity, and $\dot{\theta}_{\max}$ defines the retraction velocity at which the limit torque drops to zero. The knee extension limit activates below 5 degrees of flexion at which point above torque is added to the desired torque. The knee flexion limit is set to 90 degrees beyond which the limit torque upper bounds the desired knee torque. For the ankle joint, the flexion and extension limits activate at ± 20 degrees beyond which the limit torque upper and lower bound the desired ankle torque respectively.

Next, to improve the behavior of the prosthesis knee during swing, damping compensation in proportion to the knee velocity is added to the desired knee torque to compensate for friction and damping in the knee bearing. Finally, after saturation and friction compensation, a low pass filter is applied to ensure the derivatives of the desired torque are smooth and to remove frequencies that may excite the SEA spring. For both joints we use second order Butterworth filters with a cutoff frequency of 25 Hz at the knee and 20 Hz at the ankle.

Next, to achieve the desired torque τ_{des} in the SEA spring, we implement an SEA control similar to that used in Schepelmann et al. [2012]. The control uses proportional feedback to calculate the desired velocity needed to achieve the desired load torque:

$$\dot{\theta}_{\text{des}} = k_p(\tau_{\text{des}} - \tau_{\text{meas}}) \quad (3.4)$$

where $\dot{\theta}_{\text{des}}$ is the desired motor velocity and τ_{meas} is the measured torque. As shown in fig. 3.11, the torque on the load can be measured through the deflection of the SEA spring as $\tau_{\text{meas}} = k(\theta_l - \theta_m)$ where θ_l is the position of the load side of the spring and θ_m is the position of the motor side. To increase performance, we also add a feed-forward velocity term to the feedback term. We derive this term by differentiating the desired torque on the load and solving for the motor velocity

$$\dot{\tau}_{\text{des}} = k(\dot{\theta}_l - \dot{\theta}_m) \quad (3.5)$$

$$\implies \dot{\theta}_m = \frac{\dot{\tau}_{\text{des}}}{k} + \dot{\theta}_l. \quad (3.6)$$

Making the total desired velocity,

$$\dot{\theta}_{\text{des}} = k_p(\tau_{\text{des}} - \tau_{\text{meas}}) + \frac{\dot{\tau}_{\text{des}}}{k} + \dot{\theta}_l. \quad (3.7)$$

The motor controllers used on the prosthesis (Elmo Motion Control Gold Series) also accept a feed forward torque command, which can help achieve desired velocities more quickly. To derive the feed forward motor torque we refer to the motor dynamics depicted in fig. 3.11. The dynamics of the motor rotor are

$$\eta\tau_m - \tau_l - b_m\dot{\theta}_m = J_m\ddot{\theta}_m \quad (3.8)$$

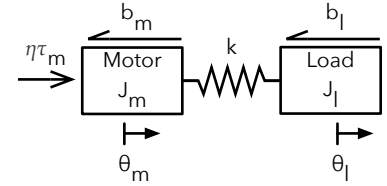


Figure 3.11: Dynamics model used to derive sea control. θ_m is the post-gearbox motor angle, J_m and b_m are the reflected motor inertia and damping, θ_l is the load angle, J_l and b_l are the load inertia and damping respectively. k is the SEA spring stiffness. τ_m is the motor torque applied to the motor rotor and η captures the efficiency of the motor torque transmission.

Where η is the efficiency of gear set and τ_m is the motor torque.

Solving for the motor torque yields

$$\tau_m = \frac{1}{\eta} (J_m \ddot{\theta}_m + b_m \dot{\theta}_m + \tau_l) \quad (3.9)$$

To eliminate the motor velocity and acceleration from the right side of the equation, we calculate the second derivative of the desired load torque

$$\ddot{\tau}_{des} = k(\ddot{\theta}_l - \ddot{\theta}_m) \quad (3.10)$$

$$\implies \ddot{\theta}_m = \frac{\ddot{\tau}_{des}}{k} + \ddot{\theta}_l, \quad (3.11)$$

and substitute eqs. (3.6) and (3.11) into eq. (3.9) to arrive at the final feed forward motor torque

$$\tau_m = \frac{1}{\eta} \left(J_m \left(\frac{\ddot{\tau}_{des}}{k} + \ddot{\theta}_l \right) + b_m \left(\frac{\dot{\tau}_{des}}{k} + \dot{\theta}_l \right) + \tau_l \right). \quad (3.12)$$

The final two steps of the SEA control are to saturate and low pass filter the desired joint velocities and feed forward motor torques to ensure safety and suppress excitatory frequencies. Knee velocities are saturated to lie within $\pm 9.95 \text{ rad/sec}$ and ankle velocities are saturated to lie within $\pm 6.96 \text{ rad/sec}$. Furthermore, if a joint violates specified hard constraint limits, the desired velocities are saturated to zero to prevent further constraint violation. For the knee joint, the flexion limit is set to 90 degrees and the extension limit is -2 degrees. For the ankle joint the flexion/extension limits are set to ± 30 degrees respectively. The saturated desired motor velocities and feed forward motor torques are then low pass filtered with second order Butterworth filters. For the knee, we use a cutoff frequency of 100 Hz and for the ankle we use a cutoff frequency of 50 Hz.

3.3 Performance Evaluation

Figure 3.12 shows the instantiation of the prosthesis design used for the results presented in this thesis. As large ankle torques were not required for the experiments conducted in this thesis, the optional unidirectional ankle springs were not installed. Of crucial importance for the work presented in this thesis is that the prosthesis faithfully reproduce the torques commanded by the mid-level control. This is important so that we can ensure differences between different mid-level control strategies are due to the differences in those strategies, and not due to an inability of the prosthesis to follow the desired behaviors.

We test the ability of the manufactured prosthesis to reproduce desired torques through three experiments: First, we collect data to

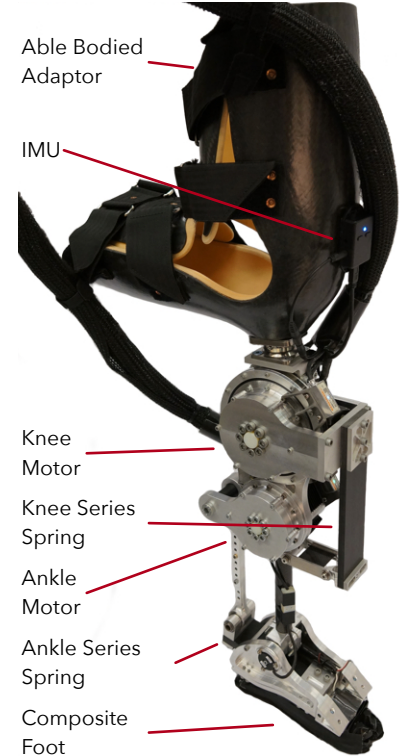


Figure 3.12: Prosthesis configuration used for experiments. An IMU attached on the thigh measures the thigh angle. Note: the optional unidirectional ankle springs were not installed for experiments presented in this thesis as the ankle motor alone produces sufficient torque for the results presented herein.

construct a Bode plot of the torque tracking behavior to confirm that the bandwidth of the actuators exceeds the desired values in table 3.1. Second, we test the ability of the prosthesis to track zero torque as a function of input disturbance frequency. And third, we investigate the ability of the prosthesis to follow the desired torques during a typical bout of walking.

3.3.1 Torque Tracking Bode Plot

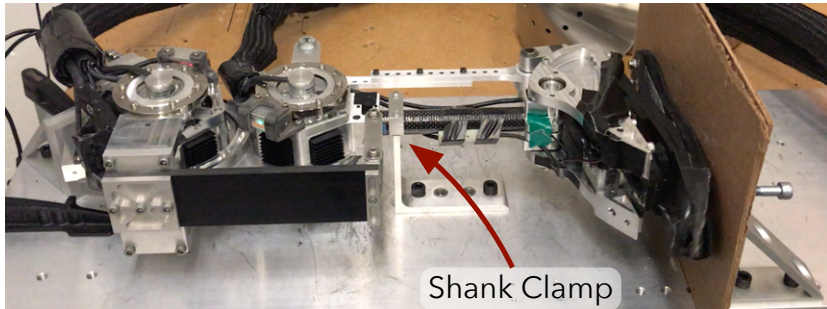


Figure 3.13: Fixture for testing bandwidth of actuators. The knee was constrained by a clamp on the shank. The ankle was constrained by a floor under the foot.

To measure the torque tracking bandwidth of the prosthesis' knee and ankle actuators, we construct bode plots of the transfer function between measured and desired torque. For this purpose, we constrain the prosthesis in the fixture shown in fig. 3.13. In this fixture, the knee joint is rotationally constrained by a clamp around the prosthesis' shank and the ankle joint is constrained by a floor under the foot. To construct the bode plot, we repeatedly command sinusoidal desired torques of varying frequencies ω and observe the resulting measured torques. We perform nonlinear least squares regression to identify the amplitude and phase shift parameters of the function $f(t) = A \sin(\omega t + \phi)$, where A is the amplitude and ϕ is the phase shift, such that the function fits the desired and measured torques. Finally, we calculate the Gain, $G(\omega) = 20 \log_{10}(A_{\text{meas}}/A_{\text{des}})$ and the phase shift, $\phi(\omega) = \phi_{\text{meas}} - \phi_{\text{des}}$, between the measured and desired signals at each frequency. For both joints, we construct Bode plots at two amplitudes of desired torque, a common amplitude of 20 N · m and at the root mean square (RMS) torques during stance for that joint.² For the knee joint we sweep frequencies in the range 1-35 Hz in 1 Hz increments, and for the ankle we sweep frequencies in the range 1-20 Hz.

Figure 3.14 shows the resulting knee and ankle bode plots at the two tested amplitudes. We define the bandwidth of the actuator as the frequency of the desired torque at which the gain falls below -3 dB or the phase lag falls below -180 deg , whichever comes first. We also report the lower of the two bandwidth values obtained

² 11.5 N · m for the knee, 55.6 N · m for the ankle according to data from Bovi et al. [2011] for 80 kg person

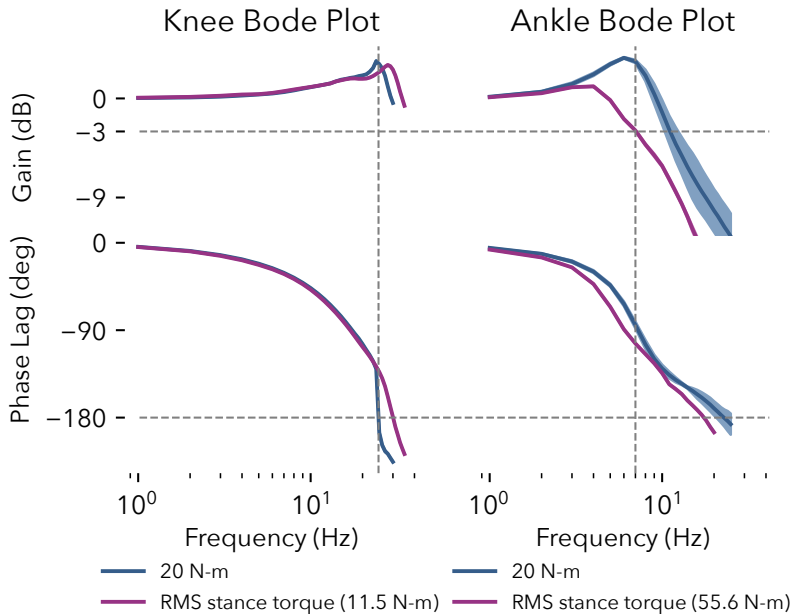


Figure 3.14: Experimentally obtained bode plots of knee and ankle actuator torque. Knee is phase limited at 24 Hz while the ankle is gain limited at 7 Hz.

from the 20 N·m or RMS torques. For the knee joint, we see that the bandwidth is phase limited at 24 Hz by the 20 N·m signal. The ankle bandwidth is gain limited at 7 Hz by the RMS stance torque signal. The measured bandwidth of the knee and ankle actuators is higher than the desired values based on able-bodied walking data.³

³ compare table 3.1 desired knee bandwidth from [Sergi et al., 2012], desired ankle bandwidth from Au and Herr [2008]

3.3.2 Zero Torque Tracking

Also important is the ability of the prosthesis to track the desired torque in the presence of external disturbances. To test this ability, we removed the shank clamp and floor from the fixture shown in fig. 3.13 and commanded zero desired torque to the ankle and knee joints. We then manually moved each joint in a sinusoidal motion while slowly increasing the frequency. Figure 3.15 shows the angle of each joint during the experiment and the approximate frequency of the motion, computed by inverting the time between peaks of the joint angle. In the second row of plots, we show the resulting measured torque. At 3 Hz the peak knee torque is roughly 6.5 N·m and the peak ankle torque is roughly 20 N·m. The knee peak knee torque is significantly less because knee actuator uses a 50:1 gear reduction as opposed to a 100:1 reduction in the ankle, resulting in less reflected inertia. The peak measured torque of both joints is less than 20% of the peak torque during normal walking.

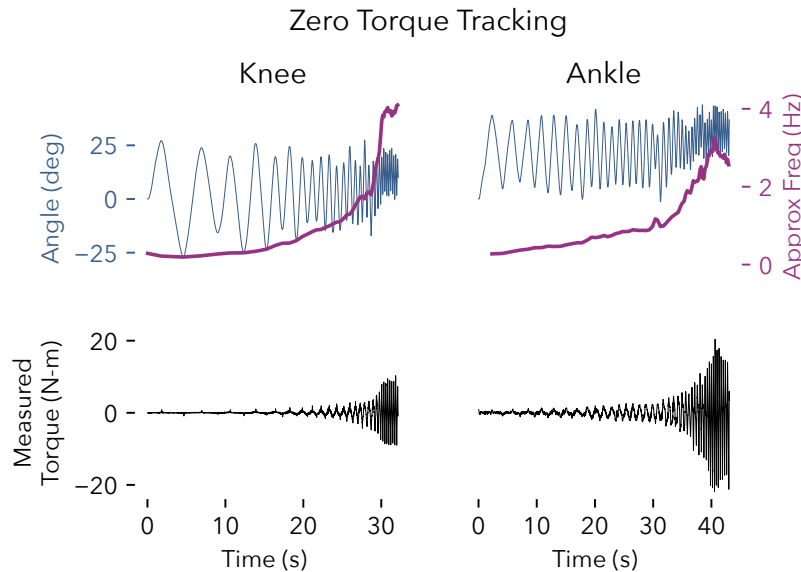


Figure 3.15: Zero torque tracking of knee and ankle joints. The prosthesis was fixed to a rigid mount and commanded to maintain zero net joint torque while the knee and ankle joints were manually oscillated (blue) by hand at increasingly fast rate (purple). The resulting measured torque is shown in the second row of axes in black.

3.3.3 Walking Torque Tracking

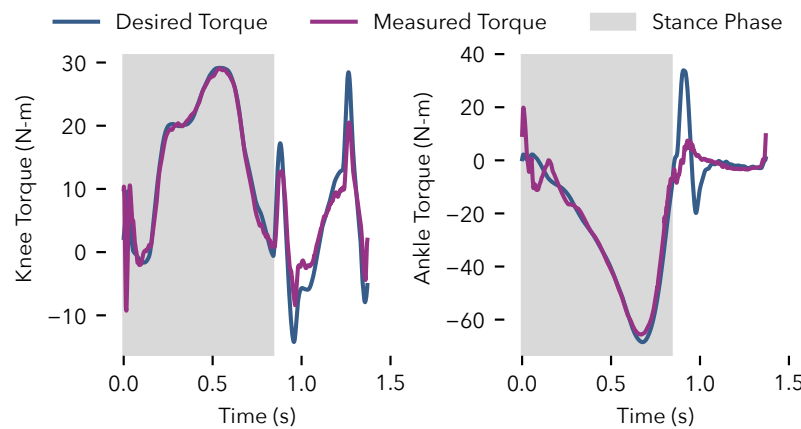


Figure 3.16: Knee and ankle torque tracking during a typical step. Torque tracking during stance is significantly better than during swing due to the significantly increased load inertia during stance (see table 3.2). During swing, trajectory tracking performance is prioritized.

Finally, we show the torque tracking performance of the prosthesis during normal walking. Figure 3.16 shows the desired and measured torque during a typical stride at a gait speed of 0.8 m/s while table 3.2 shows the median RMS torque tracking error during stance and swing over 1 min of walking. For both joints we see that torque tracking during stance is substantially better than during swing. This is the case for two reasons: First, during stance, the load inertia is significantly increased, as it primarily is comprised of the mass of

the user. Consequently, the SEA dynamics are slower and easier to control. In contrast, during swing, the load inertia is primarily the inertia of the prosthesis itself. This primarily affects the ankle, as the inertia of the foot is relatively small. Second, during swing the control's primary objective is to follow a desired swing trajectory, (see section 4.6 for more details). In this phase, the desired torque is generated by a PD feedback + feedforward term to track the desired trajectory. Consequently, the desired torques may not necessarily be feasible if the gains are high, as in the case of the of desired ankle torque during swing.

RMS Error (N-m)	Knee	Ankle
Stance	2.20	4.85
Swing	3.82	10.15

Table 3.2: Median root mean squared (RMS) torque tracking error during stance and swing

4

Neuromuscular Model

In the first part of this thesis, we investigate the ability of neuromuscular reflex control to improve amputee gait robustness. To this end, here we provide a more detailed review the neuromuscular model components on which we base our prosthesis control. Four parts comprise the model: a mechanical simulation environment we use to obtain simulation results (section 4.1), biological motors modeled by the hill muscle model that apply torques to joints (section 4.2), and finally functionally-motivated stance (section 4.3) and swing (section 4.4) reflexes that implement the key behaviors required for walking.

4.1 Mechanical Model

To obtain the simulation results we present in chapter 5, we construct a mechanical model in the Matlab Simscape Multibody™ environment similar to those presented in Geyer and Herr [2010], Song et al. [2013], Song and Geyer [2015]. This model represents the seven link biped in fig. 4.1 and includes two legs with thigh, shank, and foot segments as well as a lumped head-arms-trunk (HAT) segment. Table 4.1 lists the segment lengths, center of mass and joint locations measured from the distal end, masses, and inertias that approximate those of a 80 kg, 1.8 m tall person.

The mechanical model interacts with the environment through ground reaction forces on the toes and balls of the feet. Specifically,

	Feet	Shanks	Thighs	HAT
l (cm)	20	50	50	80
d_{COM} (cm)	14	30	30	35
d_{Joint} (cm)	16	50	50	
m (kg)	1.25	3.5	8.5	53.5
J (kg)	0.005	0.05	0.15	3

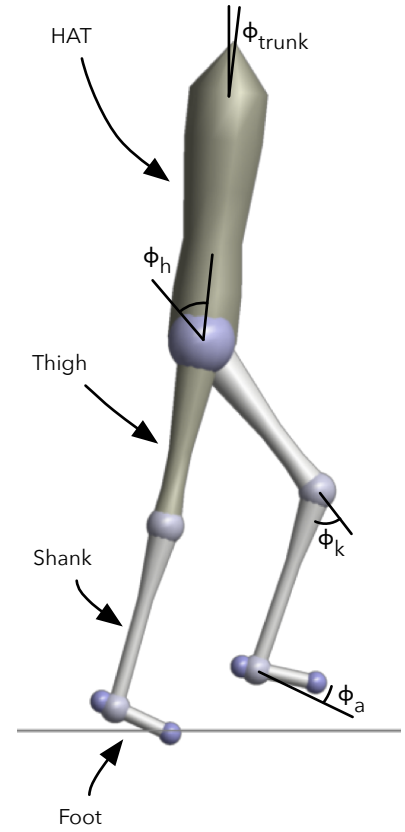


Figure 4.1: The skeletal model we use to simulate neuromuscular reflex control. The model consists of seven segments: left and right feet, shanks, and thighs, as well as a lumped head-arms-trunk (HAT) segment. Flexion joint angles are positive, extension joint angles are negative, and the zero angle configuration represents standing.

Table 4.1: Segment lengths (l_s), center of mass (d_{COM}) and joint (d_{Joint}) locations measured from the distal end, masses (m), and inertias (J) approximated from Günther and Ruder [2003].

we use a 2-dimensional reduction of the 3D ground contact model presented in Song and Geyer [2013] to calculate forces in the normal and tangential directions with respect to the terrain. In the normal direction the force is

$$F_n = k_n \Delta n_c (1 + \dot{n}_c / v_{\max}) (\Delta n_c > 0) (\dot{n}_c / v_{\max} > -1), \quad (4.1)$$

where $k_n = 78.45 \text{ N/mm}$ is the stiffness coefficient in the normal direction and Δn_c and \dot{n}_c are the penetration direction and velocity in the normal direction. The form of the normal force is inspired by Günther and Ruder [2003] and Scott and Winter [1993] and represents a linear spring with multiplicative damping. $v_{\max} = 3 \text{ cm/s}$ represents the maximum recovery velocity of the ground. If \dot{n}_c exceeds this velocity, ground contact is lost.

In the tangential direction, a state machine switches between two force models representing sliding and static friction. Sliding friction is given by

$$F_{t,slide} = -\text{sign}(\dot{t}_c) \mu_{slide} F_n \quad (4.2)$$

while static friction is given by

$$F_{t,static} = -k_t \Delta t_c \left(1 + \text{sign}(\Delta t_c) \frac{\dot{t}_c}{v_{\max}} \right), \quad (4.3)$$

where Δt_c is the penetration in the tangential direction \dot{t}_c is the penetration velocity, $\mu_{slide} = 0.8$ is the sliding coefficient of friction, and $k_t = 78.45 \text{ N/mm}$ is the stiffness coefficient in the tangential direction.

The contact model begins in the sliding mode and switches to the static mode if $\dot{t}_c < 1 \text{ cm/s}$. It switches back to the sliding mode when $|F_{t,static}| < \mu_{static}|F_n|$, where $\mu_{static} = 0.9$.

Finally, the biped skeletal model includes soft joint limits to represent the skeletal joint limits on the knee, ankle, and hip joints. The functional form of the soft limit joint torque is identical to that of the normal ground reaction force given by eq. (4.1).

$$\tau_{jl} = k_{jl} \Delta \phi_{jl} (1 + \dot{\phi}_{jl} / \phi_{\max}) (\Delta \phi_{jl} > 0) (\dot{\phi}_{jl} / \phi_{\max} > -1), \quad (4.4)$$

where $k_{jl} = 0.3 \text{ N}\cdot\text{m}/\text{deg}$ is the joint stiffness $\Delta \phi$ and $\dot{\phi}_{jl}$ are the joint limit penetration angle and velocity respectively, and $\phi_{\max} = 1 \text{ deg/s}$ is the maximum joint limit retraction velocity. Table 4.2 lists the engagement angles for the joint limits.

To obtain simulation results, we simulate the mechanical system with the ode15s variable step solver. We set the maximum step size to 10 ms, relative error tolerance to 10^{-4} , and absolute error to 10^{-6} .

Joint	ext. lim.	flex lim.
hip		50
knee	5	
ankle	-40	20

Table 4.2: Joint limits for the hip, knee, and ankle joints listed in degrees. Positive joint angles represent flexion and negative joint angles represent extension (see fig. 4.1).

4.2 Hill Muscle Models

Our proposed transfemoral prosthesis control is comprised of biological muscle actuators that are stimulated according to hypothesized reflex pathways. Specifically, we use a Hill-type *muscle tendon unit* (MTU) first described by Hill [1938]. It is comprised of a contractile element (CE) that represents muscle fibers and produces force when activated, a parallel elastic (PE) element that represents the stiffness of the collagen tissue between muscle fascicles, and series elastic (SE) element that models tendon stretch. Figure 4.2 shows the arrangement of these elements. Note that the PE and SE both are unidirectional springs with engagement lengths of l_{opt} and l_{slack} respectively.

The CE generates force according to

$$F_{\text{CE}} = F_{\max} A f_l(l_{\text{CE}}) f_v(v_{\text{CE}}). \quad (4.5)$$

In this equation, the force generated by the CE, F_{CE} , is the maximum isometric (constant length) force, F_{\max} , multiplied by activation, A , the force-length, $f_l(\cdot)$, and force-velocity, $f_v(\cdot)$, relationships of the CE. The activation, A , is a low-pass filtered version of the stimulation signal muscle $S(t)$ generated by the muscle reflexes we will detail in the next section. This filter, given by $A(t) = S - \tau \dot{A}(t)$ with time constant τ , represents the diffusion dynamics of calcium ions that activate binding sites in the muscle fibers.

The binding sites are where overlapping actin and myosin filaments attach and generate pulling force. The contractile element length of l_{opt} corresponds to maximum overlap between these filaments. Therefore, as the muscle length moves away from l_{opt} , its force production capacity decreases leading to the force-length relationship shown in fig. 4.3. We model the force-length relationship via a bell curve

$$f_l(l_{\text{CE}}) = \exp \left(\ln(0.05) \left| \frac{l_{\text{CE}} - l_{\text{opt}}}{w l_{\text{opt}}} \right|^3 \right). \quad (4.6)$$

The velocity-dependent filament attachment probabilities give rise to a force-velocity relationship shown in fig. 4.4. The following expression captures this relationship.

$$f_v(v_{\text{CE}}) = \begin{cases} \frac{v_{\max} - v_{\text{CE}}}{v_{\max} + K v_{\text{CE}}}, & \text{if } v_{\text{CE}} < 0 \\ N + (N-1) \frac{v_{\max} + v_{\text{CE}}}{7.56 K v_{\text{CE}} - v_{\max}}, & \text{if } v_{\text{CE}} \geq 0 \end{cases} \quad (4.7)$$

In this expression, K is a shape parameter and N determines the force amplification when the contractile element is lengthening. The force-velocity relationship acts as a multiplicative damper causing the

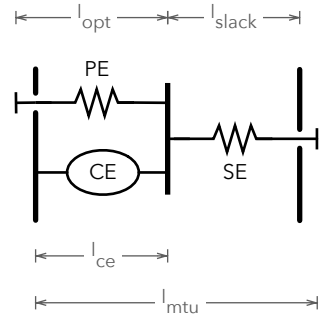


Figure 4.2: Hill-type muscle tendon unit with contractile element (CE), parallel elasticity (PE), and series elasticity (SE).

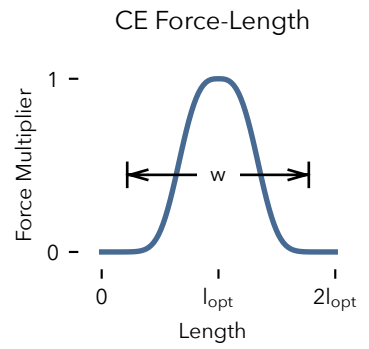


Figure 4.3: Force-length relationship of the CE.

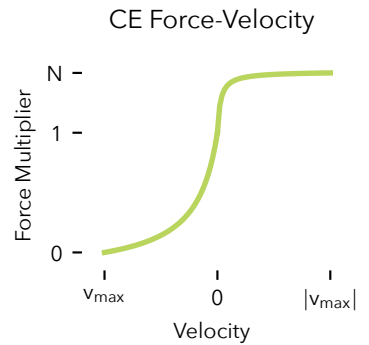


Figure 4.4: Force-velocity relationship of the CE.

Param	Value	Param	Value
τ	0.01 s	$l_{\text{opt}}^{\text{ham}}$	0.10 m
w	0.56	v_{\max}^{ham}	-1.2 m/s
K	5	F_{\max}^{ham}	3000 N
N	1.5	$l_{\text{slack}}^{\text{ham}}$	0.31 m
ϵ_{PE}	w		
ϵ_{SE}	0.04		

Table 4.3: Neuromuscular parameters for shared entities (left) and the hamstring muscle (right)

CE to produce more contractile force when it is lengthening and less as it contracts.

We model both passive elements, the PE and SE, using the same functional form representing a unidirectional, stiffening spring, the behavior of which is shown in fig. 4.5. The expressions for the elastic force produces by these elements are

$$F_{\text{PE}}(l_{\text{CE}}) = F_{\max} \left(\frac{l_{\text{CE}} - l_{\text{opt}}}{\epsilon_{\text{PE}} l_{\text{opt}}} \right)^2 (l_{\text{CE}} > l_{\text{opt}}) \quad (4.8)$$

$$F_{\text{SE}}(l_{\text{SE}}) = F_{\max} \left(\frac{l_{\text{SE}} - l_{\text{slack}}}{\epsilon_{\text{SE}} l_{\text{slack}}} \right)^2 (l_{\text{SE}} > l_{\text{slack}}). \quad (4.9)$$

The left-hand side of table 4.3 lists the parameters common among all seven muscles of each leg of the neuromuscular model. On the right-hand side of the table, we list four muscle-specific parameters for hamstrings muscle. For a complete list of muscle parameters please refer to Song and Geyer [2015].

The full biped model, shown in fig. 4.6, includes seven Hill-Type muscle-tendon units: soleus, gastrocnemius, tibialis anterior, vastus, hamstring, hip flexors, and gluteus. The length of these MTUs is related to the joint angles according to the variable-length moment arms $r_{\text{mtu}}^j(\phi^j)$ for each muscle about each joint. For example, the

PE/SE Force-Length

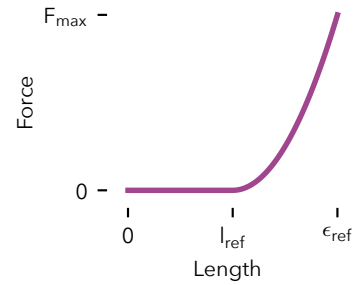


Figure 4.5: PE and SE force length relationship. For the PE, $l_{\text{ref}} = l_{\text{opt}}$ and $\epsilon_{\text{ref}} = \epsilon_{\text{PE}}$. Likewise, for the SE, $l_{\text{ref}} = l_{\text{slack}}$ and $\epsilon_{\text{ref}} = \epsilon_{\text{SE}}$.

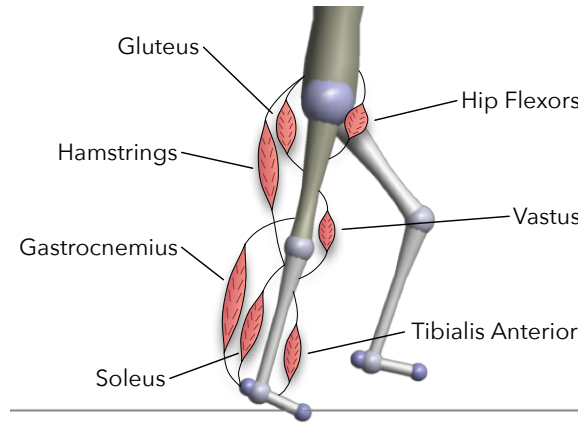


Figure 4.6: Biped walking model with labeled muscles.

length of a biarticular muscle spanning joints j and k is

$$l_{\text{mtu}} = l_{\text{opt}} + l_{\text{slack}} + \rho \left(\int_{\phi_0^j}^{\phi^j} r_{\text{mtu}}^j(\phi^j) d\phi^j + \int_{\phi_0^k}^{\phi^k} r_{\text{mtu}}^k(\phi^k) d\phi^k \right). \quad (4.10)$$

Where ρ is a parameter that approximates the effect of the pennation angle of the muscle fibers and ϕ_0^j and ϕ_0^k are reference joint angles at which the MTU settles to its rest length ($l_{\text{opt}} + l_{\text{slack}}$). The variable length moment arms also govern the torque a muscle produces about a joint according to

$$\tau_{\text{mtu}} = r_{\text{mtu}}^j(\phi^j) F_{\text{mtu}}. \quad (4.11)$$

4.3 Stance Reflexes

During stance, hypothesized reflex feedback pathways stimulate the muscles of the leg. In general, a linear feedback law governs the stimulation $S^m(t)$ of muscle m ,

$$S^m(t) = S_0^m + \sum_n G_n^m \text{Pro}_n(t - \Delta t_n), \quad (4.12)$$

where S_0^m is a constant pre-stimulation, $\text{Pro}_n(t - \Delta t_n)$ is the time-delayed proprioceptive signal from muscle n , and G_n^m is the gain on that signal. The proprioceptive signal can take the form of force feedback, $F_n^m(\cdot)$, which uses the time delayed tendon force, or length feedback, $L_n^m(\cdot) = l_n^{\text{CE}}(\cdot) - \text{off } l_n^m$, which uses the difference between the length of the contractile element of muscle n and an offset length $\text{off } l_n^m$.

The time delay we apply to proprioceptive signals estimate the round-trip neural signal transmission delay of afferent signals from muscle spindles and Golgi tendons to the spine and efferent signals back to the muscles. For ankle muscles, the soleus, tibialis anterior, and gastrocnemius, the time delay is $\Delta t_n = 20$ ms. For knee muscles, the vastus and hamstrings, it is $\Delta t_n = 10$ ms. For the hip muscles, the hamstrings, gluteus, and hip flexors, the time delay is $\Delta t_n = 5$ ms. We will denote time delayed signals using $t_1 = t - 20$ ms, $t_m = t - 10$ ms, and $t_s = t - 5$ ms.

The reflexes encode several key functions of legged locomotion: generating compliant leg behavior, preventing knee overextension, and balancing the trunk. The first function, generating compliant leg behavior, is achieved via positive force feedback on the monoarticular leg extensors: the soleus, vastus, and gluteus. For example, the reflexes stimulate the vastus in part by

$$S^{\text{vas}}(t) = S_0^{\text{vas}} + G_{\text{vas}}^{\text{vas}} F_{\text{vas}}(t_m) + \dots. \quad (4.13)$$

To implement the second function, preventing knee overextension, the reflex control uses two strategies. First, positive force feedback of the biarticular gastrocnemius and hamstrings muscles helps counteract the tendency for knee overextension caused by ankle plantarflexion and hip extension torques respectively. For example, the gastrocnemius has a force feedback reflex,

$$S^{\text{gas}}(t) = S_0^{\text{gas}} + G_{\text{gas}}^{\text{gas}} F_{\text{gas}}(t_l), \quad (4.14)$$

that flexes the knee as it contributes to ankle plantarflexion. The hamstring also has a positive force feed back

$$S^{\text{ham}}(t) = S_0^{\text{ham}} + G_{\text{ham}}^{\text{ham}} F_{\text{ham}}(t_s) + \dots \quad (4.15)$$

that counteracts knee extension caused by hip extension. Also, the hamstring force feedback helps prevent hip flexion caused by heel-strike.

A second mechanism further protects the knee by inhibiting the vastus stimulation in proportion to knee extension beyond a threshold, resulting in the complete vastus stimulation

$$S^{\text{vas}}(t) = S_0^{\text{vas}} + G_{\text{vas}}^{\text{vas}} F_{\text{vas}}(t_m) - G_{\text{knee}}^{\text{vas}} (\phi_{\text{knee}}(t_m) - {}^{\text{off}}\phi_{\text{knee}}) (\phi_{\text{knee}}(t_m) < {}^{\text{off}}\phi_{\text{knee}}) (\dot{\phi}_{\text{knee}}(t_m) < 0) \quad (4.16)$$

where ${}^{\text{off}}\phi_{\text{knee}}$ is the angle beyond which the vastus is inhibited.

The reflexes achieve the final function of balancing the trunk by proportional-derivative control that produces stimulations for the hip muscles (hip flexors, gluteus, and hamstrings) to stabilize the trunk at a reference lean. Because muscles can only provide pulling force, the proportional derivative control signal is distributed as hip flexor stimulation if the signal represents flexion torque and as simultaneous stimulation for the gluteus and hamstrings if it represents hip extension torque. For example, the complete hamstrings stimulation becomes

$$\begin{aligned} S^{\text{ham}}(t) = & S_0^{\text{ham}} + G_{\text{ham}}^{\text{ham}} F_{\text{ham}}(t_s) \\ & + \left\{ G_p^{\text{ham}}(\phi_{\text{trunk}}(t_s) - \phi_{\text{trunk}}^{\text{ref}}) + G_d^{\text{ham}} \dot{\phi}_{\text{trunk}}(t_s) \right\}_+ \end{aligned} \quad (4.17)$$

where the third term returns the positive reflex contribution from the trunk balance control.

The full set of stance reflexes are:

$$S^{\text{sol}}(t) = S_0^{\text{sol}} + G_{\text{sol}}^{\text{sol}} F_{\text{sol}}(t_1) \quad (4.18)$$

$$S^{\text{ta}}(t) = S_0^{\text{ta}} + G_{\text{ta}}^{\text{ta}} L_{\text{ta}}(t_1) - G_{\text{sol}}^{\text{ta}} F_{\text{sol}}(t_1) \quad (4.19)$$

$$S^{\text{gas}}(t) = S_0^{\text{gas}} + G_{\text{gas}}^{\text{gas}} F_{\text{gas}}(t_1) \quad (4.20)$$

$$S^{\text{vas}}(t) = S_0^{\text{vas}} + G_{\text{vas}}^{\text{vas}} F_{\text{vas}}(t_m) - G_{\text{knee}}^{\text{vas}} (\phi_{\text{knee}}(t_m) - {}^{\text{off}}\phi_{\text{knee}}) (\phi_{\text{knee}}(t_m) < {}^{\text{off}}\phi_{\text{knee}}) (\dot{\phi}_{\text{knee}}(t_m) < 0) \quad (4.21)$$

$$S^{\text{ham}}(t) = S_0^{\text{ham}} + G_{\text{ham}}^{\text{ham}} F_{\text{ham}}(t_s) + \left\{ G_p^{\text{ham}}(\phi_{\text{trunk}} - \phi_{\text{trunk}}^{\text{ref}}) + G_d^{\text{ham}} \dot{\phi}_{\text{trunk}} \right\}_+ \quad (4.22)$$

$$S^{\text{glu}}(t) = S_0^{\text{glu}} + G_{\text{glu}}^{\text{glu}} F_{\text{glu}}(t_s) + \left\{ G_p^{\text{glu}}(\phi_{\text{trunk}} - \phi_{\text{trunk}}^{\text{ref}}) + G_d^{\text{glu}} \dot{\phi}_{\text{trunk}} \right\}_+ \quad (4.23)$$

$$S^{\text{hfl}}(t) = S_0^{\text{hfl}} + \left\{ G_p^{\text{hfl}}(\phi_{\text{trunk}} - \phi_{\text{trunk}}^{\text{ref}}) + G_d^{\text{hfl}} \dot{\phi}_{\text{trunk}} \right\}_- \quad (4.24)$$

4.4 Swing Leg Control

During swing, the reflexes shape the natural double pendulum dynamics of the leg in order to achieve sufficient knee flexion, prevent toe scuffing, reach a target landing leg angle, and then extend the leg towards the ground. We here review an idealized control model, proposed in Desai and Geyer [2012], which proposes reflexes that directly apply torques to the hip and knee joints.

The idealized swing control comprises two layers. In the first layer, a leg placement policy,

$$\alpha_{\text{tgt}} = \alpha_0 + c_d d + c_v v, \quad (4.25)$$

prescribes leg angle for the leg to reach by the end of swing. We measure the leg angle between the hip-ankle line and horizontal as shown in fig. 4.7. In eq. (4.25), α_{tgt} is the target leg angle, α_0 is the default leg angle, d is the horizontal distance between the stance leg ankle and the model's center of mass, v is the velocity of the center of mass, and c_d and c_v are constant gain parameters. This policy is taken from Yin et al. [2007] and represents an empirical generalization of the leg placement strategies that recover the linear inverted pendulum model of human walking from disturbances [Kajita et al., 2001, Pratt et al., 2006].

The target angle generated by this policy forms a central input to the second layer comprised of hip and knee controls. The portion of this control that governs the knee action uses a finite state machine to switch between three phases. The first phase allows the knee to passively flex in response to hip moments generated at the onset of swing. If the passive knee flexion is insufficient (the foot swings forward with a tendency to scuff the ground), the control produces active flexion torque of the knee in proportion to the rate $\dot{\alpha}$

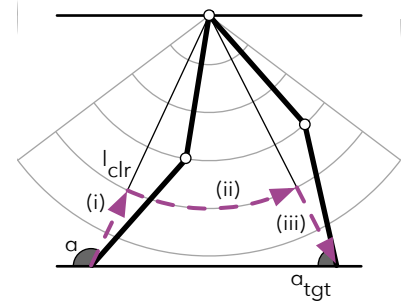


Figure 4.7: The idealized swing leg control guides the leg towards a desired landing leg angle α_{tgt} through three phases: (i) Flex the knee until it achieves a clearance leg length l_{clr} . (ii) Hold the leg length via knee damping. (iii) Stop and Extend the leg towards the ground when the leg reaches α_{tgt} . Figure reproduced from Desai and Geyer [2012].

of forward leg motion,

$$\tau_k^i = \begin{cases} 0, & \dot{\alpha} > 0 \\ -k^i \dot{\alpha}, & \dot{\alpha} \leq 0 \end{cases}, \quad (4.26)$$

where k^i is the flexion gain and the leg angle α is defined as the angle between the horizontal and the hip-ankle line.

The second phase activates when the leg length, defined as the distance between the hip and ankle, contracts below a threshold. In this phase, the knee torque is given by

$$\tau_k^{ii} = \begin{cases} -k_1^{ii} \dot{\phi}_k, & \dot{\phi}_k \geq 0 \\ -k_2^{ii} \dot{\phi}_k (\alpha - \alpha_{tgt}) (\dot{\alpha} - \dot{\phi}_k), & \dot{\phi}_k < 0 \text{ \& } \dot{\phi}_k < \dot{\alpha}, \\ 0, & \text{otherwise} \end{cases}, \quad (4.27)$$

where k_1^{ii} and k_2^{ii} are damping coefficients. The first case dampens knee flexion, while the second case dampens knee extension, but allows progressively more extension as the leg angle approaches its target. The modulation term ($\dot{\alpha} - \dot{\phi}_k$) prevents premature landing of the leg by damping the knee if it extends faster than the overall leg angle.

The third phase engages when the leg angle gets within a threshold of the target leg angle. The control then applies torque to stop and extend the knee,

$$\tau_k^{iii} = \begin{cases} k^{iii} (\alpha_{thr} - \alpha) \left(1 - \frac{\dot{\alpha}}{\dot{\alpha}_{max}} \right), & \alpha < \alpha_{thr} \text{ \& } \dot{\alpha} < \dot{\alpha}_{max}, \\ 0, & \text{otherwise} \end{cases}, \quad (4.28)$$

where $\dot{\alpha}_{max}$ is the maximum leg retraction velocity for which the stopping knee torque is applied. When this torque brings the leg velocity to zero, a knee extension torque is added,

$$\tau_k^{iii'} = \tau_k^{iii} - k^{ext} (l_0 - l), \quad (4.29)$$

where l_0 is the rest leg length, l is the current leg length, and k^{ext} is a proportional gain.

The swing leg control also specifies a hip torque in the form of a proportional derivative control on the leg angle,

$$\tau_h^\alpha = k_p (\alpha - \alpha_{tgt}) + k_d \dot{\alpha}. \quad (4.30)$$

This hip torque is supplemented by a feed forward term

$$\tau_h = \tau_h^\alpha - 2\tau_k^{iii} \quad (4.31)$$

that neutralizes the coupling dynamics between the knee and hip during the knee's stop and extend phase (Eq. 4.28).

4.5 Control for Simulation Experiments

In chapter 5, in order to assess potential benefits of using the neuromuscular model for prosthesis control, we perform simulated experiments of an amputee walking with a powered knee and ankle prosthesis. In those experiments, to generate the reference torques for the SEAs, we use a hybrid neuromuscular control that blends the muscle based stance-control (section 4.3) with the idealized swing leg placement control section 4.4.

For the stance control of the prosthesis, we utilize only muscles and reflexes of the lower leg: the Hamstring, Vastus, Gastrocnemius, Soleus, and Tibialis Anterior. These muscles are stimulated by eqs. (4.18) to (4.22). However, because the hamstring muscle spans the hip joint as well, and we do not wish to instrument the torso of the amputee user, we assume that the torso angle remains fixed at ϕ_{ref} , thereby reducing the hamstring stimulation to eq. (4.15).

Additionally, we make two modifications to the prosthesis-side swing leg control. First, on the prosthesis-side hip we remove the feed-forward term that neutralizes the disturbance created by the knee's stop and extend phase (eq. (4.31)), requiring that feedback control deal with this torque. Second, we do not use the adaptive leg placement policy of the swing control (eq. (4.25)) as the prosthesis does not have access to information about the amputee's center of mass and stance leg ankle position. Instead the prosthesis swing leg control employs a constant target leg angle, $\alpha_{tgt} = \text{const}$.

The torques produced by the swing controller augment the net torques produced by the Hill-type muscles and reflexes during stance. At heel strike, the control policy switches from using the swing leg control torques to the stance torques generated by the muscle models. In late stance, the policy mixes the torques specified by the stance and swing controllers by scaling the stance and swing torques and muscle stimulations in proportion to the normalized ground reaction force,

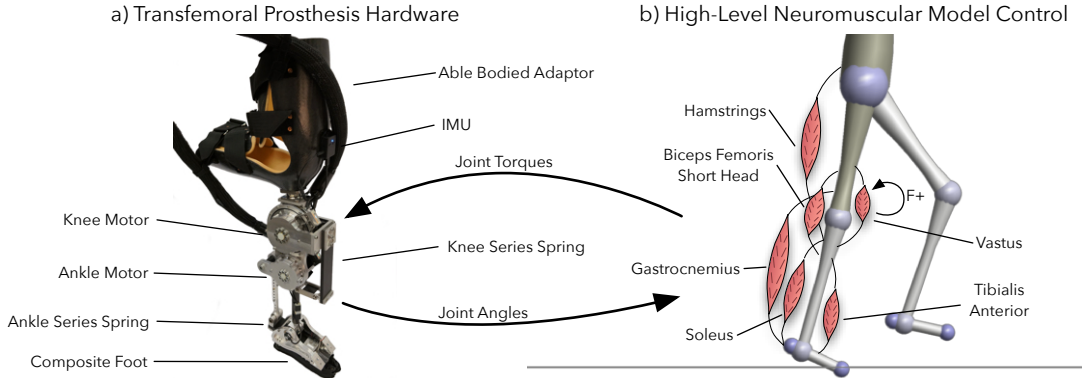
$$\tau_{\text{late stance}} = \tau_{\text{stance}}(GRF) + \tau_{\text{swing}}(1 - GRF), \quad (4.32)$$

$$S^m_{\text{late stance}} = S^m(GRF). \quad (4.33)$$

During swing, only the swing leg torques are used.

4.6 Control for Prosthesis Experiments

In chapters 6, 7, and 9 we perform experiments with the prosthesis hardware (detailed in chapter 3) with the neuromuscular model control. To operate this control on the prosthesis, we measure the prosthesis' joint angles using its onboard encoders, the user's thigh



angle using an inertial measurement unit, and ground reaction signals via hall effect sensors embedded in the foot. The measured joint angles feed into the muscle and reflex models in order to calculate the desired joint torques for the prosthesis, which are then achieved by the low-level SEA control (section 3.2). We use the ground reaction forces in

In chapters 7 and 9, the stance control follows the equations given in section 4.3 with the same modifications to the Hamstring as were made for the simulated experiments ($\phi_{\text{hip}} = \phi_{\text{ref}}$). In chapter 6 we experiment with an augmented version of the model that contains a Biceps Femoris Short Head, a monoarticular knee flexor (see fig. 4.8). This muscle helps prevent knee over extension via length feedback of the form

$$S^{\text{bfsh}}(t) = S_0^{\text{bfsh}} + G_{\text{bfsh}}^{\text{bfsh}} L_{\text{bfsh}}(t_1). \quad (4.34)$$

In this model, knee over extension is further prevented by inhibiting the vastus in proportion to the BFsH length. Consequently, the vastus stimulation becomes

$$S^{\text{vas}}(t) = S_0^{\text{vas}} + G_{\text{vas}}^{\text{vas}} F_{\text{vas}}(t_m) - G_{\text{vas}}^{\text{bfsh}} L_{\text{bfsh}}(t_m). \quad (4.35)$$

The properties of BFsH muscle (as well the properties of the other muscles) are based on human physiological parameters described in Song and Geyer [2015].

While our simulated experiments used the idealized reflexive swing control described in section 4.4, in our prosthesis experiments we instead use the minimum-jerk trajectory swing controller proposed by Lenzi et al. [2014b], which automatically adapts to walking speed and produces human-like trajectories. In our implementation, at every toeoff the control method generates a pair of minimum jerk trajectories for each joint: one that starts at the toeoff angle, velocity and acceleration and reaches peak knee flexion or ankle dorsiflexion and another that goes from the peak flexion state to the heel strike

Figure 4.8: (a) Custom transfemoral prosthesis with series elastic actuators. In experiments in this thesis, we use an adaptor to test the prosthesis with able-bodied subjects. (b) During stance, we propose a control based on a neuromuscular model of human physiology that generates joint torques through virtual muscles that are stimulated by hypothesized local reflex pathways.

state. The knee and ankle joints are set to 65 and 2 deg at peak flexion and 2 and -5 deg at heel strike respectively. The prosthesis then follows these desired joint angles via proportional/derivative feedback plus a model-based feedforward term. Combined, the feedback and feedforward terms specify the desired joint torques which the low-level SEA control tries to achieve (section 3.2). The use of the feed forward term and SEA torque control during swing allows the system to maintain a level of impact compliance despite following a trajectory.

The swing phase duration is set to 60% of the previous stance phase duration. In the chapters 6 and 7, we specified that the peak flexion angles for both the knee and ankle would be achieved simultaneously at 25% of swing. Later, in the work presented chapters 8 and 9, we delayed peak ankle flexion to 50% of swing to help avoid some of the frequent trips during swing that we discovered during the experiment presented in chapter 7. Chapter 8 also presents a more principled approach to avoiding these swing trips that explicitly predicts and plans to avoid premature foot contact with the ground.

We switched to this minimum jerk trajectory swing control approach for two reasons: First, preliminary experiments with the idealized swing control on the prosthesis hardware revealed that it was more sensitive to errors in the torque control. This seemed especially true in the second phase of the idealized swing control, in which small damping torques are used to control the rate of extension of the knee. In our SEA design (section 3.1), small errors in the torque measurement can build up over time due to encoder shift and thermal expansion. While these torque errors are insignificant during stance, they appeared to affect the behavior of idealized swing control. In contrast, a trajectory based approach can compensate for these errors through its explicit position feedback. Second, in our simulated experiments, we held the target angle α_{tgt} constant. However, in a real system, the target angle prediction should adapt to specific users and to variations in speed, terrain, and balance recovery intent. How best to predict this target angle remains an open research question and is not addressed in this thesis.

To switch between stance and swing phases, the prosthesis follows the state machine depicted in fig. 4.9. Transitions to stance occur when the leg is ahead of the frontal plane (leg angle $\alpha > 90^\circ$, see fig. 4.7) and when the ground reaction force (GRF) exceeds a hand-tuned threshold. Transitions to swing are allowed when the GRF falls below a threshold, the foot is behind the frontal plane ($\alpha < 90^\circ$), and the hip is flexing. For the experiments described in chapters 6 to 8 we use the prosthesis' built-in GRF sensors detailed in section 3.1.3. In later work (chapter 9), involving stepping on objects, we use the

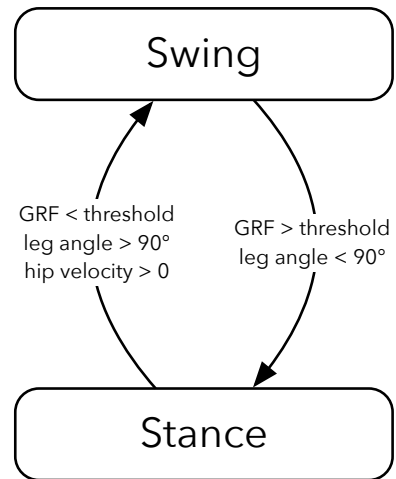


Figure 4.9: Universal stance/swing state machine utilized for all hardware experiments.

GRF readings from an instrumented treadmill, as they proved more reliable in this disturbed case.

5

Simulated Comparison of Neuromuscular and Impedance Controllers

Material in this section based partially on Thatte and Geyer [2016]¹ and Thatte and Geyer [2014]²

To evaluate the potential of neuromuscular prosthesis control to improve amputee gait robustness, we constructed a simulation of an amputee walking on a powered prosthesis and performed optimizations to identify parameters that lead to robust locomotion over rough terrain. We then compared the performance of the proposed control to that of impedance control and found that the proposed control improves robustness to elevation changes and unexpected deviations from nominal walking, suggesting that it may help amputees prevent trips and falls (fig. 5.1).

5.1 Methods

5.1.1 Simulation Environment

We studied the performance of the proposed transfemoral prosthesis controller in a simulation model of a unilateral amputee equipped with the proposed powered prosthesis. To more accurately model an amputee's anatomy, we severed the femur of the unimpaired human model 11 cm above the knee and attached the hamstring muscle to the distal end of the shortened bone as recommended in Brown et al. [2012]. This change converts the biarticular hamstring into a monoarticular muscle that only extends the hip. Next, we attached a model of the full prosthesis to the severed femur. The prosthesis modeled in this study is an earlier version of the prosthesis design presented in chapter 3, which uses the knee actuator design for both the knee and ankle joints. Our simulation of the prosthesis models the series elasticity, electrical dynamics, gear ratios, and resultant

¹ Nitish Thatte and Hartmut Geyer. Toward balance recovery with leg prostheses using neuromuscular model control. *IEEE Transactions on Biomedical Engineering*, 63(5):904–913, 2016

² Nitish Thatte and Hartmut Geyer. Towards local reflexive control of a powered transfemoral prosthesis for robust amputee push and trip recovery. In *2014 IEEE/RSJ International Conference on Intelligent Robots and Systems*, pages 2069–2074. IEEE, 2014

reflected inertias of the actuators, and assumes a low-level current-based SEA control achieves desired torques [Pratt and Williamson, 1995].

As a baseline to compare the performance of the proposed control, we also simulated the commonly-used impedance control method, which we reviewed in section 2.2.2, at the behavior level. Specifically, we implemented the impedance control presented in Sup et al. [2008] as it tended to perform better than other versions in our simulations. This control partitions the gait cycle into four phases. In each phase i , the torque of an actuated joint is governed by an impedance function

$$\tau_i = -k_{1,i}(\theta - \theta_{1,i}) - k_{2,i}(\theta - \theta_{2,i})^3 - b_i\dot{\theta}, \quad (5.1)$$

where θ is the joint angle, $\theta_{1,i}$ and $\theta_{2,i}$ are angle offsets, and $k_{1,i}$, $k_{2,i}$ and b_i are the impedance parameters.

5.1.2 Controller Optimization for Natural and Robust Walking

For both the hybrid neuromuscular controller and the impedance controller, we optimized control parameters to search for gaits that appear natural and are robust to disturbances. For the hybrid neuromuscular model, we optimized 53 parameters that include reflex feedback gains and swing leg control parameters for both the amputee and prosthesis as well as the SEA control gains. To reduce the number of parameters to optimize, we used fixed values for many parameters, such as the muscle properties and prestimulations. For the impedance controller, we optimized 59 parameters that include the reflex feedback gains and the swing leg control parameters for the amputee model, and the impedance parameters and SEA controller gains for the prosthesis. Again to reduce the number of parameters to optimize, any parameters set to according by Sup et al. [2008] were fixed to zero during the optimization.

We relied on the covariance matrix adaptation evolution strategy (CMA-ES) [Hansen, 2006] and performed optimization in two steps. In the first step, we searched for control parameters that generate a gait with natural kinematics and kinetics. To this end, we took advantage of the observation that human gait seems to result from minimizing metabolic energy consumption [McNeill Alexander, 2002], and used the cost of transport

$$Cost = \frac{W}{mgx} + \frac{1}{mgx} \int \left(c_1 \tau_{cmd}^2 + c_2 \tau_{limit}^2 \right) dt \quad (5.2)$$

as the optimization criterion. In the cost, W accounts for the energy consumption of both the modeled amputee's muscles and the prosthesis' virtual muscles according to Umberger et al. [2003], τ_{cmd} is the

sum of the torques commanded by the neuromuscular swing control or the impedance control, τ_{limit} is the sum of torques produced by the model's mechanical hard stops, which prevent knee and ankle hyperextension, m is the mass of the amputee, g is the gravitational acceleration, and x is the distance travelled in 20 seconds. The hand tuned constants, $c_1 = 0.1$ and $c_2 = 0.01$, ensure that the terms of the cost function have similar order-of-magnitude.

We ran the above optimization for 300 iterations, and used the best resulting set of control parameters to seed an optimization for robustness to unexpected changes in ground height. For this second step, the cost function was

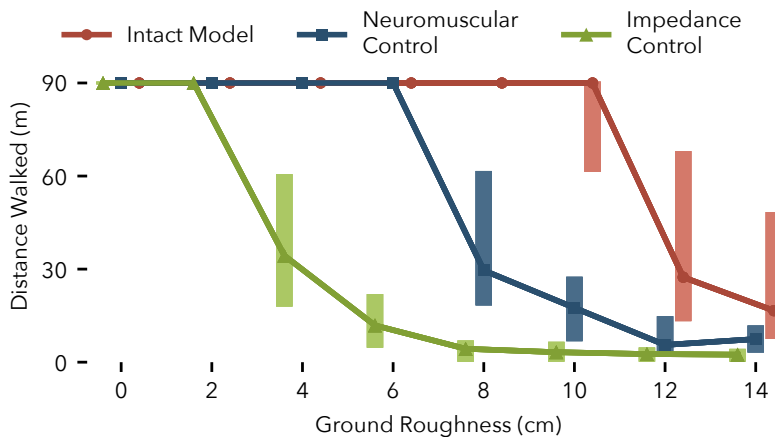
$$\text{Cost} = -x + c_3 \int \tau_{\text{limit}}^2 dt, \quad (5.3)$$

rewarding the distance travelled and penalizing joint hyperextension ($c_3 = 0.0005$). Instead of level ground, the simulations evaluating the cost were performed on terrain that is flat for the first 10 meters (to allow the model to reach steady walking) and then features steps, spaced one meter apart and drawn from a uniform random distribution. The width of the distribution grew at a rate of 2.5 cm per meter distance travelled, resulting in steps that grow progressively rougher the farther the model walks. To avoid overfitting, we performed the evaluation on five different terrains, resulting in an average cost. Like in the first step, the optimization was stopped after 300 iterations, resulting in the final, best set of control parameters.

5.2 Results

We evaluated the performance of the proposed control and of impedance control by having the amputee model walk on terrains that are flat for 10 meters and then feature steps drawn from uniform distributions for another 90 meters. The widths of the distributions are constant but varied among the terrains to test the control performance on steps of increasing steepness (0 cm to ± 14 cm, 2 cm increments, total of 8 terrains).

Figure 5.1 shows the distances the amputee model walks over 50 trials at each roughness level (proposed neuromuscular control in blue, impedance control in green). Most of the trials with the impedance-controlled prosthesis covered the full distance up to a roughness of 2 cm. At a roughness of 4 cm, however, the median distance drops to 34 m, which further declines as the roughness increases. In contrast, the prosthesis using the neuromuscular control, allowed the amputee model to walk the full distance up to a roughness of 6 cm. Moreover, neuromuscular control has a similar



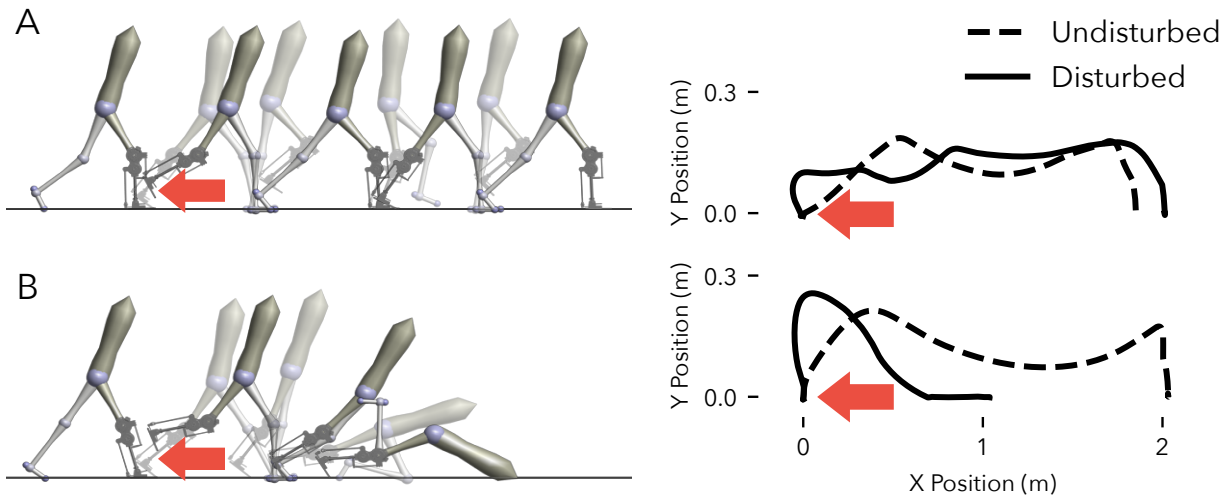
distribution of distances walked at a roughness of 8 cm as impedance control has at a roughness of 4 cm.

Although controlling the prosthesis with neuromuscular control substantially improves the robustness of the amputee model on rough terrain, the performance trails by a large margin that of an unimpaired model (fig. 5.1, red line), for which most of the trials covered the full distance up to a roughness of 10 cm. Limiting the swing leg placement targets in the neuromuscular prosthesis control to constant angles may account for some of this performance gap. In future work, we may overcome this limitation by estimating the amputee's center of mass velocity and stance ankle position so that the prosthesis control can take advantage of the full leg placement policy (eq. (4.25)). Other sources for the performance gap could stem from differences in the inertial properties between the prosthesis and the healthy leg, delay and inaccuracy in the series elastic actuator torque tracking, and the increased number of parameters in the asymmetric amputee model, which can reduce the quality of the optimized solutions.

A possible explanation for why the neuromuscular control produces more robust behavior than impedance control is the former's attempt to mimic the underlying dynamics and goals of human motor control rather than to track impedance behavior about a pre-defined motion for each individual joint. To illustrate this difference, we subjected the amputee model with both control strategies to a simulated trip in the form of a $15 \text{ N} \cdot \text{s}$ impulse applied at 5% of the undisturbed swing duration.

Figure 5.2A shows the toe trajectory of the prosthesis using neuromuscular control both in the undisturbed and disturbed cases. While

Figure 5.1: Simulated Control performance of prosthesis on rough terrain. The distances walked over terrains with different ground roughness are compared between the amputee model using a powered knee-ankle prosthesis with impedance control (green) and hybrid neuromuscular control (blue) as well as with the unimpaired human model (red). Shown are the median and range (25th and 75th percentiles) of the covered distances for 50 terrains sampled at each roughness level.



the impulse causes a large deviation from the nominal trajectory in early swing, the controller quickly recovers. From mid-swing onward, the foot follows a qualitatively similar path, maintains adequate ground clearance, and successfully reaches a similar foot placement as in the undisturbed case. In contrast, with impedance control the prosthesis does not respond adequately when subjected to the disturbance (fig. 5.2B). This is illustrated by the prosthesis behavior in mid swing, during which it does not react appropriately to maintain ground clearance of the toe. Rather, the joint-based impedance functions drive the knee into extension prematurely, and the prosthetic foot scuffs the ground resulting in a trip and subsequent fall.

5.3 Discussion

Our simulation results suggest that the hybrid neuromuscular control policy may be able to improve amputee gait stability over existing impedance control methods. An amputee model walking with a powered prosthesis showed substantial improvements in balance recovery on rough ground and after swing leg trips when using the hybrid neuromuscular control policy as opposed to impedance control. One possible reason for the improvement is that the proposed controller considers global leg information such as the target leg angle (eqs. (4.26) to (4.28)), and it is well known that without placing the feet into proper target points on the ground, legged systems fail to balance [Townsend, 1985, Raibert, 1986, Kajita et al., 2001, Seyfarth et al., 2002, Pratt et al., 2006, Wu and Geyer, 2013]. A second reason

Figure 5.2: Tripping response of the amputee model with neuromuscular (A) and impedance control (B) of the prosthesis. Shown are the prosthetic toe trajectories during undisturbed gait (dashed line) and when disturbed by a $15 \text{ N} \cdot \text{s}$ impulse (solid line). The neuromuscular controller effectively responds to the disturbance and maintains a qualitatively similar toe trajectory. The impedance controller leads to foot scuffing and an eventual fall.

could be that the design of the swing leg control policy explicitly accounts for large disturbances to the lower limb dynamics in order to achieve desired leg placements [Desai and Geyer, 2012]. Finally, the implemented impedance control strategy relies on reliable estimation of the discrete phase of gait during stance so that it can apply the appropriate impedance control parameters. In the presence of disturbances such as the ground height disturbances we studied here, this phase estimate may be incorrect, thus causing the impedance control to apply inappropriate torques.

These results capture only a small portion of the balance disturbances that humans typically encounter [Robinovitch et al., 2013]. Other disturbances may evoke amputee responses that the simulation model does not capture; especially since it is driven solely by a reflexive walking controller that ignores conscious interventions. Therefore, in future chapters of this thesis, we build towards and present results wherein we implement prosthesis controllers on real hardware being used by actual humans in order to more decisively compare control strategies.

6

Preference Based Optimization

Material in this section based on Thatte et al. [2017]¹ and Thatte et al. [2018]²

In chapter 4 we optimized the neuromuscular and impedance control strategies in simulation using a sampling-based optimization method called CMA-ES [Hansen, 2006]. This method targeted specific cost functions. However, as discussed in section 2.4, optimizing a single objective may ignore other aspects of gait that are important. Therefore in this thesis, we instead allow users to select parameters for the prosthesis by providing qualitative feedback in the form of preferences between parameter vectors. In this chapter, we discuss two approaches to optimizing parameters with preferences. The first approach, outlined in sections 6.1 to 6.4, uses Bayesian optimization. This approach, however, was unable to scale to the dimensionality needed for application to prosthesis control. Therefore, in sections 6.5 to 6.8 we outline a second method that poses parameter selection as a dueling bandits problem [Yue et al., 2012].

6.1 Bayesian Approach Introduction

As discussed in section 2.4 previous work has explored learning from qualitative feedback such as preferences in order to circumvent defining objective functions. Also, Bayesian optimization has been proposed to reduce the number of experiments required to solve optimize problems. In this first half of this chapter, we present a new optimization algorithm, Predictive Entropy Search with Preferences (PES-P), that combines these two ideas. We adapt an acquisition function previously proposed for interval scale feedback to the preference feedback case. This acquisition function seeks a pair of parameters for which a preference will maximally reduce the entropy of the distribution of objective function optima. To test the algorithm, we compare in simulation the performance of the

¹ Nitish Thatte, Helei Duan, and Hartmut Geyer. A sample-efficient black-box optimizer to train policies for human-in-the-loop systems with user preferences. *IEEE Robotics and Automation Letters*, 2017

² Nitish Thatte, Helei Duan, and Hartmut Geyer. A method for online optimization of lower limb assistive devices with high dimensional parameter spaces. In *Robotics and Automation (ICRA), 2018 IEEE International Conference on*. IEEE, 2018

proposed optimization method against the expected improvement method (EI) and uniform random sampling via Latin hypercubes (LH) for two classes of examples: optimizing randomly generated objective functions and tuning the control parameters of simulated dynamical systems.

6.1.1 Learning from Preferences

To learn latent objective functions from preferences, we rely on the method developed by Chu and Ghahramani [Chu and Ghahramani, 2005], briefly reviewed here. The method considers a training dataset D_n of n preferences between pairs of points, $\{x_1^a \succ x_1^b, \dots, x_k^a \succ x_k^b, \dots, x_n^a \succ x_n^b\}$. These points can, for instance, represent control policy parameters. From the dataset, the method finds a posterior distribution of latent objective functions f ,

$$P(f|D_n) = \frac{P(D_n|f) P(f)}{P(D_n)} \quad (6.1)$$

where $f = [f(x_1^a), f(x_1^b), \dots, f(x_n^a), f(x_n^b)]^T$. First, the method assumes that the prior distribution of objective functions is a zero-mean Gaussian process (GP), $P(f) = \mathcal{N}(0, \Sigma)$. An appropriate kernel, $\Sigma_{i,j} = k((x_i, x_j))$, describes the elements of the covariance matrix Σ . (See [Williams and Rasmussen, 2006] for a full description of GPs.) Second, $P(D_n|f)$ is the overall likelihood of preferences in the dataset given specific reward function values and is modeled as the product of the likelihood of each independent preference in the dataset,

$$P(D_n|f) = \prod_{k=1}^n P(x_k^a \succ x_k^b | f(x_k^a), f(x_k^b)) = \prod_{k=1}^n \Phi(q_k), \quad (6.2)$$

where $P(x_k^a \succ x_k^b | f(x_k^a), f(x_k^b))$ is the probability of a preference if Gaussian noise with variance σ^2 corrupts the function values, $\Phi(\cdot)$ is the cumulative distribution function of a normal distribution, and $q_k = \frac{f(x_k^a) - f(x_k^b)}{\sqrt{2}\sigma}$. In essence, the likelihood model increases the certainty of a preference between x_k^a and x_k^b as the difference between $f(x_k^a)$ and $f(x_k^b)$ widens.

To obtain the posterior distribution $P(f|D_n)$ the method approximates eq. (6.1) with a Gaussian distribution. As a result, the predictive distribution (subscript p) of the objective function at test points, f_t , is also Gaussian, $P(f_t|D_n) = \mathcal{N}(\mu_p, \Sigma_p)$. Finally, the predictive

distribution of a preference between two points x^a and x^b is

$$P(x^a \succ x^b | D_n) = \int P(x^a \succ x^b | f_t, D_n) P(f_t | D_n) df_t \quad (6.3)$$

$$= \Phi\left(\frac{\mu^a - \mu^b}{\sigma_p}\right), \quad (6.4)$$

$$\sigma_p^2 = 2\sigma^2 + \Sigma_p^{aa} + \Sigma_p^{bb} - \Sigma_p^{ab} - \Sigma_p^{ba}. \quad (6.5)$$

Figure 6.1a provides an example of how the method estimates a ground-truth objective function shown in purple. The blue line and shaded area show the mean and standard deviation of the posterior distribution of objective functions, $P(f_t | D_n)$, after two preference queries between pairs of parameters (orange, higher is preferred over lower value). The queries have the effect of lifting the estimated objective function close to preferred points and pushing it down close to unpreferred points, approximating the true objective function over time.

6.1.2 Active Learning for Optimization

Learning from preferences describes how to find a distribution of objective functions given a dataset of comparisons. The question now becomes how to efficiently solicit preferences from the user. As our main goal is to find the optimal parameters x^* , we should forgo modeling the objective function accurately in all parameter regions and instead focus on regions where the objective might be high. Bayesian optimization addresses this problem with an acquisition function that helps to efficiently sample training data.

One such acquisition function is the expected improvement, which has been used both in the context of preference feedback [Brochu et al., 2008] and interval scale feedback [Jones et al., 1998],

$$EI(x) = (\mu^* - \mu(x))\Phi(d) + s(x)\phi(d), \quad (6.6)$$

where $d = (\mu^* - \mu(x))/s(x)$, μ^* is the mean of the current estimate of the optimum, and $\mu(x)$ and $s(x)$ are the mean and standard deviation of the objective of a new point x , respectively. As an alternative, for interval scale feedback, [Hennig and Schuler, 2012] and [Hernández-Lobato et al., 2014] proposed acquisition functions that seek to reduce the uncertainty in the distribution of objective function optima, measured in terms of the differential entropy. For example, the Predictive Entropy Search acquisition function [Hernández-Lobato et al., 2014] seeks a point x that is expected to reduce the entropy of the distribution of optima x^* after observing its value y ,

$$\alpha_n(x) = H[P(x^* | D_n)] - E_{P(y|x, D_n)} [H[P(x^* | y, x, D_n)]], \quad (6.7)$$

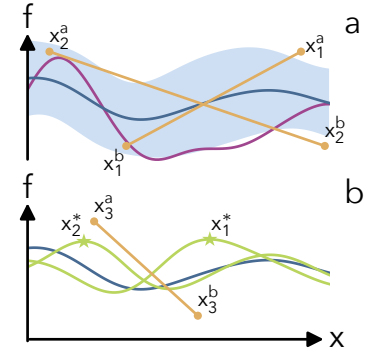


Figure 6.1: Learning from preferences. (a) Mean and standard deviation of $P(f_t | D_n)$ (blue) after two preferences queries (orange) from the true objective function (purple). (b) Mean of $P(f_t | D_n)$ (blue) and means of $P(f_t | D_n, x_m^*)$ (green) for two samples of x_m^* . PES-P queries a new comparison (orange) for which the preference is currently uncertain, but on average is certain after conditioning on all x_m^* .

where $H[P(x)] = - \int P(x) \log P(x) dx$ is the differential entropy. The authors of these methods have shown they can outperform EI.

6.2 Bayesian Approach Methods

Our goal is to simultaneously address both the difficulty of defining objective functions when an expert cannot demonstrate the desired robot behavior and the expense of running experiments on hardware. To this end, we adapt the Predictive Entropy Search acquisition function (eq. (6.7)) to the preference learning case.

6.2.1 Acquisition Function

To obtain the optimal parameters x^* with the smallest number of preference queries, we solicit preferences that maximize the expected information gain about the distribution of objective function optima $P(x^*|D_n)$. Adapting eq. (6.7) to preference feedback yields

$$\alpha_n(x^a, x^b) = H[P(x^*|D_n)] - E_{P(y|x^a, x^b, D_n)} [H[P(x^*|y, x^a, x^b, D_n)]], \quad (6.8)$$

where y is a binary random variable that represents the preference between x^a and x^b . The first term in this function is the current entropy of objective function optima and the second term is the entropy of optima after observing the preference y . As we have not yet observed the preference, we take the second term in expectation over the two possible preference outcomes.

As discussed in [Hernández-Lobato et al., 2014], this acquisition function is intractable to compute. However, following the approach used for the original PES algorithm, we can rewrite eq. (6.8) in terms of the entropies of the predictive distribution of the preference between x^a and x^b ,

$$\alpha_n(x^a, x^b) = H[P(y|x^a, x^b, D_n)] - E_{P(x^*|D_n)} [H[P(y|x^*, x^a, x^b, D_n)]] \quad (6.9)$$

$$\approx H[P(y|x^a, x^b, D_n)] - \frac{1}{M} \sum_{x_m^* \sim P(x_m^*|D_n)}^M H[P(y|x_m^*, x^a, x^b, D_n)]. \quad (6.10)$$

This reformulation significantly improves computability. First, the new acquisition function uses the entropies of probabilities of preferences, given by eq. (6.4). Second, we now take the expectation over $P(x^*|D_n)$, which we can perform by sampling M functions from $P(f_t|D_n)$ and optimizing each one to get M samples of x^* (see Appendix for details). Finally, the second term no longer requires conditioning the GP on every pair of x^a and x^b considered during

optimization of the acquisition function. Instead, we only have to condition the Gaussian process M times on (x_m^*, D_n) .

For the experiments in section 6.3 we choose $M = 12$, which allows us to construct and optimize $\alpha_n(x^a, x^b)$ in about five seconds. Although 12 samples of x^* is not enough to compute an accurate expectation over $P(x^*|D_n)$, interpreting the algorithm as an example of active learning by disagreement may explain why it still works well. As shown in fig. 6.1b, optimizing the acquisition function chooses a pair x^a and x^b for which the preference is currently uncertain, but certain on average after conditioning on all x_m^* . The sampled x_m^* do not necessarily agree on which point is preferred; hence, after observing the preference, the algorithm can rule out x_m^* that made the model certain but wrong about the preference. This intuition is similar to that provided by [Houlsby et al., 2012] for Bayesian active learning by disagreement for GP classifiers.

6.2.2 Conditioning the Gaussian Process on x^*

The second term on the right side of eq. (6.10) requires us to compute the distribution of the preference given the location of the optimum,

$$P(y|x_m^*, x^a, x^b, D_n) = \int P(x^a \succ x^b | f_t, x_m^*, D_n) P(f_t|x_m^*, D_n) df_t. \quad (6.11)$$

It is not directly feasible to condition the predictive distribution on x^* , so instead we turn to approximating this condition with three constraints (see appendix for details):

C1: First we impose that x^* is a local maximum by ensuring that the gradient of $f(x^*)$ is zero and its Hessian is negative definite. We further simplify the Hessian constraint to only require that the Hessian's off-diagonal elements are zero and its diagonal elements are less than zero. We implement the gradient and off-diagonal constraints by conditioning the prior, $P(f)$, on derivative observations as outlined in [Solak et al., 2003]. To constrain the diagonal elements of the Hessian, we amend the likelihood term in eq. (6.1) by adding terms that penalize Hessians with positive diagonal elements.

C2: Second, we try to ensure that x^* is also a global maximum by enforcing that $f(x^*)$ is greater than the function values of all training points sampled so far. We impose this constraint by adding more preference relations into the likelihood term in eq. (6.1) between x^* and all training points.

C3: Finally, to further ensure that $f(x^*)$ is a global maximum, we require that it is also larger than the function values of the two new test points, $f(x^a)$ and $f(x^b)$. Whereas C2 ensures $f(x^*)$ exceeds function values in areas explored so far, C3 ensures that $f(x^*)$ also

Algorithm 1: Predictive Entropy Search with Preferences

```

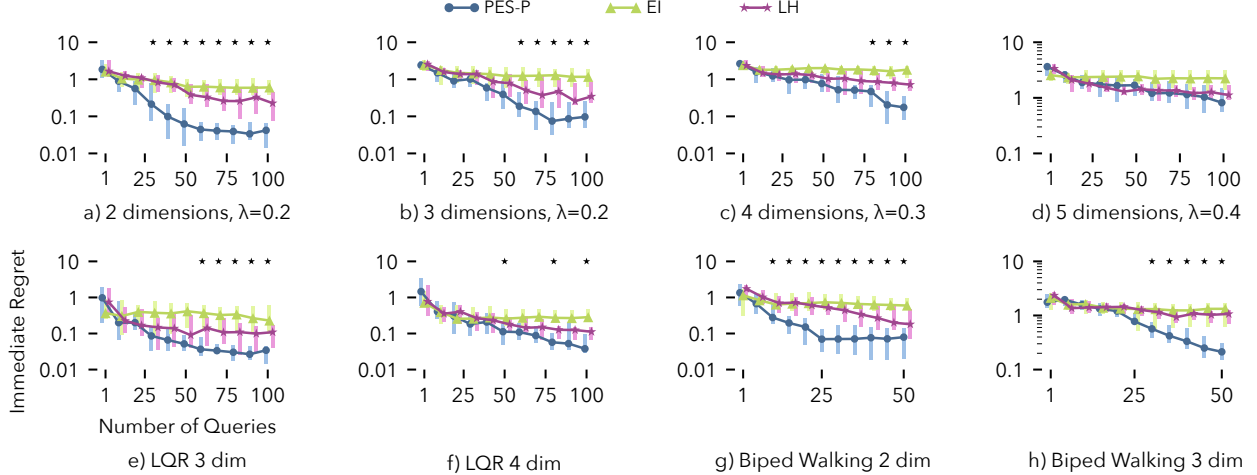
1: procedure PES-P
2:    $D_n = \emptyset$ 
3:   for  $n \leftarrow 0$  to  $N - 1$  do                                 $\triangleright N$  iterations
4:      $F \leftarrow \{f_m \sim P(f_t|D_n) | m \in [1, M]\}$ 
5:      $X^* \leftarrow \{\arg \max_x (f_m) | f_m \in F\}$ 
6:      $(x_{n+1}^a, x_{n+1}^b) \leftarrow \arg \max_{(x^a, x^b)} ff_n(x^a, x^b; X^*)$ 
7:      $y_{n+1} \leftarrow \text{QUERYUSERPREF}(x_{n+1}^a, x_{n+1}^b)$ 
8:      $D_{n+1} \leftarrow D_n \cup (x_{n+1}^a, x_{n+1}^b, y_{n+1})$ 
9:   end for
10:  return  $x^* \leftarrow \arg \max_x \text{mode}(P(f_t(x)|D_N))$ 
11: end procedure

12: function  $\alpha_n(x^a, x^b; X^*)$                        $\triangleright$  acquisition function
13:    $h \leftarrow \left\{ H \left[ P(y|x^a, x^b, D_n, C1, C2, C3) \right] | x_m^* \in X^* \right\}$ 
14:   return  $H \left[ P(y|x^a, x^b, D_n) \right] - \text{mean}(h)$ 
15: end function
```

exceeds function values in unexplored regions. We approximate this constraint analytically by conditioning on the single constraint $f(x^*) > (f(x^a) + f(x^b))/2$ using the method detailed in [Xu and Li, 2010].

6.2.3 Algorithm Summary

With constraints C1 to C3, at each iteration we can efficiently compute the acquisition function, eq. (6.10). We summarize the resulting Predictive Entropy Search with Preferences (PES-P) algorithm as follows (algorithm 1): At each iteration n , first, the algorithm samples M objective functions from the current distribution, $P(f_t|D_n)$, and optimizes each one to generate M samples of x^* (lines 4 and 5). Next, using the set of sampled optimums X^* , we maximize the acquisition function to obtain the next two points to present to the user x_{n+1}^a and x_{n+1}^b (lines 6 and 12–15). Note: we can precompute the effect of C1 and C2 before evaluating $ff_n(x^a, x^b)$ as these two constraints do not depend on x_{n+1}^a and x_{n+1}^b . On the other hand, C3 depends directly on x_{n+1}^a and x_{n+1}^b and therefore is computed within the acquisition function for every pair of points considered during the optimization of $ff_n(x^a, x^b)$. We then query the user to obtain their preference y_{n+1} between these two points and add it to the dataset of preferences (lines 7 and 8). Finally, at the end of the N iterations of the algorithm, we return the optimum x^* of the most likely function, $\text{mode}(P(f_t(x)|D_N))$, which is equal to the posterior mean function



in the Gaussian process case (line 10). While it may be more correct to return mode ($P(x^*|D_N)$), we do not do this as the PES algorithm seeks to avoid approximating this distribution.

6.3 Bayesian Approach Results

We test the ability of PES-P to solve optimization problems in three simulated cases with increasing realism from the optimization of randomly generated objective functions drawn from a GP, to the tuning of feedback gains of random linear systems and a neuromuscular walking model. In all cases, we compare the performance of the proposed algorithm to the expected improvement criterion (EI) (eq. (6.6)) and random sampling via Latin hypercubes (LH)³ [McKay et al., 2000]. For the three cases, we show results over 20 trials and measure performance in terms of the immediate regret, defined as $IR = |f(\tilde{x}_n^*) - f(x^*)|$, versus the number iterations. Here, $f(\tilde{x}_n^*)$ is the objective value of the current estimate of the optimum at this iteration, $f(x^*)$ is the value of the true optimum, and an iteration consists of a single preference query between two points. Additionally, we also check the statistical significance of the reduction in IR obtained by PES-P compared to both EI and LH via two-sided Mann-Whitney U tests ($p < 0.05$).

6.3.1 Optimizing Randomly Generated Objective Functions

To avoid inducing bias by hand-engineering test functions, we first evaluate the algorithm on random synthetic objective functions. We generate objective functions on the domain $x \in [-1, 1]^D$ by sampling

Figure 6.2: Performance of predictive entropy search with preferences (PES-P), expected improvement (EI), and Latin hypercube random sampling (LH) for optimizing random objective functions sampled from a GP (a-d), and tuning feedback control parameters of random linear systems (e-f) and a biped walking model (g-h). Shown are the median and interquartile range over 20 trials of the immediate regret (IR) against the number of preference queries. Black stars indicate iterations for which PES-P achieves statistically significant stochastic reductions in IR compared to both EI and LH according to two-sided Mann-Whitney U tests ($p < 0.05$).

³ LH sampling divides the parameter space into $(2N)^D$ hypercubes, where D is the dimensionality of the space. $2N$ samples are placed such that each hypercube has at most one sample and there is at most one filled hypercube along any row of hypercubes when viewed along any direction. This method ensures that the samples are roughly uniformly distributed in the entire space. At each iteration we choose two of these samples.

a vector of 500 function values from a GP prior with a quadratic mean, $\mu(x) = -x^T x$, and isometric squared exponential covariance $k(x_i, x_j) = \exp\left(\frac{-1}{2\lambda} x_i^T x_j\right)$. We use a quadratic mean function to bias the function distribution away from those that have their optimum on a boundary of the domain, as these functions are easier to optimize.

We continue to generate the rest of the function as it is optimized by conditioning the GP on the 500 seed values and all function values sampled during the optimization. We assume the mean of the final function distribution is the true objective function. To simulate a more realistic situation, we provide the algorithms with noisy preferences from the sampled function values ($\sigma^2 = 0.1$).

Figures 6.2a-d show the immediate regret for two to five dimensional problems with λ , the length scale of the kernel, scaling from 0.1 to 0.4 as the dimensionality of the problem increases. On two to four dimensional problems, PES-P outperforms EI and LH by achieving statistically significant reductions in IR. However, as the dimensionality increases, it takes more iterations for this advantage to become apparent. In the five dimensional case, there is no significant difference between PES-P and LH, perhaps due to $M = 12$ samples of x_m^* being insufficient and the difficulty of accurately sampling x_m^* in higher dimensions.

6.3.2 Tuning Controllers for Random Linear Systems

Next, we test the ability of PES-P to optimize simple control systems by optimizing the feedback gains K for D -dimensional single-input linear systems $\dot{\xi} = A\xi + Bu$ with feedback $u = K\xi$. We sample the elements of the A matrix from the standard normal distribution while $B = [0_{1 \times (D-1)}, 1]^T$. We assume a quadratic instantaneous cost resulting in the objective function

$$f(K) = - \int_0^{t_f} \xi_K^T(t)(Q + K^T R K)\xi_K(t)dt, \quad (6.12)$$

where $\xi_K(t)$ is the evolution of the state under the control policy K and a fixed initial condition ξ_0 , $Q = I_{D \times D}$ and $R = 1$. To obtain a finite search domain, we find the stable range of parameters by varying the elements of the true optimal control parameters K^* one at a time while keeping other elements constant. We scale and shift this region to map to the domain $[-1, 1]^D$. Finally, we use the Automatic Relevance Determination Gaussian Kernel and optimize the hyperparameters at each iteration by maximizing the posterior probability of the hyperparameters under a gamma hyperprior [Chu and Ghahramani, 2005, Williams and Rasmussen, 2006]. In order to apply a consistent noisy preference model ($\sigma^2 = 0.1$) across all sampled systems, we transform all objective values by first mapping

them through $-\log(-f(K))$ and then shifting and scaling the values by the mean and range of the values of 10^D randomly sampled controllers.

Figures 6.2e and 6.2f show the resulting optimization performance on three and four dimensional systems. In the 3 dimensional case, PES-P achieves a lower median IR than LH after 30 iterations. This difference becomes significant after 60 iterations. In the 4 dimensional case, PES-P significantly outperforms LH after 50 iterations, but the significance of this improvement is sporadic as the iterations continue. A possible reason for the reduced performance difference between PES-P and LH in the LQR problem as compared to the random objective function problems is the existence of hard-to-optimize flat regions in the LQR objective functions. This suggests that PES-P may be more well suited for problems that have clear optimum.

6.3.3 Tuning Control Parameters of a Walking Model

In the third case, we test the ability of PES-P to optimize the feedback gains for a neuromuscular model of walking [Thatte and Geyer, 2016], a system with a complex non-linear controller addressing the specific application domain of human locomotion. We perform two and three dimensional optimizations, in which we tune the feedback gains for a subset of the model’s muscle actuators. We use the negative cost of transport plus the distance walked over a 20 second time span as the objective function. As in the previous linear systems example, we obtain noisy preferences between parameters and optimize the hyperparameters at every iteration.

Figures 6.2g and 6.2h show the performance of PES-P, EI, and LH. In this example, PES-P achieves a significant reduction in IR in just 10 iterations in the 2-dimensional case and in 25 iterations in the 3 dimensional case. Furthermore, in the 3D case the PES-P’s median solution is approximately 10 times better than those found by EI or LH.

6.4 Bayesian Approach Discussion

We presented a new optimization algorithm (PES-P) that extends Predictive Entropy Search to preference feedback. The algorithm addresses two key problems frequently encountered in system optimization. First, it circumvents the often difficult process of parameterizing and learning an objective function by directly querying users for preferences between pairs of parameters. Second, the algorithm minimizes the required number of experiments by employing Bayesian optimization techniques that ensure the queries maximize

the information gained about the location of the optimum. Moreover, unlike previous approaches for preference learning on robotic systems [Wilson et al., 2012, Jain et al., 2013], PES-P does not require a model of the system.

Our experiments show that the proposed algorithm outperforms baseline algorithms. In most of the experiments, PES-P found optima that achieved higher objective values than those found by the expected improvement method (EI) or by random comparisons via Latin hypercubes (LH) (fig. 6.2). The reason why PES-P outperformed EI is likely due to the former's explicit consideration of how the limited, noisy information obtained from a preference query will affect the knowledge about potential objective function optima. The acquisition function (eq. (6.8)) recognizes that preferences become more uncertain the closer two sample points are to each other. EI, on the other hand, does not reason about noisy preferences and, instead, still assumes it can sample values (eq. (6.6)). Consequently, EI ignores the distance between sample points, which often leads to a greedy strategy that solicits preferences between adjacent points. While this strategy can resemble gradient ascent with convergence to local optima in a noise-free optimization, it often failed in our experiments characterized by noisy observations. Note, however, that such limitations were not observed by Brochu and colleagues [Brochu et al., 2008], who successfully used EI with preferences to optimize parameters for a graphics application, possibly because the associated visual task produced less noisy responses than did our simulations.

However, a major drawback of the proposed PES-P approach is its limited ability to scale to problems of sufficient dimensionality. As shown in fig. 6.2d PES-P provides little benefit over random sampling on 5D problems. In contrast, to optimize the neuromuscular model control proposed in section 4.6 we need to be able to solve problems with dozens of dimensions. Therefore, in the next half of this chapter, we explore an alternative approach, that frames prosthesis optimization as a dueling bandits problem [Yue et al., 2012].

6.5 Bandit Approach Introduction

In the first half of this chapter, we explored the potential of a method that combines Bayesian optimization with learning from preferences. However, the simulation results presented demonstrate the it is unlikely the proposed method can scale to the dimensionality needed for prosthesis optimization. Previously published impedance control strategies for transfemoral prostheses have roughly 20 tunable parameters for a given gait condition, such as walking at a specific speed. Sup et al. [2011] show that these parameters also vary with

alternative conditions such as incline. Therefore, these kinds of parameterized policies could require on the order of 100 parameters to deal with a range of situations. Previous work has attempted to reduce the number of parameters via heuristic rules that tie impedance parameters to other states of the prosthesis such as joint angles [Simon et al., 2014]. However, it is not obvious how to translate these heuristics to other control strategies, such as the neuromuscular control we propose in section 4.6, or phase-based control [Quintero et al., 2016], which follows knee and ankle trajectories parameterized as functions of hip angle and hip angle integral.

To deal with high-dimensional parameter selection for prostheses, many have turned to offline optimization of control parameters. Markowitz et al. [2011] use data from a height-and weight-matched intact subject to obtain speed-adaptive neuromuscular control parameters for a transtibial amputee’s prosthesis and Aghasadeghi et al. [2013] use an invariant gait representation to model an amputee’s gait and find the appropriate impedance control parameters. In these approaches however, it is unclear how well the resultant parameters suit the subject when executed on actual hardware.

In this paper, we tackle these issues by framing prosthesis optimization as a dueling bandits problem [Yue et al., 2012]. The resulting approach utilizes the subject’s preferences to include subjective user feedback in the tuning process. The method deals with high dimensional optimization problems by incorporating domain knowledge in the form of an offline optimization step. We show that this method produces a library of parameters from which different users prefer different options and for which preferred controllers tend to follow human gait trends. Moreover, we explore further utilizing the offline optimization to help the controllers generalize to speeds that were not included during the online optimization process.

6.6 Bandit Approach Methods

In this study, we use the transfemoral prosthesis presented in chapter 3 and the prosthesis control that uses neuromuscular reflexes during stance and minimum jerk swing trajectories during swing described in section 4.6.

6.6.1 Optimization method

To optimize the control parameters of this neuromuscular transfemoral prosthesis control for specific users, we frame the task as a K -armed dueling bandits problem [Yue et al., 2012]. In this formalism, at each iteration $t \in [1, \dots, T]$ of the optimization, an algo-

rithm chooses two options, referred to as bandits, out of the set of K possibilities, so as to minimize the total cumulated regret over the iterations. The cumulated regret is defined as

$$R(T) = \zeta^* T - \frac{1}{2} \sum_{t=1}^T E[\zeta_{1t} + \zeta_{2t}] \quad (6.13)$$

where ζ^* , ζ_{1t} , and ζ_{2t} , are the values of the optimal bandit and first and second bandits chosen on iteration t respectively. To minimize $R(T)$, algorithms must effectively trade off exploration of all bandits to gain confidence in their values and exploitation of the best bandit so as to not incur regret.

In a dueling bandits problem, we do not observe numeric rewards directly. Rather, we observe if an oracle prefers the first bandit to the second. Because we never directly observe numeric values, algorithms for this problem use alternative notions of value. In this work, we utilize the Double Thompson sampling method [Wu and Liu, 2016], which achieves state-of-the-art regret on several datasets. This method defines a bandit's value as its Copeland Score: the number of other options that a bandit defeats on average.

Key to employing this method for prosthesis optimization is offline generation of parameter sets for which we are likely to obtain reasonable gaits for different subjects. This task can be viewed as sampling from the set of parameters that produce gait patterns consistent with human locomotion. In this work, we explore generating this set of controllers using a recently published gait data set that includes kinematics and kinetics for individual subjects walking at three different speeds, 0.8, 1.2, and 1.6 m/s [Moore et al., 2015]. For each subject in this dataset, we use the Covariance Matrix Adaptation Strategy [Hansen, 2006] to find neuromuscular model parameters Γ that reproduce the subject's body-weight-normalized knee and ankle joint torques $\tau_h = [\tau_h^k, \tau_h^a]^T$ given the subject's hip, knee, and ankle angle trajectories $\theta_h = [\theta_h^h, \theta_h^k, \theta_h^a]^T$. Specifically, we solve

$$\Gamma = \operatorname{argmin}_{\Gamma} (\tau_h - \tau_{nm})^T (\tau_h - \tau_{nm}) + \alpha \xi_{nm}^T \xi_{nm} \quad (6.14)$$

where $(\tau_{nm}, \xi_{nm}) = \text{neuro}_{\Gamma}(\theta_h)$ are the torques and muscle activations generated by the neuromuscular model given the human joint angle trajectories and model parameters. $\alpha = 0.01$ is a small constant we use to help regularize the solutions.

Table 6.1 shows the parameters we optimize during this process. For each parameter in the Speed-Independent category, we look for a single value to use across all speeds. For parameters in the Speed-Dependent category we search for three different values, one for each gait speed in the dataset (0.8, 1.2, and 1.6 m/s). The parameters we choose to optimize include the isometric force and feedback gains for

each muscle, which are closely related to the effective stiffness of the joint [Geyer et al., 2003], muscle prestimulations, which are related to the stride energy [Geyer et al., 2003], and the muscle reference angles, to help deal with the kinematic variability between subjects [Geyer and Herr, 2010].

From the dataset provided by Moore et al. [2015], which contains samples for twelve subjects, we were able to extract nine parameter sets. (One subject’s torque data is corrupted and two subjects’ data resulted in an overly flexed knee when used on the prosthesis.) Figure 6.3 shows an example of two subjects’ torque patterns shown in red. We see that there are significant differences between the two subjects in terms of both timing and magnitude of torque. In green, we see that after optimizing the neuromuscular model for each subject, it is able to capture both gait patterns.

We can quantify the quality of the model fit to the data by computing the root mean squared (RMS) error between the model’s predicted torques and the actual torques. Over the nine parameter sets we achieve a median RMS knee torque error of 35% of the RMS human knee torque, and a median RMS ankle torque error of 15% of the RMS human ankle torque. Much of the error in the knee torque prediction occurs right after heel strike, where the model typically predicts near-zero torque. In future work we plan to adapt the model to produce more knee flexion torque at heel strike, which should significantly reduce the model error.

To compensate for kinematic differences between the prosthesis and the training data, before sending prosthesis joint angles to the neuromuscular control, we add constant bias angles to the joint encoder readings so that at joint j ,

$$\theta_{\text{model}}^j = \theta_{\text{encoder}}^j + \theta_0^j. \quad (6.15)$$

We hand-tune these bias parameters for each bandit and subject to ensure the bandits work as well as possible.

6.6.2 Experiment Procedure

In our experiment, we test the ability of our offline optimization approach to generate controllers that are suited to different subjects and to produce kinematics and kinetics similar to those of intact subjects. We further test the effectiveness of using offline optimizations to help improve the ability of the control to generalize to speeds different than those experienced during the online optimization.

After providing informed consent to a protocol approved by the Carnegie Mellon University Internal Review Board, five non-amputee subjects (four male, one female, average mass = 68.8 kg std 11.17 kg)

	Speed-Independent	Speed-Dependent
$F_{\text{max}}^{\text{ham}}$	ham ϕ_0^{hip}	$F+G_{\text{ham}}$
$F_{\text{vas}}^{\text{max}}$	ham ϕ_0^{knee}	$F+G_{\text{vas}}$
$F_{\text{bfsh}}^{\text{max}}$	vas ϕ_0	$F+G_{\text{gas}}$
$F_{\text{gas}}^{\text{max}}$	bfsh ϕ_0	$F+G_{\text{sol}}$
$F_{\text{sol}}^{\text{max}}$	gas ϕ_0^{knee}	$F-G_{\text{sol}}$
$F_{\text{ta}}^{\text{max}}$	gas ϕ_0^{ankle}	$L+G_{\text{bfsh}}$
$\text{off}_{\text{bfsh}}^{\text{ta}}$	sol ϕ_0	$L-G_{\text{bfsh}}$
$\text{off}_{\text{vas}}^{\text{bfsh}}$	ta ϕ_0	$L+G_{\text{ta}}$
$\text{off}_{\text{ta}}^{\text{ta}}$	S_0^{vas}	
	S_0^{ham}	

Table 6.1: Optimized parameters, Γ . Speed-independent parameters use a single value for all speeds, while speed dependent parameters have distinct values for 0.8, 1.2, and 1.6 m/s gaits. Consequently, in total we optimize 43 parameters. F_{max} refers to a muscle’s maximum isometric force, ϕ_0 is a parameter used for muscle moment arm calculations, and S_0 is a muscle’s pre-stimulation.

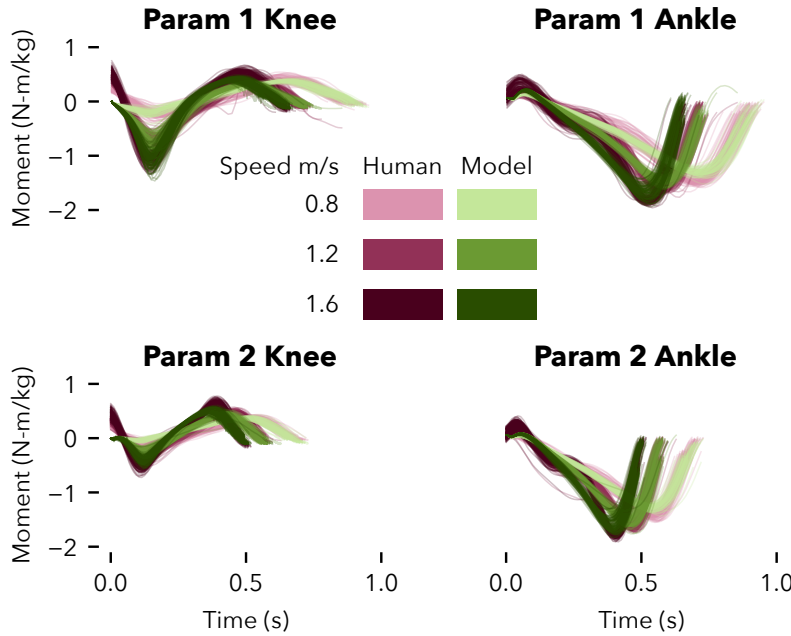


Figure 6.3: Results of the offline optimization that fits the neuromuscular model to intact-subject gait data. Shown are the knee and ankle torques for two different subjects. These plots show there can be significant inter-subject gait variability.

donned the prosthesis via the able-bodied adaptor shown in fig. 3.12. On the contralateral leg, subjects wore a lift shoe, the height of which we adjusted to ensure subjects' hips were even when standing.

Subjects participated in a three day study. On the first day, subjects acquainted themselves with the prosthesis for roughly 2 hours. By the end of this period, all subjects were able to walk (while holding hand rails) consistently without tripping on a set of hand-tuned parameters at a speed of up to 1.2 m/s. On the second day, the first 15 minutes consisted of hand-tuning the bias angles for each parameter set (eq. (6.15)) to allow the subject to achieve adequate ankle and knee flexion for as many parameters as possible. Then, we performed the dueling bandits optimization for 50 iterations, which required approximately thirty minutes of walking at 0.8 m/s. Each iteration consisted of roughly ten seconds of walking on each parameter, after which the subject indicated their preference. If subjects were unsure of their decision they could walk with both parameter sets multiple times. If their uncertainty persisted, the experimenter chose the parameter set that produced angles and torques more aligned with human data. If the experimenter also had no preference, a random number generator selected the winner. We chose to perform fifty iterations, as pilot testing suggested this was sufficient for the algorithm to begin comparing the optimal parameter set to itself, indicating a high level of confidence in the optimum.

On the third day, subjects walked with their preferred parameters at 0.8, 1.0, 1.2, 1.4, and 1.6 m/s. For each speed, we tested both the appropriate speed-dependent parameters and those designed for 0.8 m/s. To obtain parameters for 1.0 and 1.4 m/s we performed linear interpolation between the adjacent parameters. Finally, we recorded the subject's gait at 0.8 m/s for all non-preferred parameter sets and the hand-tuned parameters used on the first day.

6.7 Bandit Approach Results

6.7.1 Copeland Scores

The five subjects in the study preferred four different parameter sets out of the nine parameter sets they could choose from, thereby demonstrating that the offline optimization approach can generate parameters that suit different users. Figure 6.4 shows the total Copeland score achieved by each parameter set across all five subjects. From this chart, we can see it is possible, as in the case of parameter set 6, that a controller receives high scores from some users while receiving a score of zero from other users. This illustrates the importance of tailoring prostheses to individual users. Some parameters such as parameters 1, 4, and 8, achieved consistently low scores across all users. It may be possible for us to remove these parameters from future studies. However, more subjects would be needed before making such a determination as parameter set four received a relatively high score from subject five.

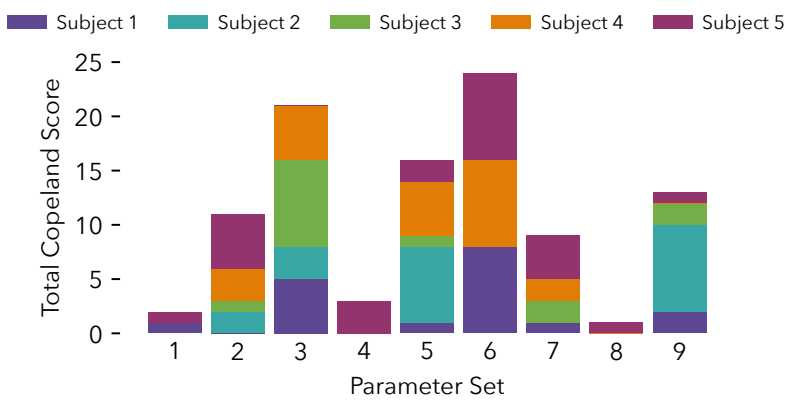


Figure 6.4: Total Copeland score achieved by each parameter set across all five subjects.

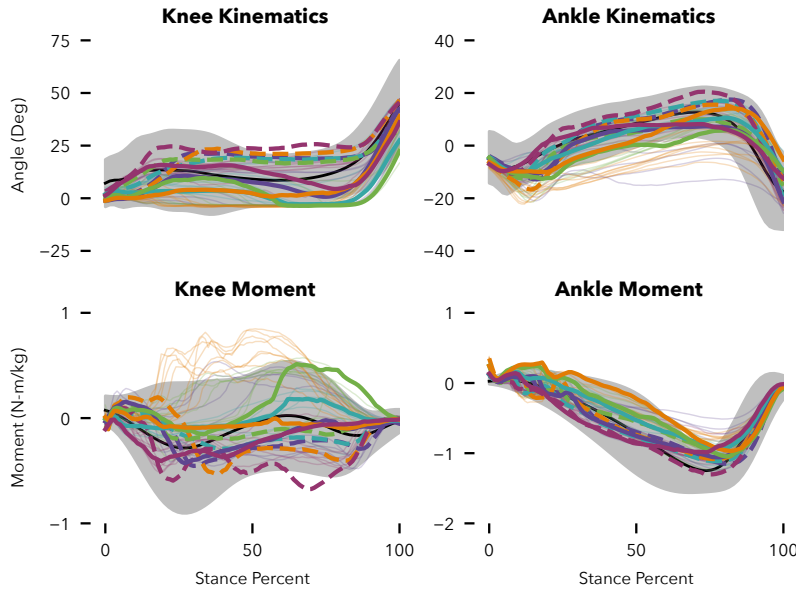


Figure 6.5: Median angles and moments at 0.8 m/s for all parameter sets for all subjects. Thicker weight solid lines indicate each subject’s gait with their preferred parameters. Dashed lines indicate gait with hand-tuned parameters. The grey shaded regions show the mean and three sigma intact subject gait data (from the extra slow walking data in [Bovi et al., 2011]).

6.7.2 Kinematics and Kinetics at 0.8 m/s

Figure 6.5 shows the ankle and knee kinematics achieved by all subjects on all parameters at 0.8 m/s . The thicker solid lines indicate the gait data produced by subjects’ preferred parameters and the dashed lines indicate the gait data produced by the hand-tuned parameters. We see that subject gait with both their preferred parameters and hand-tuned parameters follow similar trends to intact gait data [Bovi et al., 2011], whose mean and three sigma variance is shown as the blue shaded region. However, all subjects preferred the optimized parameters to the hand-tuned set.

Just as in the intact data, there is significant variation in subjects’ preferred gait characteristics, which reinforces the idea that targeting a specific kinematic or kinetic pattern may not be ideal for all users. This seems to be especially true of the knee joint moment, where there are significant differences in the amount of knee extension torque in early stance and flexion torque in late stance among users.

6.7.3 Control Performance at Higher Gait Speeds

Figure 6.6 shows the average net ankle work⁴ produced by the control strategy at speeds ranging from 0.8 to 1.6 m/s . Data from subjects 1, 2, and 3, who chose parameter sets 5, 9, and 3 respectively, show a clear downwards trend in ankle work as speed increases when using a constant set of gains. On the other hand, with the adaptive gains,

⁴ The area within the torque versus angle plot of the ankle over a stride.

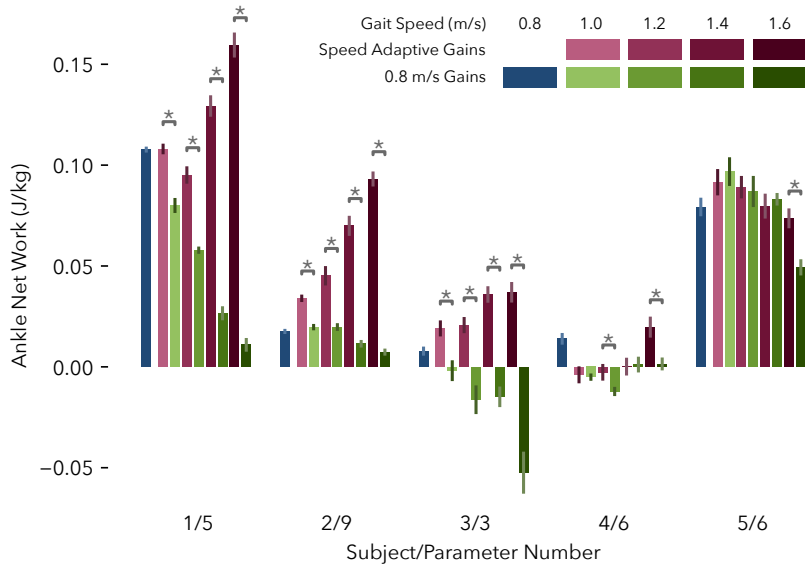


Figure 6.6: Average net ankle work for each subject at each speed. Purple bars indicate trials where speed-adaptive gains were used whereas green bars indicate trials performed with the gains for 0.8 m/s. Stars indicate statistically significant differences between the work produced by the speed adaptive gains and that produced by the 0.8 m/s gains ($p < 0.05$).

as speed increases ankle work increases, mimicking the behavior of the biological ankle [Herr and Grabowski, 2011]. All three of these subjects preferred the behavior of the adapted parameters to the parameters for 0.8 m/s when walking at 1.4 and 1.6 m/s.

Subjects 4 and 5 both chose parameter set six and show no clear trend in ankle work as speed increases. For this parameter set, the speed adapted gains only increased ankle work significantly over baseline at 1.6 m/s for both subjects. Additionally, these two subjects indicated no trend in preference between the adapted and unadapted parameters at the higher speeds. These two subjects produced different amounts of net work despite using the same parameter set. This is likely due to kinematic differences between the subjects as well as differently tuned bias settings for the ankle joint.

From this result we can conclude that the offline optimization approach can produce improved responses at speeds other than that at which we conduct the online optimization, but that the improvement needs to be confirmed on a per-parameter basis. It is not currently clear why parameter set six does not exhibit increasing ankle work as speed increases as the underpinning human data for this parameter set does indeed exhibit the desired trend. The issue could possibly lie with the structure of the high level control or with local minimums obtained by the CMA-ES method.

6.8 Bandit Approach Discussion

We present a new approach for online optimization of lower limb assistive devices that uses preference feedback to incorporate the user's subjective assessment of device behavior. The method tackles high dimensional tuning problems by incorporating domain knowledge via an offline optimization step that utilizes kinetic and kinematic data from intact subjects to obtain a library of policy parameters. We find that the five subjects who completed our experiment preferred four different parameter sets from this library. The resulting gait patterns resembled intact human gait data and were preferred to hand-tuned parameters, confirming that the method can generate parameters suited for different subjects.

A result of the offline optimization we use is that the method is largely agnostic to the number of tunable parameters. Consequently, we were able to additionally optimize neuromuscular model parameters for different speeds. Our experimental results show that these parameters improved the ankle work characteristics and user preferences as speed increased for three out of four tested parameter sets.

Previous works such as Eilenberg et al. [2010] and Markowitz et al. [2011] have demonstrated control of powered ankle prostheses via neuromuscular models of muscles and reflexes. This paper extends that work, as it presents the first instance of neuromuscular control on a powered knee and ankle prosthesis.

Due to the ability of the method to handle problems of arbitrary dimensionality given sufficient computational resources, it may be used to tune many types of control strategies. For example, one could use the approach to optimize the phase variable control strategy, in which the prosthesis follows predefined knee and ankle trajectories parameterized as functions of hip angle and hip angle integral [Quintero et al., 2016]. In this case, each bandit would provide a different knee and ankle trajectory. Importantly, the ability of this method to optimize various types of controllers may help researchers compare control strategies fairly, as we do in chapter 7.

It is probable that the parameter library we obtained in this work can be further improved. We propose two directions for further investigation: First, it may be possible to improve the library by obtaining a larger set of gait data and then using clustering algorithms to arrive at a reduced set of canonical gaits. Vardaxis et al. [1998] apply a similar idea to EMG data to cluster gaits into five major styles. With a library derived from canonical gaits, we may cover the parameter space more evenly. A second approach is to use biomechanical measurements from the amputee, such as segment lengths and mea-

sured peak joint torques, to obtain probability distributions for the neuromuscular model parameters. We could then compose the parameter library by sampling parameters from the distributions and performing rigid body simulations of the amputee and prosthesis system.

The optimization approach we have presented may have considerable practical value for commercial prostheses as well. Because it uses preference feedback, users of an assistive device can easily provide feedback via smartphones or wearable devices. Moreover, the dueling bandit algorithm is well suited to lifelong learning. Since the algorithm seeks to minimize regret, we can ensure its exploration is only as obtrusive as necessary.

The study we presented has several limitations. First, we only had five subjects complete the study. Ideally, we would have more subjects than the number of parameter sets so we could determine if any parameters are never preferred or if any group is not currently well represented by the current set of parameters. Also, we should confirm that the proposed optimization framework provides suitable control parameters for amputees wearing this prosthesis.

Bayesian Approach Appendix

To obtain X^* (line 5, algorithm 1), we sample M functions from the posterior by approximating $P(f_t|D_n)$ using Bayesian linear regression with Fourier features (as outlined in [Hernández-Lobato et al., 2014]) and sampling M feature weight vectors. As the Fourier features have analytic derivatives, we can optimize each linear function using a second order method with multiple restarts.

We approximate conditioning the predictive distribution on x^* via three constraints:

C1 x^* is a local maximum. $\nabla f|_{x^*} = 0$ and the Hessian of the objective function is negative definite by imposing $\text{diag}(\nabla \nabla f|_{x^*}) < 0$ and $\text{upper}(\nabla \nabla f|_{x^*}) = 0$. We group $\nabla f|_{x^*} = 0$ and $\text{upper}(\nabla \nabla f|_{x^*}) = 0$ into constraint C1.1 and $\text{diag}(\nabla \nabla f|_{x^*}) < 0$ into constraint C1.2.

C2 x^* is preferred to current training points, $f(x^*) > f(x_k^a)$ and $f(x^*) > f(x_k^b)$, $\forall k \in [1, n]$.

C3 x^* is preferred to new training points, $f(x^*) > f(x_{n+1}^a)$ and $f(x^*) > f(x_{n+1}^b)$.

We precompute the effects of constraints C1 and C2 before evaluation of $ff_n(x^a, x^b)$. To impose C1 and C2, we first divide their components into two groups: $c = [\nabla f|_{x^*}^\top, \text{upper}(\nabla \nabla f|_{x^*})^\top]^\top$ and $f' = [f^\top, \text{diag}(\nabla \nabla f|_{x^*})^\top, f(x^*)]^\top$. Note C1.1 $\implies c = 0$. We write

the predictive distribution of the objective function at test points f_t given constraints C1 and C2 as

$$P(f_t|D_n, C1, C2) = \int P(f_t|f', C1.1) P(f'|D_n, C1, C2) df'. \quad (6.16)$$

We use Bayes rule to evaluate the second term in the integral,

$$P(f'|D_n, C1, C2) = \frac{P(D_n, C1.2, C2|f') P(f'|C1.1)}{P(D_n, C1.2, C2|C1.1)}. \quad (6.17)$$

We form the prior term $P(f'|C1.1)$ by conditioning the joint distribution, $P(c, f')$ on C1.1 given by $c = 0$.

$$P(f'|c) = \mathcal{N}(f'|\Sigma_{cf'}^T \Sigma_{cc}^{-1} c, \Sigma_{ff'} - \Sigma_{cf'}^T \Sigma_{cc}^{-1} \Sigma_{cf'}) \quad (6.18)$$

implies $P(f'|c = 0) = \mathcal{N}(f'|0, \Sigma_{ff'}|_c)$.

We implement the likelihood term by adding extra factors to the likelihood in eq. (6.1) that impose soft constraints representing C1.2 and C2. For C1.2 we use the penalty term $P([\nabla \nabla f|_{x^*}]_{dd} < 0 | [\nabla \nabla f|_{x^*}]) = \Phi(-[\nabla \nabla f|_{x^*}]_{dd}/\sigma_h)$ and for C2 we add more preference relations between x^* and all training points.

$$\begin{aligned} P(D_n, C1.2, C2, |f') &= \left[\prod_{k=1}^n P(x_k^a \succ x_k^b | f(x_k^a), f(x_k^b)) P(x^* \succ x_k^a | f(x^*), f(x_k^a)) P(x^* \succ x_k^b | f(x^*), f(x_k^b)) \right] \\ &\times \prod_{d=1}^D P([\nabla \nabla f|_{x^*}]_{dd} < 0 | [\nabla \nabla f|_{x^*}]_{dd}) \\ &= \left[\prod_{k=1}^n \Phi(q_k) \Phi(q_k^{a*}) \Phi(q_k^{b*}) \right] \prod_{d=1}^D \Phi(q_d^h) \end{aligned} \quad (6.19)$$

Where $q_k^{a*} = \frac{f(x^*) - f(x_k^a)}{\sqrt{2}\sigma}$ and $q_k^{b*} = \frac{f(x^*) - f(x_k^b)}{\sqrt{2}\sigma}$ and $q_d^h = \frac{-[\nabla \nabla f|_{x^*}]_{dd}}{\sigma_h}$.

We use Laplace's approximation to approximate $P(f'|D_n, C1, C2)$ as Gaussian,

$$P(f'|D_n, C1, C2) \approx \mathcal{N}\left(f' | f'_{MAP}, \left(\Sigma_{ff'}^{-1} + \Lambda_{f'_{MAP}}\right)^{-1}\right), \quad (6.20)$$

where $f'_{MAP} = \arg \min_{f'} -\log P(f'|D_n, C1, C2)$ and $\Lambda_{f'_{MAP}}$ is the Hessian of $-\log P(D_n, C1.2, C2|f')$ evaluated at f'_{MAP} .

We compute the first term in eq. (6.16), $P(f_t|f', C1.1)$ by conditioning the joint distribution $P(c, f', f_t)$ on f' and $c = 0$,

$$P(f_t|f', c = 0) = \mathcal{N}\left(f_t | \left(\Sigma_{ct}^T B + \Sigma_{ft}^T D\right) f', \Sigma_{tt} - \begin{bmatrix} \Sigma_{ct}^T & \Sigma_{ft}^T \end{bmatrix} \begin{bmatrix} A & B \\ C & D \end{bmatrix} \begin{bmatrix} \Sigma_{ct} \\ \Sigma_{ft} \end{bmatrix}\right), \quad (6.21)$$

where, $\begin{bmatrix} A & B \\ C & D \end{bmatrix} = \begin{bmatrix} \Sigma_{cc} & \Sigma_{cf'} \\ \Sigma_{cf'}^T & \Sigma_{ff'} \end{bmatrix}^{-1}$. We can substitute eq. (6.21)

and eq. (6.20) into eq. (6.16) to yield the predictive distribution subject to constraints C1 and C2.

$$\begin{aligned} P(f_t|D_n, C1, C2) = & \mathcal{N} \left(f_t | (\Sigma_{ct}^T B + \Sigma_{f't}^T D) f'_{MAP}, \Sigma_{tt} - \begin{bmatrix} \Sigma_{ct}^T & \Sigma_{f't}^T \end{bmatrix} \begin{bmatrix} A & B \\ C & D \end{bmatrix} \begin{bmatrix} \Sigma_{ct} \\ \Sigma_{f't} \end{bmatrix} \right. \\ & \left. + (\Sigma_{ct}^T B + \Sigma_{f't}^T D) (\Sigma_{f'|c}^{-1} + \Lambda_{f'_{MAP}})^{-1} (\Sigma_{ct}^T B + \Sigma_{f't}^T D)^T \right). \end{aligned} \quad (6.22)$$

We obtain $P(f_t|D_n, C1, C2, C3)$ by analytically conditioning eq. (6.22) on the single inequality $f(x_m^*) > (f(x^a) + f(x^b))/2$ using the method detailed in [Xu and Li, 2010]. Finally, using eq. (6.11) we can compute the predictive distributions of preferences given the locations of x_m^* .

To optimize $ff_n(x^a, x^b)$ (line 7, algorithm 1) we construct its gradient by evaluating $P(f_t|D_n)$ and $P(f_t|D_n, C1, C2, C3)$ at test points x^a and x^b as well as points offset by $\delta_x = \pm 0.001$ along each dimension. We then optimize $\alpha_n(x^a, x^b)$ via gradient ascent.

7

Experimental Comparison of Neuromuscular and Impedance Controllers

7.1 Introduction

To date, there have been many proposed controllers for prostheses, which we reviewed in section 2.2. However, there has been a dearth of studies directly comparing the merits and detriments of these different strategies.

In this work, we provide one such study by comparing the neuromuscular (NM) and impedance (IMP) control strategies in a similar manner as in chapter 5. We seek to make this comparison as objective as possible. To do this, we minimized the experimenter's influence on controller parameter selection by using the dueling bandits parameter selection method presented in chapter 6. This method comprises of two parts: 1) We first generated parameters for both controllers through offline optimizations that try to match the controller output to able-bodied gait data of different subjects. 2) We used a preference-based optimization that allows users to select their preferred parameter set. Finally, we also replaced the hand tuning of offset angles that we used in chapter 6 (eq. (6.15)) with an iterative learning procedure.

We had also hoped to compare neuromuscular and impedance control to the continuous phase-based control proposed by Quintero et al. [2016]. However, we were unable to achieve a consistent walking pattern with this control strategy. We present our results trying to implement this control strategy later in this thesis in section 9.2.

We are primarily interested in potential robustness improvements provided by neuromuscular prosthesis control, as predicted by the simulation results presented in chapter 5. To examine controller robustness, we tested both controllers with able-bodied subjects walking with their preferred parameters at constant speed and with treadmill velocity disturbances. We then evaluated the user

ratings, number of falls, reasons for falls, and gait variability for each condition.

7.2 Methods

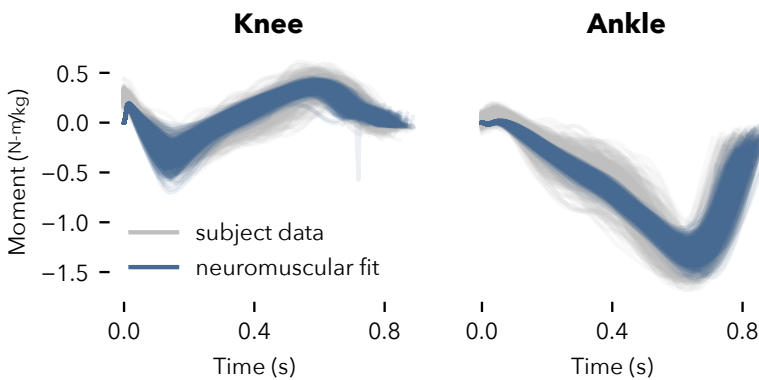
7.2.1 Parameter Generation

To obtain suitable parameters for the neuromuscular and impedance control methods we relied on the dueling bandits optimization approach outlined in section 6.6.1. Whereas in section 6.6.1 we optimized control parameters to match gait data at different speeds to achieve a speed-adaptive control, in this work, we optimized control parameters to match both undisturbed and disturbed gait in order to obtain robust control parameters. We used the dataset provided by Moore et al. [2015], which provides gait data for undisturbed walking and walking with treadmill velocity disturbances.

For the neuromuscular control, we used the black-box CMA-ES optimizer [Hansen, 2006] to obtain parameters that can reproduce the behavior of each subject in the gait dataset. We optimized the parameters listed in table 7.1 so the model’s output torques match those in the gait dataset. Specifically, we minimized the following cost function:

$$\Gamma = \operatorname{argmin}_{\Gamma} (\tau_h - \tau_{nm})^T (\tau_h - \tau_{nm}) + \alpha \xi_{nm}^T \xi_{nm} \quad (7.1)$$

where τ_{nm} and ξ_{nm} are the torques and muscle activations respectively generated by the neuromuscular model given the human joint angle trajectories and model parameters Γ . $\alpha = 0.01$ is a small constant we use to help regularize the solutions and prevent muscle stimulations from saturating. Figure 7.1 shows an example of the fit achieved to one subject’s joint moments.



Optimized Parameters	
F_{\max}^{ham}	$F+G_{\text{ham}}^{\text{ham}}$
F_{\max}^{vas}	$F+G_{\text{vas}}^{\text{vas}}$
F_{\max}^{gas}	$F+G_{\text{gas}}^{\text{gas}}$
F_{\max}^{sol}	$F+G_{\text{sol}}^{\text{sol}}$
F_{\max}^{ta}	$F-G_{\text{sol}}^{\text{ta}}$
off_t^{ta}	$L+G_{\text{ta}}^{\text{ta}}$
$\text{off}_\phi^{\text{vas}}$	$\phi G_{\text{knee}}^{\text{vas}}$
S_0^{vas}	$\epsilon_{\text{SE}}^{\text{ap}}$
S_0^{ham}	$F_{\text{init}}^{\text{ham}}$

Table 7.1: Optimized parameters, Γ . We optimize 18 parameters. F_m^m refers to muscle m ’s maximum isometric force, S_0^m is muscle m ’s pre-stimulation, signal G_n^m is the gain on a feedback signal from muscle n acting on muscle m , $\epsilon_{\text{SE}}^{\text{ap}}$ is the tendon reference strain of the ankle plantarflexors (sol and gas) and $F_{\text{init}}^{\text{ham}}$ is the initial force in the hamstring MTU at heelstrike.

Figure 7.1: Example of fit to subject data achieved by neuromuscular model.

The impedance stance control strategy we implemented, is similar to those reviewed in section 2.2.2. We paired this stance control strategy with the same minimum jerk swing control as we used with neuromuscular control (section 4.6). Figure 7.2 shows the state machine for the implemented impedance stance/minimum-jerk swing control. In each stance phase, we use a linear spring-damper relationship between the output torque of a joint and the joint angle/velocity (eq. (2.4)).

To generate parameters for impedance control, we followed a two step procedure: In the first step, we identified appropriate joint angle thresholds that define the impedance controller's finite state machine transition rules. In the impedance controller, the transition from phase 1 to phase 2 of stance is based on the knee angle crossing a threshold. We specified this threshold such that 95% of steps in a subject's gait data pass from phase 1 to phase 2. As we used gait data with disturbances, this procedure automatically sets the threshold such that it allows for a large degree of gait variation. Next, we identified the ankle angle threshold that defines the transition between stance phases 2 and 3. Again, we set this threshold such that 95% of the steps that made it through the first transition successfully complete the second transition as well. We set the thresholds so that 95% of steps pass through, instead of 100% of steps, to ignore outlier steps.

Once we identified the joint angle thresholds that define state transitions, we next fitted the impedance parameters within each phase. In each phase, the torque output of the impedance control for a particular joint is

$$\tau_{\text{imp}} = -k(\theta - \theta_0) - b\dot{\theta} \quad (7.2)$$

$$= \begin{bmatrix} -\theta & -\dot{\theta} & 1 \end{bmatrix} \begin{bmatrix} k \\ b \\ k\theta_0 \end{bmatrix} \quad (7.3)$$

$$= \vec{\Theta}\vec{k}, \quad (7.4)$$

where $\vec{\Theta}$ is a matrix of the subject's joint angles and velocities and \vec{k} is a vector of the impedance parameters. Therefore, the squared error between the subject's joint torque τ_h and the impedance control model is

$$\epsilon_\tau = (\tau_{\text{imp}} - \tau_h)^T (\tau_{\text{imp}} - \tau_h) \quad (7.5)$$

$$= \vec{k}^T \vec{\Theta}^T \vec{\Theta} \vec{k} - 2\vec{\tau}_h^T \vec{\Theta} \vec{k} + \vec{\tau}_h^T \vec{\tau}_h. \quad (7.6)$$

To calculate the impedance parameters for each phase we minimized the squared error subject to the constraints $k > 0$ and $b > 0$, which ensures that the resulting impedance models are stable. Finally,

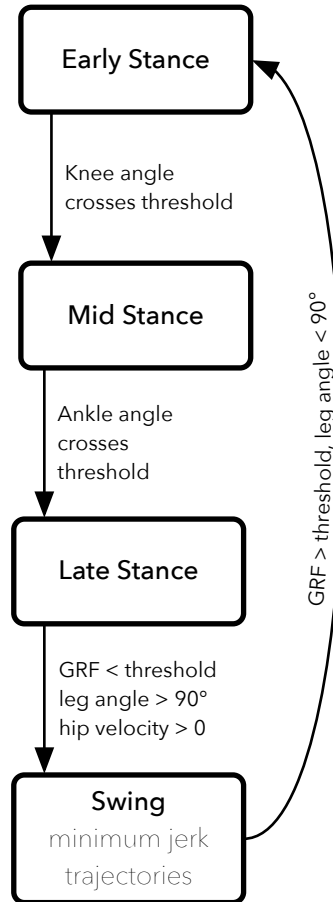


Figure 7.2: Finite state machine used for impedance control scheme. In each state the control employs linear impedance functions that determine the behavior of the ankle and knee joints. At toeoff, the controller generates minimum-jerk trajectories for the knee and ankle to follow during swing.

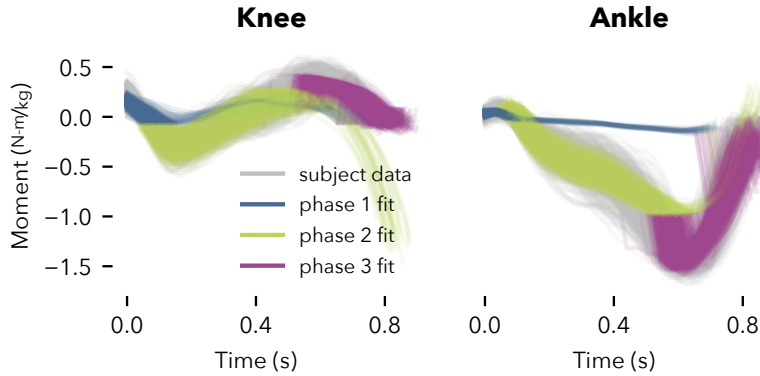


Figure 7.3: Example of fit to subject data achieved by impedance control model to. Note that green trajectories in knee moment plot and blue trajectories in ankle moment plot that do not track subject data are those that did not successfully transition to the next phase.

to obtain model parameters that are robust to outlier steps in the dataset, we utilized the RANSAC procedure, which iteratively solves the above optimization on randomly sampled subsets of the data in order to classify outliers and fit to inliers only [Fischler and Bolles, 1981].

Figure 7.3 shows an example of the impedance control model optimized to match one subject's gait data. In this figure, the color of the lines indicates the phase of gait. We see that the majority of steps fit the subject's joint moments (grey) well. However, there are a few steps for which the color of the line, and thus the phase does, not transition properly. Consequently, the resulting torque diverges from the human data. This is expected as the phase transition angles were selected such that 95% of steps pass through each phase transition.

7.2.2 Iterative Learning

In section 6.6, in order to compensate for kinematic differences between the joint angles in the gait dataset and the joint angles of the prosthesis, we applied hand-tuned offsets to the measured prosthesis joint angles before calculating the neuromuscular model torques (eq. (6.15)). These offsets helped ensure the prosthesis achieved comfortable levels of ankle dorsiflexion, and prevented knee over extension (or flexion) during stance. In this experiment, in order to reduce the potential for bias induced by hand tuning, we take a more systematic, iterative learning approach to tuning these offsets.

During the iterative learning procedure, each subject walked with each parameter set for both the neuromuscular and impedance controllers. The knee and ankle angle trajectories during stance were recorded and after each step, the following update rules were applied to the knee and ankle joint offsets

$$\theta_{\text{knee}}^{\text{offset}} \leftarrow \theta_{\text{knee}}^{\text{offset}} + k_{\text{lrm}} \left(\theta_{\text{knee}}^{\text{ext}} - \theta_{\text{knee}}^{\text{ext,tgt}} \right) \left(\theta_{\text{knee}}^{\text{flex}} < \theta_{\text{knee}}^{\text{flex,max}} \text{ OR } \theta_{\text{knee}}^{\text{ext}} > \theta_{\text{knee}}^{\text{ext,tgt}} \right) \quad (7.7)$$

$$\theta_{\text{ankle}}^{\text{offset}} \leftarrow \theta_{\text{ankle}}^{\text{offset}} + k_{\text{lrm}} \left(\theta_{\text{ankle}}^{\text{flex}} - \theta_{\text{ankle}}^{\text{flex,tgt}} \right), \quad (7.8)$$

where $k_{\text{lrm}} = 0.05$ controls the learning rate, $\theta_{\text{knee}}^{\text{ext}}$ and $\theta_{\text{knee}}^{\text{ext,tgt}} = 0^\circ$ are the measured and target knee extension in mid-stance respectively and $\theta_{\text{ankle}}^{\text{flex}}$ and $\theta_{\text{ankle}}^{\text{flex,tgt}} = 12^\circ$ are the measured and target ankle dorsiflexion in mid-stance respectively. The conditional terms in the knee iterative learning rule prevent the knee offset angle from inducing more knee flexion if the knee flexion in early stance, $\theta_{\text{knee}}^{\text{flex}}$, crosses a threshold $\theta_{\text{knee}}^{\text{flex,max}} = 10^\circ$.

7.2.3 Treadmill Disturbance

In our experiment we probed the robustness of the impedance and neuromuscular prosthesis controllers. To this end, we disturbed gait using treadmill velocity disturbances similar to those in the gait dataset we used to generate parameters [Moore et al., 2015]. During the disturbed walking conditions, the treadmill velocity was generated as follows: First, random accelerations were sampled from a zero-mean Gaussian distribution with variance $35 \text{ m}^2/\text{s}^4$. These accelerations were saturated to the range, $[-15, 15] \text{ m/s}^2$. Next, the acceleration was integrated to obtain a velocity signal, and the long-term drift was removed by a 2nd order high-pass filter with a passband edge frequency of 0.5 hz. Finally, a constant offset of 0.8 m/s was applied to the velocity signal, which was then saturated to the range $[0, 3.6] \text{ m/s}$.

7.2.4 Experimental Protocol

We evaluated the robustness, user ratings, and causes for falls of the neuromuscular and impedance controllers in an experiment with ten able-bodied subjects wearing the prosthesis via an adaptor. All subjects provided informed consent to IRB-approved protocols. Subjects participated in the following six-day procedure:

Day 1: Practice Session Subjects practiced walking on the prosthesis until they could achieve consistent gait without the use of handrails. Subjects who could not achieve hands free walking by the end of the two-hour practice session did not continue with the experiment.

Day 2: Practice Session On the second day subjects continued to practice walking on the prosthesis without the use of hand rails. In

addition, on this day subjects practiced walking with the disturbance described in section 7.2.3. This session lasted for 2 hours.

Day 3: Iterative Learning Subjects walked with each of the nine parameter sets for each controller while the iterative learning procedure (section 7.2.2) tuned the joint angle offsets.

Day 4: Dueling Bandits Optimization We performed the dueling bandits optimization procedure (section 6.6) to find each subject's preferred parameters with both controllers. The order in which we optimized controllers was chosen randomly.

Day 5: Disturbance Experiment - Practice We performed a practice session for the full disturbance experiment. First, subjects walked without the prosthesis at 0.8 m/s for 2 minutes without disturbances and then 2 minutes with the treadmill velocity disturbance enabled. After completing these no-prosthesis trials, subjects donned the prosthesis and tested the neuromuscular and impedance controllers in five rounds of trials that consisted of three trials each. In each trial, subjects walked without disturbances for 1 minute and with disturbances for 1 minute. In each round of trials, the subjects tested their preferred neuromuscular and impedance control parameters along with a set of suboptimal parameters for one controller type. Odd numbered subjects tested a suboptimal neuromuscular parameter set, while even numbered subjects tested a suboptimal impedance parameter set. For the suboptimal parameter set we chose the parameter set that ranked 7th out of 9 in terms of cumulative Copeland score (defined in section 6.6.1) at the end of the dueling bandits tuning procedure.

Day 6: Disturbance Experiment - Data Collection The procedure for this day was identical to that of day 5. During these trials, a Vicon motion capture system captured the motion of the legs. Additionally, subjects wore an IMU that measured the roll and pitch of the torso during walking. During trials, we recorded the number of falls (measured as the number of times subjects needed to use the hand rails or the ceiling-mounted hardness to recover balance) and the user ratings for both the undisturbed and disturbed conditions of each trial.

We evaluated the robustness of the two control strategies primarily by looking at the number of falls experienced by each subject in the no disturbance and disturbance cases. As a baseline, we also compared to the no prosthesis case. As a secondary measures of gait robustness, we also measured the variability of the torso pitch and roll angles. The variability is measured by subtracting the median torso angle trajectory over the strides in a condition from the

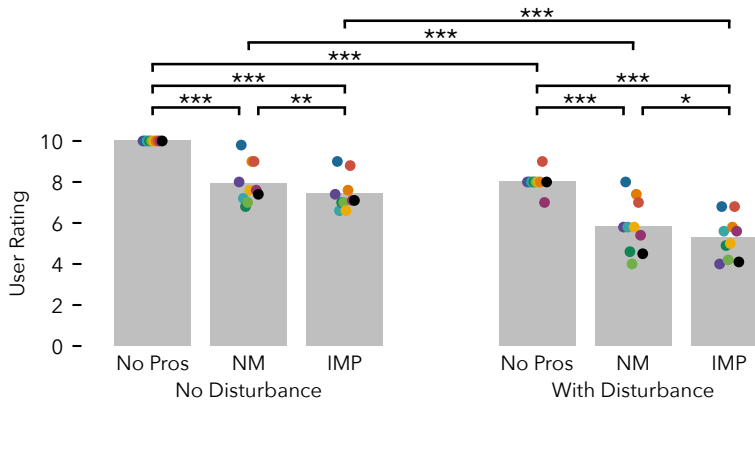


Figure 7.4: Average user ratings across all trials in both the undisturbed and disturbed walking conditions when walking without the prosthesis (No Pros) and with the Neuromuscular (NM) prosthesis control and impedance (IMP) prosthesis control. Grey bars show the mean across subjects. Statistical significance assessed by paired t -tests. *: $p < 0.05$, **: $p < 0.01$, ***: $p < 0.001$.

corresponding torso angle trajectories. Then the interquartile range (IQR) of the median subtracted trajectories is used as the measure of variability.

7.3 Results

First, fig. 7.4 shows the user ratings of the different conditions. We mandated that users rate the No Prosthesis/No Disturbance case 10/10 so that other conditions could be rated relative to this case. We see that in both the no disturbance and disturbance cases, neuromuscular control was rated significantly more preferably than impedance control. Neither control could match the ratings given to the no prosthesis case. Introduction of the disturbance caused a significant drop in user rating for all controllers.

Next, fig. 7.5 shows the number of falls in each condition. Here we see that there was significant differences in the median number of falls between impedance control and no prosthesis walking in the no

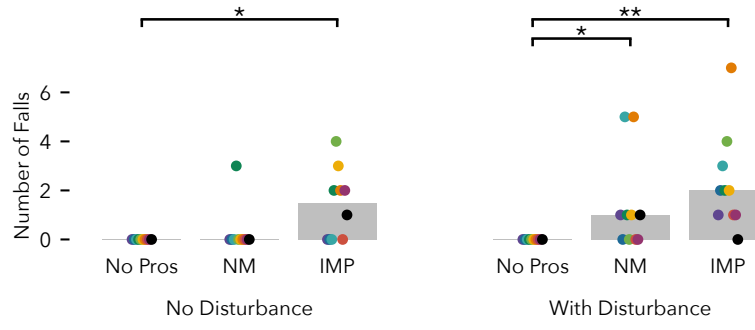


Figure 7.5: Total number of falls across all trials in both the undisturbed and disturbed walking conditions when walking without the prosthesis (No Pros) and with the Neuromuscular (NM) prosthesis control and impedance (IMP) prosthesis control. Grey bars show the median number of falls across all subjects. Statistical significance assessed by Wilcoxon signed-rank test. *: $p < 0.05$, **: $p < 0.01$.

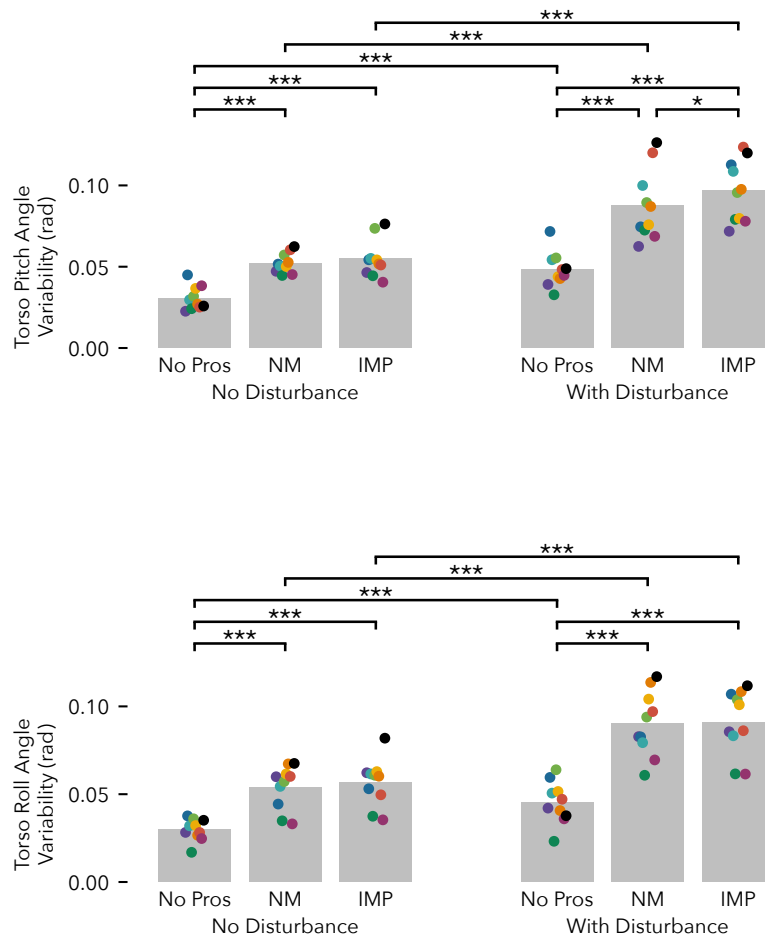


Figure 7.6: Torso pitch angle variation. Angle variation calculated as the interquartile range of torso angles after the median torso angle trajectory over the strides in a trial is subtracted out. For the prosthesis trials, we report the average variation across the five trials for each condition. Grey bars show the mean across subjects. Statistical significance assessed by paired t -tests. *: $p < 0.05$, ***: $p < 0.001$.

Figure 7.7: Torso roll angle variation. Angle variation calculated as the inter quartile range of torso angles after the median torso angle trajectory over the strides in a trial is subtracted out. For the prosthesis trials, we report the average variation across the five trials for each condition. Grey bars show the mean across subjects. Statistical significance assessed by paired t -tests.* * *: $p < 0.001$.

disturbance case and both impedance and neuromuscular walking in the disturbance case. No significant differences were found directly between the neuromuscular and impedance controllers.

Figures 7.6 and 7.7 show the torso pitch and roll angle variability respectively. We see significant differences between the no prosthesis and with prosthesis cases as well as the no disturbance and with disturbance cases. There is also a significant increase in torso pitch variability with the impedance control compared to the neuromuscular control in the disturbance case.

Finally, table 7.2 shows a tally of the reasons for the observed falls with each controller type when using preferred parameters. We manually determined the reason for each fall by analyzing video recordings, motion capture data, and logged prosthesis data. The first four categories refer to general losses of balance resulting in a fall in the four cardinal directions. Backward falls generally resulted from

Fall Types	Neuromuscular	Impedance
Fall Forward	1	0
Fall Backwards	6	4
Fall Left	1	0
Fall Right	0	3
Missed Stance / Swing Transition	3	0
Missed Stance 2 / Stance 3 Transition	0	7
Knee Collapse	0	15
Swing Trip	4	12

Table 7.2: Tally of observed reasons for falls across all subjects and across both the undisturbed and disturbed walking conditions. Falls were manually classified based on video and logged prosthesis data. An individual fall can be assigned to more than one reason.

the treadmill suddenly stopping when the prosthesis stance leg was still in front of the body, causing a loss of balance backwards. The falls forward, left and right were generally more ambiguous in their cause, but may be due to improper leg placement.

The missed stance/swing transitions in the neuromuscular control were caused when subjects did not allow the leg angle to cross the 90° threshold set in stance/swing state machine (compare fig. 4.9). The missed stance 2/stance 3 transitions occurred with impedance control if the user did not dorsiflex the ankle sufficiently to trigger the transition. This could cause the knee to produce an extension torque in late stance, making it difficult to enter the swing phase (compare fig. 7.3). As shown in fig. 7.8, the rate at which the impedance controller failed to transition through all three stance phases significantly increased with the introduction of disturbances.

In contrast, the knee collapse fall type was triggered in impedance control if the user dorsiflexed the ankle too early causing a premature switch to the third phase of stance. In this phase, knee torque typically trends towards zero to allow for passive flexion of the knee heading into swing. However, in the case of a premature switch to the push-off phase, these near-zero knee torques can cause the knee to suddenly collapse under the user's weight.

The last cause of falls, trips during swing, occurred when using both controllers, but 3x more often with impedance control than with neuromuscular control. Many of the swing trips for impedance control were also preceded by a missed stance 2/stance 3 transition. Others occurred when kinematics were drastically changed by the disturbance. For example, several swing trips occurred after a sudden acceleration of the treadmill caused the stance step length to dramatically increase, thereby altering kinematics at toeoff and in swing, and leading to the toe hitting the ground mid-swing.

Finally, we look at the effect of using suboptimal controllers on user ratings and falls. Figure 7.10 shows the median ratings of each

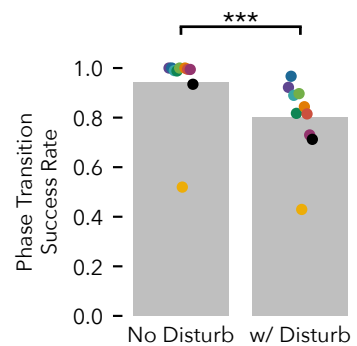


Figure 7.8: Fraction of steps for which impedance control successfully transitions through all three stance phases. Disturbances significantly decrease the transition success rate. Grey bars show the mean success rate across all users. Statistical significance assessed by paired *t*-test. ***: $p < 0.001$.

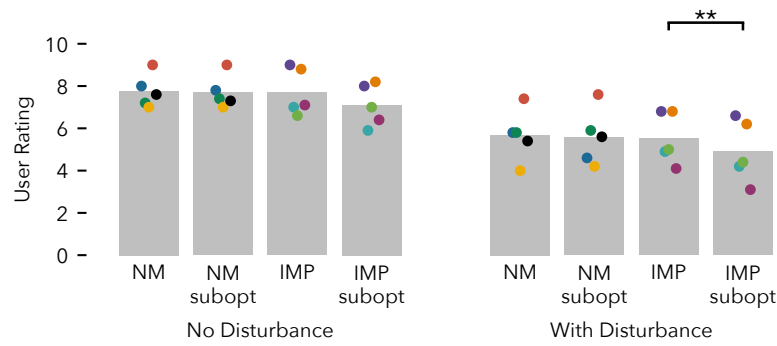


Figure 7.9: Comparison of user scores of optimal versus suboptimal parameters sets for the neuromuscular and impedance control strategies. Grey bars show the mean user rating across subjects. Statistical significance assessed by paired *t*-tests.
**: $p < 0.01$.

the preferred and suboptimal parameters for each controller. For neuromuscular control, we see no significant difference between the preferred controller from day 4 and the suboptimal controllers. In fact for the neuromuscular control with disturbances, 4 out of 5 users slightly preferred the suboptimal control from day 5. On the whole, choosing a suboptimal set of parameters seemed to have a larger effect on impedance control with 4 out of 5 subjects preferring the optimal to suboptimal parameters with out disturbances and all five subjects preferring the optimal impedance parameters to the suboptimal parameters in disturbed case.

Figure 7.10 shows the median number of falls garnered by optimal and suboptimal parameters. In the disturbance case we see a increase in the median number of falls with the suboptimal parameter sets over the preferred parameter sets. However this difference was not significant.

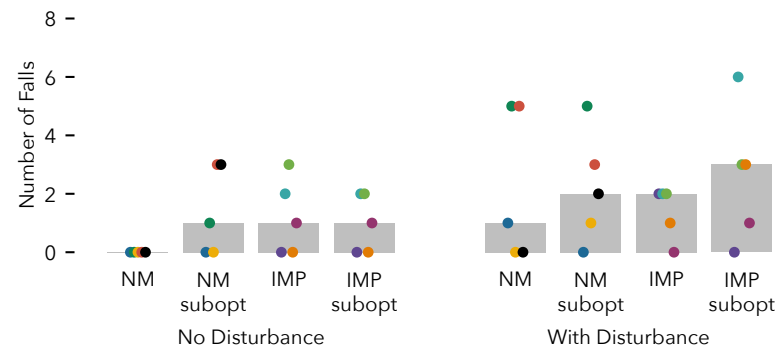


Figure 7.10: Comparison of number of falls of optimal versus suboptimal parameters sets for the neuromuscular and impedance control strategies. Grey bars show the median number of falls across subjects. Statistical significance assessed by Wilcoxon signed-rank test.

7.4 Discussion

In this work, we sought to objectively compare the robustness, user preferences, and reasons for falls of the neuromuscular and impedance control strategies for powered, robotic knee and ankle prostheses. Overall, we found that users rated the neuromuscular control more highly than impedance control and using impedance control led to significantly more falls compared to walking without a prosthesis. While we did observe more falls with the impedance control across all subjects than with the neuromuscular controller, when considering the question, "Did individual users fall more often with impedance control than with neuromuscular control?", these differences were not significant. The only measure of gait stability in which a significant difference between the neuromuscular and impedance controllers was measured was the torso pitch variability, which neuromuscular control significantly reduced in the disturbance case compared to impedance control.

Categorizing the falls by their type gives more insight into differences between the controllers. There were reasons for falls with each controller that did not exist for the other. For NM control, missed transitions between stance and swing caused three falls. While these falls could be directly attributed to the leg-angle threshold in the high level state machine that governs the stance/swing state transition (fig. 4.9), that these falls only occurred with neuromuscular control suggests a causal difference in the two strategies. One possible reason that these falls did not occur with impedance control is that the discrete transition between the second and third stance phases generates a sudden increase in the ankle plantarflexion torque. When walking with impedance control, subjects may have waited to feel this transition before beginning swing. In contrast, neuromuscular control gives no such obvious transition and thus users may attempt to enter swing too early. However, with better sensing of ground reaction forces, the threshold on leg angle would not be necessary, and thus this problem would be resolved.

While impedance control's discrete phase transitions may have helped users avoid missing the stance to swing transition, it directly caused two other failure modes. The first, missed transitions between the second and third phases of stance, occurred if the user did not dorsiflex the ankle enough to trigger the transition. This failure could lead to trips during swing or a later loss of balance. The second, the knee collapse failure mode, happened if the impedance controller switched to the third phase of stance too early, which could cause a sudden reduction in knee extension torque. The fact that individual subjects fell for both of these reasons suggests that we cannot fix

these failure modes by simply tuning the ankle angle threshold that governs the phase transition. Decreasing the threshold to prevent missed transitions would likely cause more knee collapses. Conversely, increasing the threshold would likely cause more missed transitions.

Finally, users suffered from trips during swing when using both stance control strategies, which were both paired with the same minimum-jerk trajectory generation swing control strategy. However, these trips occurred three times more frequently with impedance stance control than with neuromuscular stance control. Many of the trips that occurred with impedance control were preceded by a missed transition between the second and third stance phases. Neuromuscular control, in contrast, is smooth throughout stance with no discrete transitions, and thus may transition to swing more consistently and cause fewer swing trips. Nevertheless, even with its smoother stance phase, subjects still tripped during swing several times with the Neuromuscular control. Therefore, in sections 8.5 to 8.8 we seek to explicitly minimize the risk of tripping by using estimates of the current and future hip height and orientation to plan knee and ankle swing trajectories that avoid premature ground contact.

The smooth stance phase of the neuromuscular model, which eliminates failure modes such as knee collapses and missed stance phase transitions and may help reduce swing trips, comes at the cost of dramatically increased model complexity. The implemented impedance controller has 20 parameters: 3 stance phases \times 2 joints \times 3 parameters per joint per phase + 2 transition parameters. In contrast, the implemented neuromuscular control is more than 4 times as complex as it has 80 parameters: 54 defining muscle-specific mechanical properties, 9 defining shared muscle properties, and 17 defining the neural reflexes.

Of these 80, we chose to only optimize 18 when generating parameter sets in order to avoid local minima and to complete the optimization in a reasonable amount of time. The choice of which 18 parameters to choose was based on trial and error and prior experience with the model. In the clinical setting, the lack of transparency about the function of and interdependencies between the 80 parameters may make practical application of neuromuscular control difficult. Therefore, in order to achieve the potential benefits of a smooth controller that does not have discrete stance phases, while avoiding excessive complexity, in chapter 9, we explore an alternative approach to stance control. This approach relies on a continuous estimate of phase and easily interpretable models for the output behavior as a function this phase estimate.

A surprising result of this experiment is the lack of substantial differences between suboptimal and optimal controllers. Only in the case of impedance control under disturbances did subjects unanimously restate their preference for the control parameter sets they had preferred on the optimization day. The lack of clear differences between the neuromuscular parameter sets could be the result of the neuromuscular model generally being less sensitive to its parameters than the impedance controller. For example, large differences in behavior between impedance control parameter sets can result if one set of parameters causes many missed phase transitions and another parameter set does not. Another reason for the lack of clear difference in user ratings could be the difference in the query. During the optimization procedure, subjects were asked to directly prefer one parameter set to other after short ~ 10 sec bouts of walking with each parameter set. In contrast, on the data collection day, parameter sets were independently rated on a 1-10 scale after 2 minutes of walking. In future work, we should check for consistency of the preferred parameters by performing the dueling bandits optimization procedure on multiple days in order to see if the users preferences are consistent from day to day.

Our simulated results presented in chapter 5 predicted a larger difference between controllers that was not borne out by this experiment. In future work, the motion capture data collected during these trials should be used to improve the neuromuscular model so that researchers can perform experiments investigating prosthetic device performance with a higher likelihood that those results translate to the real world. Reliable predictive models would vastly reduce the time it takes to iterate prosthesis controller designs.

This study has several limitations that should be addressed in future work. First, we only performed the study with ten subjects, which made establishing the statistical significance of the results difficult. Limiting the number of subjects was necessary due to the substantial practice time required for subjects to achieve reliable handrail-free walking with the prosthesis. Furthermore, there were several subjects who could not proceed past the first day of the experimental procedure as they could not manage to walk without the handrails or experienced excessive discomfort in the prosthesis adaptor. While researchers should eventually perform adequately powered studies comparing prosthesis controllers in the future, at this point in the development of these controllers, there are still significant issues in the prosthesis control that can be discovered and addressed with small n studies. In the case of a safety critical device like a prosthesis, all causes of falls should be systematically addressed even if they are rare and their frequency cannot be estab-

lished to a high degree of confidence.

Second, we tested very specific implementations of the impedance and neuromuscular controllers. Specifically, our impedance control implementation utilized linear impedance functions, as in Sup et al. [2009], and phase transition rules based on joint angle thresholds, as in Lawson et al. [2014]. However, other variations on the impedance control have been suggested as well, including those that use nonlinear impedance functions [Sup et al., 2007, Shultz et al., 2016] and those using ground reaction signals for the transitions between phases [Sup et al., 2009]. The neuromuscular control structure we used was described in section 4.6 and based on Song and Geyer [2015]. This structure encodes a specific set of reflexes. However, there are many other feedback pathways that could be incorporated into this model as well that may improve performance. Additional experiments will be needed to compare amongst variations in these control strategies.

Finally, in this experiment, users needed to pick parameters out of a pre-generated discrete set of possibilities. It is possible and likely that there exists parameters for each control that are more robust, comfortable, and efficient. However, finding these parameters by solving a high dimensional optimization problem using real prosthesis feedback remains an unsolved problem for three reasons: First, optimizations suffer from the curse of dimensionality. Recently, Wen et al. [2019] optimized 12 parameters of a robotic knee/pассив ankle prosthesis, a significant improvement from prior approaches. However, this approach is still insufficient for impedance control of both the knee and ankle joints, which requires 20 parameters. In our work, the parameter generation approach tackles the dimensionality through a large amount of offline computation.

Second, it is unclear what objective function to use in the optimization. For example, Wen et al. [2019] target a desired knee angle trajectory. However, perfect tracking of this trajectory may come at the expense of robustness or comfort. In this experiment, we allowed users to specify their own objective through their preferences. In future work, similar preference-based approaches could be used to identify an objective function, made up of weighted gait features, that aligns with user preferences. An optimization approach, such as Wen et al. [2019], could then be used to target this objective function if it can be scaled to the required number of dimensions.

The final challenge for performing the full optimization is that many important features we would use to quantify gait are difficult to measure. For example, to measure gait robustness using treadmill velocity disturbances, we required many minutes of walking under disturbances just to observe a few falls. Metabolic energy consump-

tion typically takes several minutes to observe, even when using a predictive model of its steady state value [Zhang et al., 2017]. Other gait features such as comfort are not directly quantifiable. Identification of quickly measurable stand-ins for these metrics should be a focus of future research.

Reactive Swing Control for Trip Avoidance

Material in this section based on Gordon et al. [2019]¹ and Thatte et al. [2019]²

The experimental results from chapter 7, in which we compared neuromuscular and impedance control, revealed that trips during swing were one of the most common causes for falls (table 7.2). In this chapter we explore two potential methods for avoiding swing trips. The first focuses on avoidance of obstacles during gait through online learning of classifiers that can recognize the user’s obstacle avoidance intent. In the second, we directly address the trips during normal walking that were observed in chapter 7 by planning swing trajectories that use an estimate of the user’s hip height and orientation to avoid premature ground contact.

8.1 Classification Approach Introduction

Avoiding obstacles on the ground is a necessity for maintaining safety while performing a variety of locomotion tasks. This behavior requires anticipation of an obstacle and active leg control strategies to avoid it [Patla and Prentice, 1995]. Transfemoral amputees, however, have a compromised ability to negotiate obstacles, as shown in Figure 8.1, as current prosthesis technology relies on mechanically passive knees that necessitate significant compensation at the hip in order to replicate able-bodied trip recovery strategies [Shirota et al., 2015]. Compromised ability to avoid and recover from trips may contribute to the large number of falls that leg amputees suffer. For instance, 58% of unilateral amputees reported a fall within a year [Kulkarni et al., 1996]. Moreover, the fear of falling can cause amputees to avoid activity, leading to further deterioration of their physical condition [Miller et al., 2001].

An increasing availability of powered prostheses in research labs provides the opportunity to study active obstacle avoidance strategies

¹ Max Gordon, Nitish Thatte, and Hartmut Geyer. Online learning for proactive obstacle avoidance with powered transfemoral prostheses. In *Robotics and Automation (ICRA), 2019 IEEE International Conference on*. IEEE, 2019

² Nitish Thatte, Nandagopal Srinivasan, and Hartmut Geyer. Real-time reactive trip avoidance for powered transfemoral prostheses. In *Proceedings of Robotics: Science and Systems*, 2019



in prosthetics, although so far only a limited number of studies exist on this topic. These studies focus on detecting and classifying the correct response strategy after the amputee has tripped. For example, Lawson et al. [2010] developed a classifier that uses fast Fourier transform and the root mean square of accelerometer data as features to classify stumbles and recovery strategies, respectively. Zhang et al. [2011a] found that adding EMG signals from the residual limb to accelerometer data can help reduce false positives for stumble and strategy detection. Finally, Shirota et al. [2014] identified the optimal sliding window lengths and increments for feature calculation for trip detection and strategy selection classifiers. While detecting and classifying trip recovery strategies after their occurrence is a necessary step towards improving gait robustness, it does not provide a proactive prosthesis control strategy that prevents obstacle encounters in the first place.

Another major drawback of the previous studies is that they train and test classifiers offline. However, a deployed trip classifier needs to function online and deal with temporal adaptation of the learner and amputee. The adaptation is required as the obstacle avoidance behavior triggered by a trip classifier alters the amputee's movements and, therefore, the data used to train the classifier. Consequently, trip classifiers trained offline may be ineffective due to a mismatch of training and testing data. In section 2.3 we reviewed high-level classifiers that detect transitions between gait modes such as standing, level ground walking, and stair/ramp ascent/descent. In that setting,

Figure 8.1: a) Utilizing minimum jerk trajectories during swing does not allow for appropriate adaptation of swing trajectories to enable obstacle avoidance. b) Our adaptive system learns online to detect the presence of an obstacle from the amputee's late stance/early swing movements. Once detected, the controller modifies the trajectories of the knee and ankle to achieve improved obstacle clearance.

classification approaches often run into a similar problem of training and testing data mismatch. Spanias et al. [2018] provides a method of rectifying this data distribution mismatch.

Here we present the first pilot study that combines online learning and proactive control of a powered transfemoral prosthesis to implement obstacle avoidance in amputee locomotion. The obstacle avoidance system uses early-swing measurements of the residual limb angle, angular velocity, and linear acceleration to recognize in-process obstacle avoidance attempts. To address the online learning aspect of this system, we adapted the method proposed by Spanias et al. [2018] for online learning of gait mode classification. We also changed the existing swing leg behavior of the prosthesis to facilitate obstacle avoidance. This change includes a regression to predict the appropriate degree of knee and ankle flexion given the user's previous obstacle response motions. Finally, we evaluated the system behavior in trials with both non-amputee and amputee subjects.

8.2 Classification Approach Methods

8.2.1 Forward-Backward Classifier

In order to learn to classify trips online with minimal hand-labeling of data, we rely primarily on the forward-backwards classifier approach first proposed by Spanias et al. [2018] for the purpose of classifying different modes of gait such as level ground walking, standing, and stair climbing. In their work, a *forward classifier* predicts the next step's gait mode using data in a window shortly before the transition. In parallel, a *backward classifier* labels completed steps with their correct gait mode in hindsight. Because the backwards classifier has access to features from the completed step, it can achieve accurate labels with a small amount of hand-annotated data. Once trained, the backwards classifier can provide labels for training the forward classifier, obviating the need for further hand-labeling of steps.

In our work, the forward classifier predicts, shortly after toe-off, if the upcoming swing will require obstacle avoidance or not. For this purpose, we use a linear support vector machine and features of the residual limb motion in the last 210 ms of stance and first 90 ms of the swing phase. Because user behavior changes over time in response to changes in prosthesis obstacle avoidance behavior, we retrain the forward support vector machine every ten steps using labels from the backward classifier.

The backward classifier is another linear support vector machine, trained once for each user, which uses features extracted from the

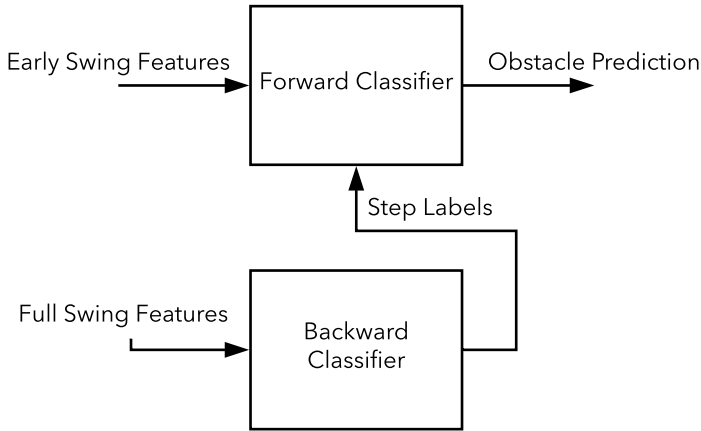


Figure 8.2: Forward-Backward Classifier Overview. The backwards classifier uses features from the entire swing to provide training class labels to a forwards classifier. The forwards classifier uses features from late stance and early swing in order to predict if an upcoming swing will be an obstacle avoidance attempt.

entire swing phase to label a step as an avoidance attempt after the fact. To train the backwards classifier we hand label obstacle avoidance attempts and normal steps for roughly ten obstacles. Figure 8.2 provides an overview of this system.

8.2.2 Target Knee Angle Regression

A prosthesis user will not always encounter obstacles of the same height. As the obstacle avoidance response can be disruptive to the user, it is desirable to give the user control over the magnitude of the prosthesis response. We seek to achieve this functionality by using the normalized backward classifier score as a metric for the difficulty of avoiding an obstacle. We then implement a simple linear feedback law that assigns higher target flexion knee angles to obstacle avoidance attempts that are more difficult according to this metric. Figure 8.3 outlines this feedback mechanism, which has the form

$$\theta_{n+1}^{tgt} = \theta_n^{tgt} - k_{decay}(\theta_n^{tgt} - \theta_{min}) + k_{score}\hat{\xi}, \quad (8.1)$$

$$\hat{\xi} = \frac{\xi - \xi_{10^{\text{th}} \text{ percentile}}}{\xi_{90^{\text{th}} \text{ percentile}} - \xi_{10^{\text{th}} \text{ percentile}}}, \quad (8.2)$$

where θ_{tgt} is the current target angle for a given set of features, n is the current time step, k_{decay} is a gain that prevents continual target angle growth by decaying target angles towards θ_{min} , and k_{score} is a gain on the normalized class score, $\hat{\xi}$. The system shifts class scores, ξ , so that scores below the 10th percentile of tripped step scores result in a reduction of the target knee angle. Furthermore, the system normalizes the scores by $\xi_{90^{\text{th}} \text{ percentile}} - \xi_{10^{\text{th}} \text{ percentile}}$ so that the gain k_{score} has a predictable effect across subjects whose score ranges vary.

The system fits the target knee angles with a linear support vector

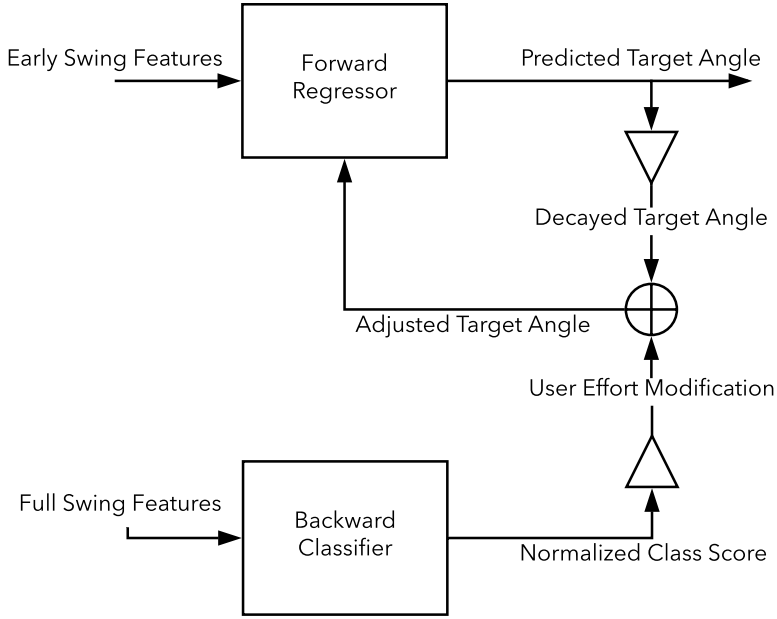


Figure 8.3: Knee Angle Regression Feedback. In order to enable volitional control of the knee and ankle flexion angles to allow users to achieve greater flexion angles for larger obstacles, we implement a feedback system that uses the backwards classifier class score to quantify obstacle difficulty. After each step, the system increases the desired target angle for that step’s forward features proportionally to the normalized back classifier score. We also decay the current desired target angle for those features to prevent continual growth of the target angle. The regression is retrained every ten avoidance attempts.

regression. Every time the trip avoidance triggers, it appends an additional target angle, specified by eq. (8.1), to a training data set. The system retrains the regression using this data set every ten trip avoidance steps.

8.2.3 Feature Extraction

For the forwards and backwards classifiers, as well as the target knee angle regression, we use features of the thigh angle, angular velocity, and linear accelerations in a time window. Specifically, we use the mean, standard deviation, minimum value, and maximum value of each signal. For forward classification and regression the time window begins 210 ms before toe-off and ends 90 ms after toe-off, while for the backward classification we use a window consisting of the entire swing phase between toe-off and heel strike.

8.2.4 Trajectory Planning

To generate the knee and ankle motions for unperturbed swing, we use the minimum jerk swing control outlined in section 4.6 and first proposed by Lenzi et al. [2014b]. This swing control scheme generates and follows human-like trajectories for the knee and ankle joints that start at the toe-off angle, angular velocity, and angular acceleration of each joint, go to target flexion states, and then extend to desired final angles at the estimated heel strike time. We estimate the swing period to be 65% of the stance period.

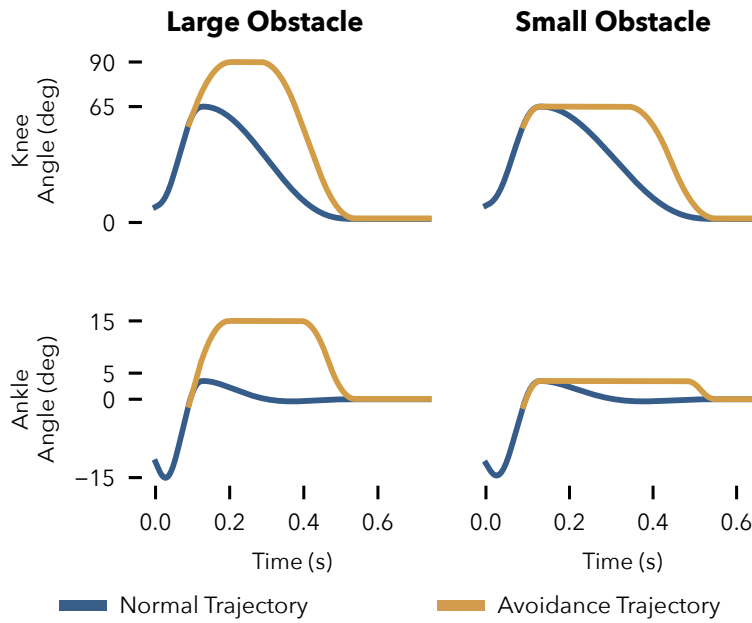


Figure 8.4: Bang-bang obstacle avoidance trajectories (yellow) vs normal minimum jerk trajectories (blue) for the knee and ankle.

When the forward classifier triggers an obstacle avoidance attempt, we switch to bang-bang trajectories for the knee and ankle joints. These trajectories maximize foot clearance while respecting joint angle, velocity, and acceleration limits. The bang-bang trajectories achieve desired flexion angles as quickly as possible and then extend as late as possible such that they achieve extension before the predicted heel strike time. The trajectory planner uses the target knee angle regression to determine the appropriate peak angle for the knee trajectory, while the ankle trajectory's target flexion angle is a linear function of the knee's target angle. The knee trajectory's peak flexion angle is constrained to lie within 65 and 90 degrees while the peak ankle flexion is constrained within 5 and 15 degrees. Examples showing the minimum jerk swing trajectories and obstacle avoidance trajectories planned for large and small obstacles are given in fig. 8.4.

8.2.5 Experimental Protocol

We tested the ability of the proposed online learning system to accurately classify trips and normal swings, help subjects avoid tripping on obstacles, and modulate knee and ankle flexion appropriately for obstacles of different heights. To evaluate these aspects of system performance, we conducted experiments with the powered knee and ankle prosthesis previously described in chapter 3.

Two subjects, one non-ampetee with prior experience using this prosthesis, and one inexperienced amputee subject, performed walk-

ing trials with the obstacle avoidance system enabled. As subjects walked, an experimenter placed objects on the treadmill belt in front of each subject's prosthetic leg, necessitating an obstacle avoidance reaction. To obtain a baseline performance level for non-reactive prosthetic swing control, we also performed obstacle avoidance trials with the minimum jerk swing trajectories designed for undisturbed swing. Before the online trials, the backwards classifier was trained for the prosthesis user with 75 steps. The able bodied subject completed 446 total steps, with 53 box avoidance steps, while the amputee completed 222 total steps, with 40 box avoidance steps. The amputee subject performed trials in an ABBA order, where A is minimum jerk control and B is the reactive control, in order to average out potential learning effects. The amputee subject also had an additional practice session the day prior to the box avoidance trials in which he acclimated to walking with the powered prosthesis without obstacles.

8.3 Classification Approach Results

8.3.1 Results

Tables 8.1 and 8.2 show the overall classification accuracies, sensitivities, and specificities for the forward and backwards classifiers for the able-bodied and amputee subjects respectively. The forward and backwards classifiers for both subjects achieve high specificity (the number of normal steps classified correctly) and accuracy (> 95%). The sensitivity, the percentage of true trips classified correctly, of the classifiers for both subjects is substantially lower than the specificity or accuracy. For the forward classifier, we see that because the model is trained online, the sensitivity improves from the first half of the trial to the second half, which explains some of the low overall sensitivity.

Controller	Classification Accuracy	Sensitivity	Specificity
Forward, 1 st Half	96%	73%*	99%
Forward, 2 nd Half	99%*	93%‡	99%
Forward Overall	98%	85%‡	99%
Backward	99%	100%‡	99%

Importantly, the ability of the forward classifier to correctly trigger the bang-bang obstacle avoidance trajectories improves obstacle avoidance success rates as shown in table 8.3. Both subjects were able to avoid significantly more obstacles with the obstacle avoidance controller than with the minimum jerk trajectory controller.

We also compared our online learning approach for obstacle avoid-

Table 8.1: Classifier performance ³, able-bodied steps: 446, Avoidance attempts: 53

³* $\implies p < 0.05$, ** $\implies p < 0.01$, *** $\implies p < 0.001$, Chi-squared test

Controller	Classification Accuracy	Sensitivity	Specificity
Forward, 1 st Half	95%	80%	98%
Forward, 2 nd Half	96%	85%	98%
Forward Overall	95%	83%	98%
Backward	98%	90%*	99%

Table 8.2: Classifier performance, amputee, total steps³: 222, Avoidance attempts: 40

Controller	Able-Bodied Success Rate	Amputee Success Rate
Minimum Jerk	37%‡	35%‡
Adaptive Bang-Bang	89%	71%

Table 8.3: obstacle avoidance success rates³

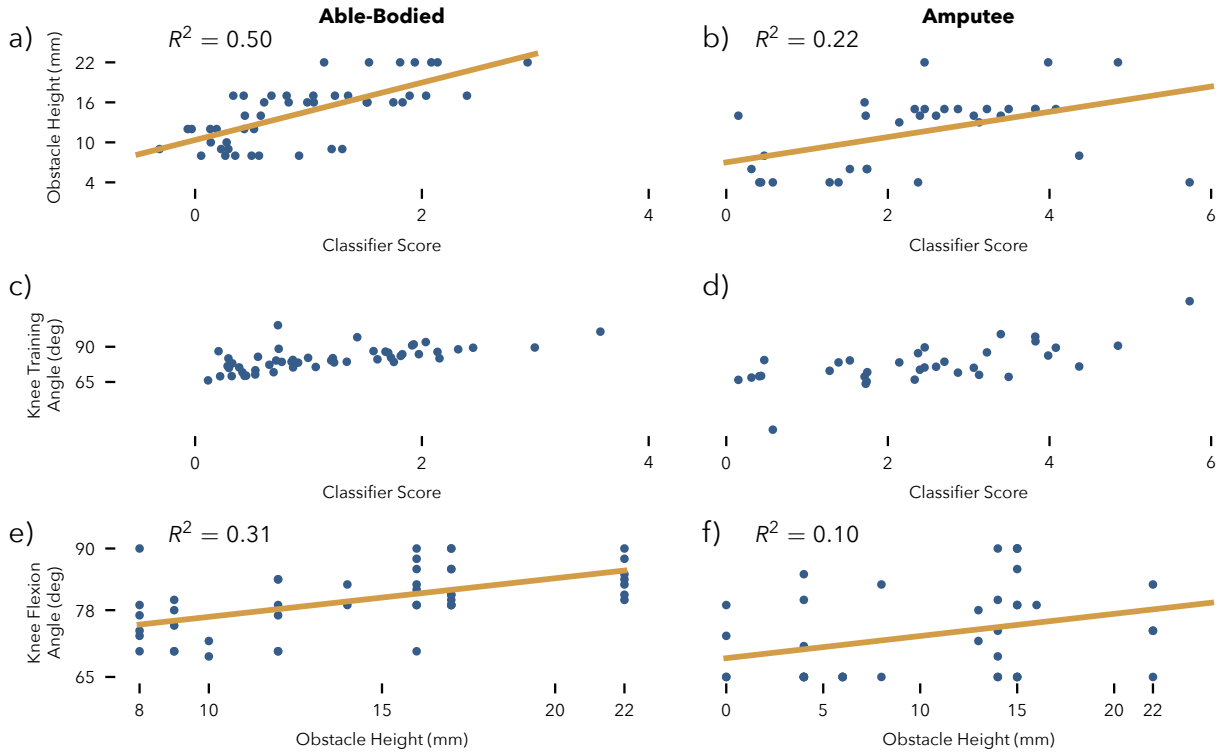
ance to an offline approach similar to that taken by Lawson et al. [2010], Zhang et al. [2011a], and Shirota et al. [2015]. To do this, we trained a classifier offline using the first half of the amputee subject's bang-bang control data and tested it on the second half of the data. Table 8.4 shows that the classifier trained offline has trouble generalizing to the second half of the data, as it performs significantly worse than the online-trained model in terms of accuracy and sensitivity.

Classifier	Classification Accuracy	Sensitivity	Specificity
Offline	89%	39%‡	100%
Online	95%*	83%	98%

Table 8.4: Online and Offline Forward Classifier Performance, Amputee³

Finally, we examined the ability of the knee angle regression to choose a target knee angle that is appropriate for the object size. The feedback law proposed in eq. (8.1) assumes we can use the backwards classifier score as a metric of obstacle difficulty. For the able-bodied subject, this assumption seems warranted, as there is a strong relationship between the obstacle height and the classifier score (fig. 8.5a, $R^2 = 0.50$). However, for the amputee subject, who was less experienced with walking with the powered prosthesis, this relationship is less clear (fig. 8.5B, $R^2 = 0.22$).

As shown in fig. 8.5c&d, our system is able to ensure that high classification score steps, associated with high user effort, obtain larger target flexion angles. This relationship led to noisy volitional control of the knee flexion angle for the able-bodied subject (fig. 8.5e) as evidenced by the linear relationship between knee angle and obstacle height ($R^2 = 0.31$). However, for the amputee subject, there is no clear relationship between the obstacle height and knee flexion angle (fig. 8.5f, $R^2 = 0.10$).



8.4 Classification Approach Discussion

We developed an online learning system to help users of powered transfemoral prostheses avoid obstacles. Our system uses information from an inertial measurement unit during the late stance to early swing period to classify the upcoming swing as either normal or a trip avoidance attempt. Unlike previous work on obstacle negotiation for transfemoral prostheses [Lawson et al., 2010, Zhang et al., 2011a, Shirota et al., 2014], our system learns online on an actual transfemoral prostheses. We compared the classification performance of our online system with a hypothetical offline system using online trials to provide testing and training data for offline analysis. This comparison showed that the online learning system provided an improvement in sensitivity and accuracy to obstacle avoidance attempts. Both an experienced, able-bodied subject and an inexperienced, amputee subject were able to improve their obstacle avoidance success rates significantly. However, only the experienced, able-bodied subject was able to achieve some level of volitional control of the prosthesis flexion as a function of obstacle height.

There are several reasons why the amputee subject may not have

Figure 8.5: Obstacle height vs backwards classifier score for (a) the able-bodied and (b) amputee subjects. The system uses the backwards classifier score as a metric for obstacle avoidance difficulty. This score is used in a feedback loop that forms the training set for the flexion target angle regression (c-d). With this feedback system, the able bodied user (e) is able to achieve a degree of volitional control over flexion angle as evidenced by the linear relationship between knee flexion angle and obstacle height ($R^2 = 0.31$). However, the amputee (f) was not able to achieve meaningful control over the flexion of the prosthesis ($R^2 = 0.10$), possibly due to the decreased experience level of this subject.

been able to achieve volitional control of prosthesis flexion. First, the amputee had far less experience using the prosthesis than the able-bodied subject. Consequently, even though both subjects were informed that trying harder to lift the leg over bigger obstacles would likely lead to greater flexion once the prosthesis learns, it is likely that only the first subject was able to incorporate and implement this information. The amputee may have concentrated on more rudimentary aspects of gait, as evidenced by his use of the handrails to walk, whereas the able-bodied subject did not need to use the hand rails. Moreover, the amputee's socket may have provided less control over the prosthesis than did the intact subject's able-bodied adapter (shown in fig. 3.12). Finally, we noted that the relationship between joint flexion and obstacle height tended to oscillate over the course of our trials. This may imply that the gains we used for the target knee angle regression (eq. (8.1)) were too high.

Before settling on the specifics of the obstacle avoidance system presented here, we also tested other options for its components. For example, we also evaluated incorporating EMG signals from the non-prosthetic limb in our obstacle avoidance classifier. Previous research showing that able-bodied subjects utilize stance leg musculature to help raise the hip during obstacle avoidance motivated this choice of EMG placement [Patla and Prentice, 1995]. However, as was found by Spanias et al. [2018], using EMG data along with mechanical data in the forwards-backwards online learning algorithm did not seem to improve classification accuracy, which is already high. This lack of improvement may also result from a significant delay in our wireless EMG sensors (Delsys Trigno). It is possible that a low-latency wired EMG sensor would be able to improve classification performance or the performance of the target angle regression.

We also tried using imitation learning techniques to model able-bodied strategies for stepping over obstacles. Specifically, we employed maximum margin inverse optimal control [Ratliff et al., 2007] to learn, offline, cost functions for the knee that explained obstacle avoidance trajectories. However, when used online, the generated trajectories tended to diverge and produce unexpected results because the initial toe-off state of the prosthesis did not match those in the able-bodied data set. For the obstacle avoidance classifier, we correct this sort of offline-online mismatch via the backwards classifier that provides labels to train the forwards classifier online. It is less clear how to update trajectories in hindsight as we never see the obstacle. For this reason, we used bang-bang trajectories during obstacle avoidance, which maximize the time the joints remain flexed.

In the future, this issue could be solved by incorporating a laser distance sensor into the prosthesis. This sensor could enable precise

measurement of the ground and obstacle shape during the initial part of swing as the hip moves forward. We could then use this information to explicitly plan knee and ankle trajectories that will avoid the obstacle and the floor until the appropriate touch down time. In the second half of this chapter, we present an initial step in this direction in which we incorporate information from a laser distance sensor to plan swing trajectories that help prevent trips on flat terrain.

There are several other limitations of the current study we should address in future work as well. First, we only tested the algorithm with two subjects. More subjects of varying skill levels are necessary to determine how applicable the system is to a broader population. Additionally, a likely reason why the forward classifier's sensitivity was relatively low, was that there were many more normal steps than obstacle avoidance attempts in the training data set. This may cause the SVM loss function's minimum to focus more heavily on classifying normal steps correctly. Deploying this system on a commercial prosthesis, for which trips are more rare, would exacerbate this issue. Therefore, future development should investigate how to train a classifier given heavily unbalanced class frequencies.

8.5 Planning Approach Introduction

Lower limb amputees using state of the art commercial prostheses face a number of gait deficiencies that negatively impact their quality of life [Gauthier-Gagnon et al., 1999]. Of acute significance among these deficiencies are the increased risk of falling and the related injuries, which can lead to amputees avoiding activity out of a fear falling [Miller et al., 2001]. As falls and their avoidance are linked to swing leg placement in locomotion, active swing control strategies could help to substantially reduce the risk of falling. However, current swing controllers of transfemoral prostheses do little to proactively minimize this risk.

Existing swing phase control approaches for powered prostheses predominantly seek to reproduce the average swing phase behavior of the human leg. Whether the approach is based on trajectory planning [Lenzi et al., 2014b], impedance control [Sup et al., 2009], or phase-based control [Quintero et al., 2016], they all treat the swing phase motion as an “open loop” problem with respect to trip hazards, as none of the approaches take the location of the heel and toe of the prosthetic foot with respect to the ground explicitly into account. Therefore, current swing control strategies neglect a clear advantage that robotic prostheses can have over their passive counterparts: the ability to sense and act upon environmental information.

Consequently, as shown in table 7.2, trips during swing may pose a significant hazard to users of powered prostheses.

In this work, we develop a swing control strategy to reactively avoid trips with powered transfemoral prostheses that uses visual information about the environment and an estimate of the prosthesis configuration. Some previous studies have explored incorporating visual feedback into the control of leg prostheses. For example, Scandaroli et al. [2009] developed a state estimator and controller that allowed the ankle joint of a prosthesis to conform to the slope of the ground under the foot. To address the problem of terrain recognition, Zhang et al. [2011b] developed a classifier using a LIDAR and an IMU to discriminate between terrains such as flat ground and steps. More recently, Liu et al. [2016] combined this terrain classifier with a Bayesian intent classifier (based on [Du et al., 2012]) to develop an environment-aware locomotion mode recognition system. In addition, RGBD sensors have been explored as a source of rich environmental information for legged assistance, including gait recognition [Massalin et al., 2017] and stair detection [Krausz et al., 2015, Duan et al., 2018]. However, none of these previous studies have implemented a control strategy that uses environmental information to reactively govern the motion of a powered prosthesis in real-time.

We present such a real-time reactive control of a powered prosthesis that combines three building blocks. First, we use an extended Kalman filter (EKF) that fuses measurements from an IMU, a LIDAR, and encoders on the prosthesis to estimate the current pose of the prosthetic leg with respect to the ground. Second, we predict likely future leg trajectories with sparse Gaussian process models learned online during swing. Finally, we use the leg pose estimate and trajectory predictions in a fast quadratic-program planner to reactively generate in real time leg joint trajectories that avoid premature toe and heel contact with the ground. To evaluate the proposed control, we compare our method for trip avoidance to a standard non-reactive minimum-jerk trajectory planning approach in a prosthesis walking experiment designed to elicit trips.

8.6 Planning Approach Methods

The trip avoidance control we propose involves (1) estimating the position and orientation of the leg (section 8.6.1), (2) predicting the future hip angles and heights (section 8.6.2), and (3) planning corresponding knee and ankle trajectories such that the heel and toe will not contact the ground prematurely (section 8.6.3).

8.6.1 Extended Kalman Filter for estimating Leg Position/Orientation

To estimate the position and orientation of the leg, we employ an EKF that fuses information from a LIDAR distance sensor (SICK OD1000), an IMU (YEI Technologies 3-Space sensor), and encoders on the prosthesis (Renishaw Resolute, Netzer DS-25). The EKF filters the nonlinear, discrete-time dynamics given by

$$\begin{aligned} x_t = \begin{bmatrix} q_t \\ p_t \\ \dot{p}_t \end{bmatrix} &= \begin{bmatrix} f_{\text{gyro}}(\omega_t) & 0 & 0 \\ 0 & I_{3 \times 3} & \Delta t I_{3 \times 3} \\ 0 & 0 & I_{3 \times 3} \end{bmatrix} x_{t-1} \\ &+ \begin{bmatrix} 0 \\ \frac{1}{2} \Delta t^2 I_{3 \times 3} \\ \Delta t I_{3 \times 3} \end{bmatrix} \begin{bmatrix} R_{\text{OI}}(q_{t-1}) a_t - \begin{bmatrix} 0 \\ 0 \\ g \end{bmatrix} \end{bmatrix} + w_t \quad (8.3) \\ &= f(x_{t-1}, u_t) + w_t, \end{aligned}$$

where q is the quaternion orientation, R_{OI} and p are the rotation matrix and position of the IMU in inertial coordinates, ω is the angular rate measured by the gyroscope, f_{gyro} integrates the gyroscope rate to update the orientation, a is the accelerometer measurement, $u_t = [\omega_t, a_t]^T$, and Δt is the integration time step (1 ms).

The dynamics are corrupted by process noise $w_t \sim \mathcal{N}(0, Q_t)$ due to the inaccuracy of the IMU's measurement of the true acceleration and angular velocity. Consequently, Q_t is given by

$$Q_t = \frac{\partial f}{\partial u} \Big|_{x_{t-1}, u_t} \begin{bmatrix} \sigma_\omega^2 I_{3 \times 3} & 0 \\ 0 & \sigma_a^2 I_{3 \times 3} \end{bmatrix} \frac{\partial f}{\partial u} \Big|_{x_{t-1}, u_t}^T, \quad (8.4)$$

where σ_ω^2 and σ_a^2 are the gyroscope and accelerometer measurement variances, respectively.

To estimate the pose given our sensor measurements, we follow a standard EKF procedure [Anderson and Moore, 1979], reviewed here for completeness. The EKF state estimation process has two steps: First, we *predict* the next state distribution by forward-propagating the mean $\hat{x}_{t-1|t-1}$ and covariance of the state estimate $\Sigma_{t-1|t-1}$ using the dynamics given by eq. (8.3),

$$\hat{x}_{t|t-1} = f(\hat{x}_{t-1|t-1}, u_t) \quad (8.5)$$

$$\Sigma_{t|t-1} = F_t \Sigma_{t-1|t-1} F_t^T + Q_t, \quad (8.6)$$

where $F_t = \partial f / \partial x|_{\hat{x}_{t-1|t-1}}$.

Next, we incorporate information from noisy sensor observations to *update* the state estimate. To do this, we utilize a observation model given by $z_t = h(x_t) + v_t$, where $v_t \sim \mathcal{N}(0, R)$, and the

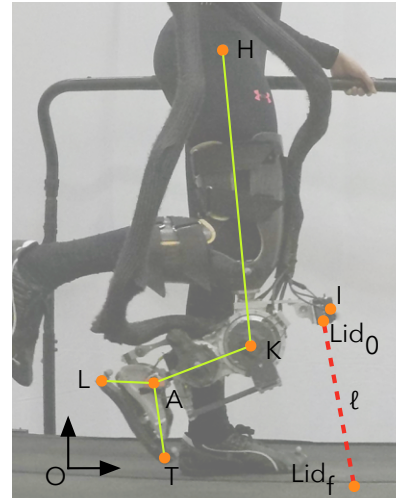


Figure 8.6: Kinematic model of the user and prosthesis used for state estimation and motion planning. The model includes the hip (H), knee (K), ankle (A), heel (L) and toe points (T). Additionally, the start (Lid_0) and end (Lid_f) points of the LIDAR beam (with length ℓ) are indicated. The IMU is located at point I. Both the LIDAR and IMU are mounted to the thigh portion of the powered knee-and-ankle prosthesis.

following update equations:

$$K_t = \Sigma_{t|t-1} H_t^T \left(H_t \Sigma_{t|t-1} H_t^T + R \right)^{-1} \quad (8.7)$$

$$\hat{x}_{t|t} = \hat{x}_{t|t-1} + K_t (z_t - h(\hat{x}_{t|t-1})) \quad (8.8)$$

$$\Sigma_{t|t} = (I - K_t H_t) \Sigma_{t|t-1} \quad (8.9)$$

where z_t are the actual sensor measurements and $H_t = \partial h / \partial x|_{\hat{x}_{t-1|t}}$.

The observations in our EKF formulation use the kinematic model shown in fig. 8.6. We calibrate this model using ground truth data from a VICON motion capture system. In our application we incorporate three observations:

1. The expected acceleration vector points up in the global coordinate frame,

$$h_1(x_t) = \{R_{OI}(q)\}_{\text{row } 3} \quad (8.10)$$

$$z_1 = a \quad (8.11)$$

2. The expected LIDAR measurement given the position of the IMU,

$$h_2(x_t) = \left\{ \ell : \{p_{OLID_f}(x_t, \ell)\}_{\text{row } 3} = 0 \right\} \quad (8.12)$$

$$z_2 = \ell_{\text{meas}}, \quad (8.13)$$

where p_{OLID_f} is the location of the laser beam endpoint represented in the global coordinate system, $\ell = \|\overrightarrow{\text{LID}_0 \text{LID}_f}\|$ is the modeled laser beam length, and ℓ_{meas} is the actual measured LIDAR distance.

3. During stance, the toe point coincides with the origin (active 200 ms after stance begins until toe-off)

$$h_3(x_t) = p_{OT}(x_t, \theta_k, \theta_a) \quad (8.14)$$

$$z_3 = [0 \ 0 \ 0]^T \quad (8.15)$$

where p_{OT} is the location of the toe in the inertial frame, and θ_k and θ_a are the measured knee and ankle angles.

The measurement noise for these observations is given by

$$R = \begin{bmatrix} \sigma_a^2 I_{3 \times 3} & 0 \\ 0 & \sigma_l^2 \end{bmatrix} \quad (8.16)$$

during swing and

$$R = \begin{bmatrix} \sigma_a^2 I_{3 \times 3} & 0 & 0 \\ 0 & \sigma_\ell^2 & 0 \\ 0 & 0 & \sigma_f^2 I_{3 \times 3} \end{bmatrix} \quad (8.17)$$

during stance. In these equations, σ_a^2 is the accelerometer variance, σ_ℓ^2 is the LIDAR measurement variance, and σ_f^2 is the foot position variance.

To further improve the EKF's state estimate, we enforce a number of constraints using the methods provided by Gupta and Hauser [2007]. Specifically, we enforce three equality constraints:

1. First, we require that the quaternion has unit norm

$$1 = q_1^2 + q_2^2 + q_3^2 + q_4^2. \quad (8.18)$$

2. Second, we prevent the yaw component of the orientation q from drifting. To do this, we convert the q to ZYX Euler angles and enforce $\phi_z = 0$,

$$0 = \text{atan2} \left(2(q_1 q_4 + q_2 q_3), 1 - 2(q_3^2 + q_4^2) \right). \quad (8.19)$$

3. Finally, during stance we further constrain the toe's x and y -coordinates to 0,

$$\begin{bmatrix} 0 \\ 0 \end{bmatrix} = \{p_{OT}(x_t, \theta_k, \theta_a)\}_{\text{rows 1 and 2}}. \quad (8.20)$$

In addition, we use inequality constraints to ensure the toe and heel do not penetrate the ground,

$$0 \leq \{p_{OT}(x_t, \theta_k, \theta_a)\}_{\text{row 3}}, \quad (8.21)$$

$$0 \leq \{p_{OL}(x_t, \theta_k, \theta_a)\}_{\text{row 3}}. \quad (8.22)$$

We enforce these constraints by solving the following quadratic program after each update step,

$$\hat{x}_{t|t}^{\text{proj}} = \underset{x}{\text{argmin}} \left(x - \hat{x}_{t|t} \right)^T \Sigma_{t|t}^{-1} \left(x - \hat{x}_{t|t} \right), \quad (8.23)$$

such that

$$A_{\text{eq}} x = b_{\text{eq}}, \quad (8.24)$$

$$A_{\text{ineq}} x = b_{\text{ineq}}, \quad (8.25)$$

where A_{eq} , b_{eq} , A_{ineq} , and b_{ineq} are derived from linearizing the equality and inequality constraints.

To identify the appropriate parameters of the Kalman filter, we collected ground truth training and testing kinematic data using a Vicon motion capture system and optimized the parameters of the EKF to minimize the error of the kinematic estimate. The parameters we optimized were the rotation of the LIDAR with respect to the hip,

the translation between the LIDAR and the IMU, and σ_ω , σ_a , σ_ℓ , and σ_f .

Figure 8.7 shows an example of the resulting EKF estimates of the hip, knee, ankle, heel, and toe positions during swing (blue stick figure and traces) compared to the ground truth obtained from the motion capture system (yellow) and an EKF estimate without the LIDAR sensor information integrated (red). Over the entire test data set, the root mean squared error of the estimated heel and toe positions during swing is 18.6 mm for the EKF with LIDAR information. In contrast, the EKF without LIDAR information has an error of 46.7 mm. Thus, including the LIDAR sensor data reduces the error by 60%.

8.6.2 Gaussian Process Hip Trajectory Prediction

To predict the future hip angle and height trajectories, we train sparse Gaussian process models using the FITC approximation [Snelson and Ghahramani, 2007]. The sparse approximation ensures the computational complexity at test time is independent of the training data set size, providing consistent real time performance. Throughout the swing phase, the learned hip angle and height distributions are conditioned on the swing trajectories completed so far to predict the distribution of the future trajectories for the rest of the swing (example shown in fig. 8.8). Our algorithm then uses the means of these conditional distributions in the motion planning phase (compare section 8.6.3).

For example, to calculate the conditional mean of future hip angles, we first compute the joint distribution of completed (θ_h^c) and future (θ_h^f) hip angles,

$$P(\theta_h^c, \theta_h^f) = \mathcal{N}(\mu_{\text{fitc}}, \Sigma_{\text{fitc}} + K(t_{\text{joint}}, t_{\text{joint}})) \quad (8.26)$$

$$= \mathcal{N}\left(\begin{bmatrix} \mu_c \\ \mu_f \end{bmatrix}, \begin{bmatrix} \Sigma_{c,c} & \Sigma_{c,f} \\ \Sigma_{f,c} & \Sigma_{f,f} \end{bmatrix}\right), \quad (8.27)$$

where μ_{fitc} and Σ_{fitc} are obtained from equation 11 in [Snelson and Ghahramani, 2007] and $K(t_{\text{joint}}, t_{\text{joint}})$ is an additional noise term given by a rational quadratic kernel [Rasmussen, 2004] that correlates the predicted angles across time, which results in smooth predicted trajectories. The mean of the conditional distribution $P(\theta_h^f | \theta_h^c)$ is then given by

$$\mu_f^{\text{cond}} = \mu_f + \Sigma_{f,c} \Sigma_{c,c}^{-1} (\mu_c - \theta_h^c). \quad (8.28)$$

As the inversion of $\Sigma_{c,c}$ is the most computationally expensive component of eq. (8.28), we use at most the last 10 hip angles and heights

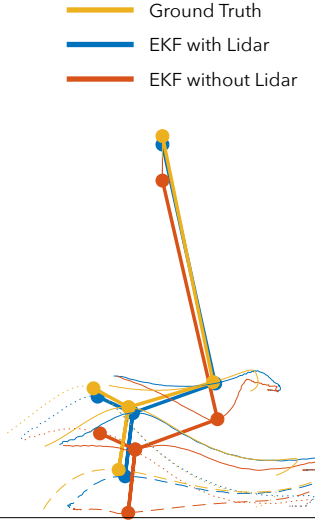


Figure 8.7: Trajectories of extended Kalman Filter (EKF) estimate of the position of the leg during swing (blue). Ground truth positions given by motion capture (yellow). EKF estimate without LIDAR information shown in red. Thick lines show the leg configuration at peak toe height during swing. Dotted lines indicate heel trajectories while dashed lines show the toe trajectories. Knee and ankle trajectories given by solid lines.

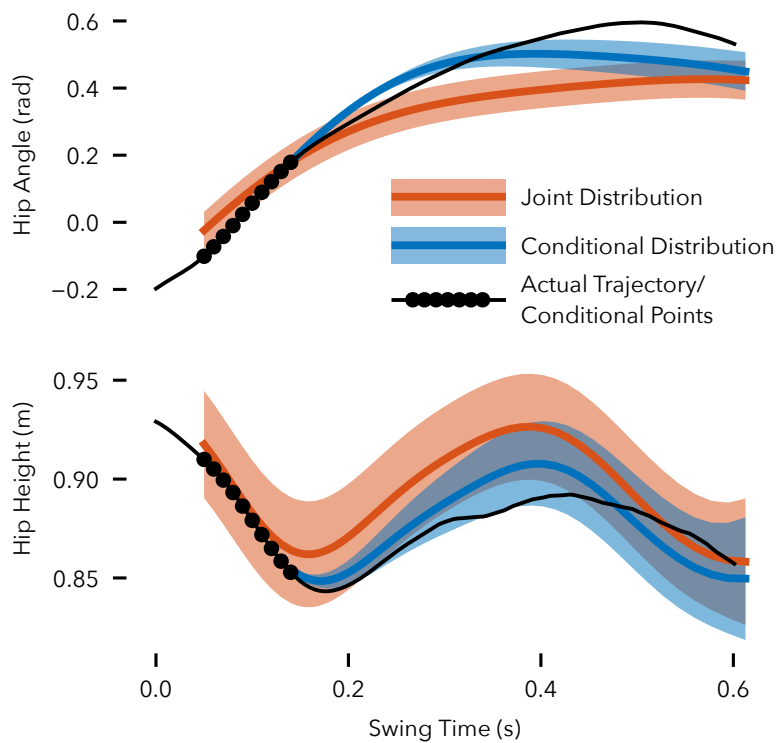


Figure 8.8: Example of hip angle and height trajectory predictions 0.15 s into swing. The prediction algorithm uses the previous 10 measured hip angles and heights (sampled at 100 Hz, black dots) along with the learned joint distributions of hip angles/heights versus time (red) to obtain the conditional distributions of future hip angles/heights (blue). The planning algorithm uses the means of the conditional distributions to generate knee and ankle trajectories. The actual hip height and angle trajectories are shown in black.

(sampled at 100 Hz) when calculating the conditional mean (compare fig. 8.8).

8.6.3 Trajectory Planning Quadratic Program Formulation

To obtain reactive control of the prosthesis swing leg motion, we plan future swing trajectories with a fast quadratic program (QP) operating at 100 Hz. The QP includes equality constraints, which ensure the trajectories progress smoothly from the current position to the desired end position, and inequality constraints, which avoid premature ground contact of toe and heel of the prosthesis. Because in our formulation the QP can only solve for one joint at a time, we first solve for the ankle trajectory assuming the knee trajectory found in the previous time step, and then use this updated ankle trajectory to solve for the new knee trajectory.

Figure 8.9 provides more details of the actions of the trajectory planner algorithm. For example, at a time of about 150 ms into the

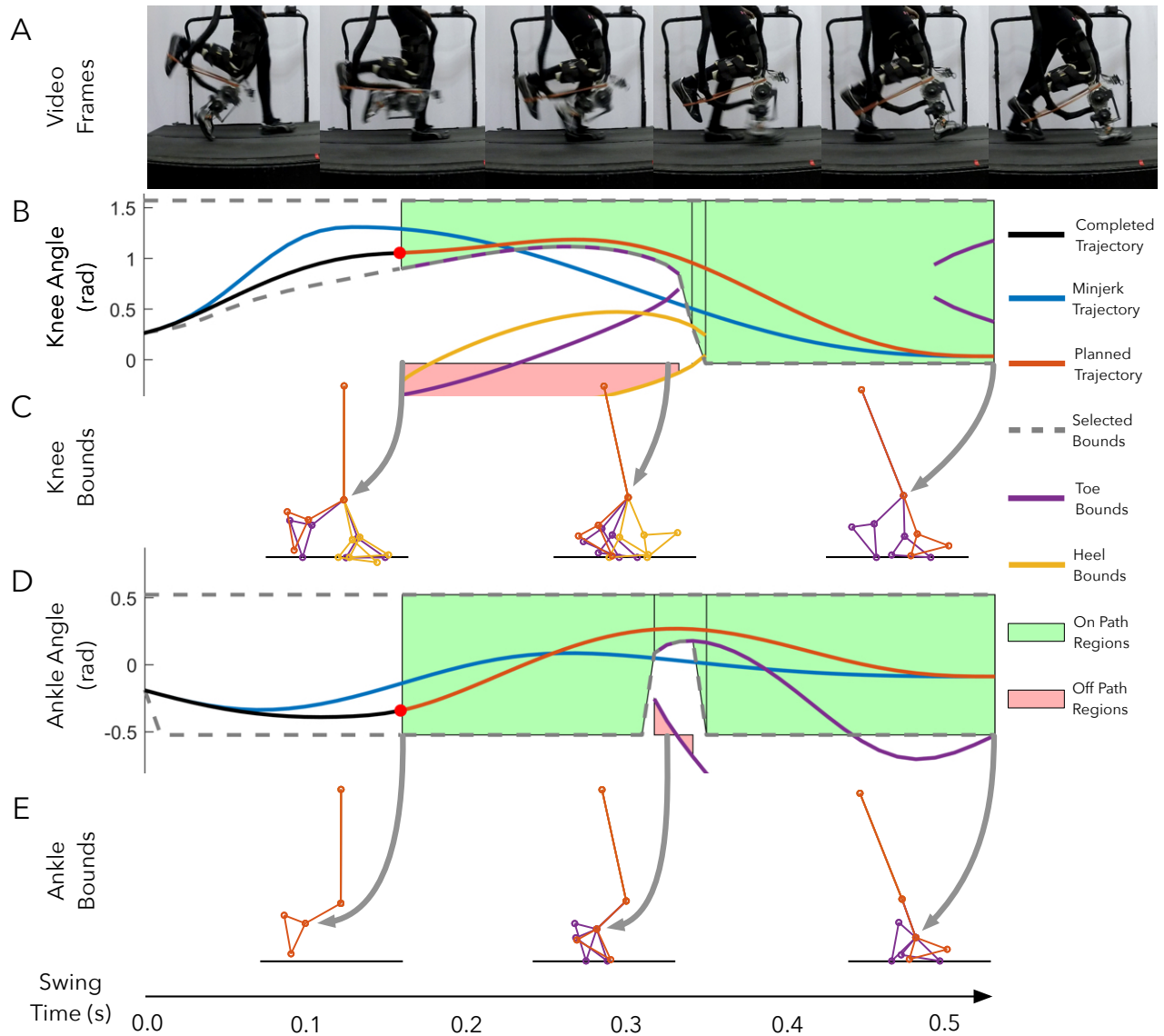


Figure 8.9: Planning Algorithm Steps: Panels B and D show the generated knee and ankle trajectories respectively. The planned trajectory (red) lies within the computed bounds (dashed gray). In contrast, standard minimum jerk trajectories (blue) do not respect the bounds, thereby increasing the tripping hazard. Panels C and E show examples of inverse kinematics (IK) solutions for toe (purple) and heel (yellow) contact for the knee and ankle joints respectively. We use the IK solutions to generate bounded regions that the planned trajectory can safely traverse. We consider ground contact constraints for only the first half of the remaining swing duration after which we only consider joint angle constraints. We use Dijkstra's algorithm to select regions (green) that allow a path from the start point to the desired final point. Bounded regions that do not lie on the path are shown in red. Panel A shows the corresponding prosthesis motion.

swing phase, the algorithm solves

$$\theta_k^{\text{toe bnd}} = \left\{ \theta_k : \{p_{OT}(\theta_h, z_h, \theta_k, \theta_a)\}_{\text{row 3}} = 0 \right\} \quad (8.29)$$

$$\theta_k^{\text{heel bnd}} = \left\{ \theta_k : \{p_{OL}(\theta_h, z_h, \theta_k, \theta_a)\}_{\text{row 3}} = 0 \right\} \quad (8.30)$$

at a set of sample times spanning the remaining swing trajectory to obtain a planned knee trajectory (red trace in fig. 8.9B). Figures fig. 8.9C and E show the predicted inverse kinematics (IK) solutions at characteristic points into the swing for the knee and ankle respectively, with solutions leading to toe contact shown in purple and solutions leading to heel contact shown in yellow. For each contact point, there are typically two solutions, one lower bound, for which the joint angle cannot cross from above, and one upper bound, for which the joint angle cannot cross from below.

Often, the valid leg configurations span disjointed regions in the configuration space (green and red regions in fig. 8.9B and D). Therefore, the planner next identifies a valid sequence of regions for the trajectory to traverse in a four step procedure. First, the planner identifies critical points along the predicted trajectory at which any bound activates or deactivates. Second, at each critical point, the planner sorts the bound angles from largest to smallest and iterates through them to define regions between successive upper and lower bounds. Third, the planner defines a graph over the regions with edge weights equal to the average squared angle minus the volume of the child region. This cost favors a sequence of regions that are large and thus safe to travel through and avoids regions that require excessive joint flexion or extension. Dijkstra's algorithm is then used to find a valid sequence of regions that minimizes this cost [Dijkstra, 1959]. Finally, so that the generated trajectories do not get too close to the identified bounds, a buffer is added to the bounds. This buffer takes the form

$$\theta_{\text{buf}} = \theta_{\text{buf}}^0 \sin \left(\pi \frac{t - t_0}{t_f - t_0} \right), \quad (8.31)$$

where θ_{buf}^0 is either 5° or -5° for lower and upper bounds respectively, t is the future swing time, and t_0 and t_f are the current and final swing times.

After identifying the bounded regions, the planner generates the trajectory for a specific joint by solving a quadratic program. The trajectory of each joint is represented by three, fifth-order polynomial

splines,

$$\theta_1(t) = a_{01} + a_{11}t + \dots + a_{51}t^5 = [1 \ t \ \dots \ t^5]a_1 \quad (8.32)$$

$$T_0 \leq t < T_1 \quad (8.33)$$

⋮

$$\theta_3(t) = a_{03} + a_{13}t + \dots + a_{53}t^5 = [1 \ t \ \dots \ t^5]a_3 \quad (8.34)$$

$$T_2 \leq t < T_F, \quad (8.35)$$

and solved for by the following QP,

$$a^* = \underset{a}{\operatorname{argmin}} \frac{1}{2} a^T (H_\theta + w H_{\ddot{\theta}}) a, \quad (8.36)$$

where $a = [a_1^T \ a_2^T \ a_3^T]^T$, H_θ and $H_{\ddot{\theta}}$ encode quadratic costs on angle and jerk respectively, and w is a weight parameter. The solution is subject to the inequality constraints

$$\theta(t) \leq \theta_{\max}(t), \forall t \quad (8.37)$$

$$\theta(t) \geq \theta_{\min}(t), \forall t \quad (8.38)$$

$$\dot{\theta}(t) \leq \dot{\theta}_{\max}, \forall t \quad (8.39)$$

$$\dot{\theta}(t) \geq \dot{\theta}_{\min}, \forall t, \quad (8.40)$$

which ensure the trajectory lies within the identified bounds and respects velocity limits, and to the equality constraints

$$\theta(T_0) = \theta_0 \quad (8.41)$$

$$\dot{\theta}(T_0) = \dot{\theta}_0 \quad (8.42)$$

$$\ddot{\theta}(T_0) = \ddot{\theta}_0 \quad (8.43)$$

$$\theta(T_F) = \theta_F \quad (8.44)$$

$$\dot{\theta}(T_F) = 0 \quad (8.45)$$

$$\ddot{\theta}(T_F) = 0 \quad (8.46)$$

$$\theta_1(T_1) = \theta_2(T_1) \quad (8.47)$$

$$\dot{\theta}_1(T_1) = \dot{\theta}_2(T_1) \quad (8.48)$$

$$\ddot{\theta}_1(T_1) = \ddot{\theta}_2(T_1) \quad (8.49)$$

⋮

which ensure the trajectory starts at the current and terminates at the desired positions, velocities, and accelerations and that the splines join together smoothly. If the QP fails to find a trajectory that can satisfy the constraints, the last found valid trajectory is reused for the next time step. In addition, at the first iteration, the ankle trajectory planner uses the output of the minimum jerk trajectory planner to solve the inverse kinematics for the bounds.

8.6.4 Experimental Procedure

We tested the ability of the proposed trip avoidance control to reduce the incidence and severity of trips while walking with the powered transfemoral prosthesis shown in fig. 8.6 To evaluate the performance of the system, an able-bodied user walked with the prosthesis while attempting to elicit trips by lowering the hip in swing. During the stance phase, the prosthesis randomly decided to either use the proposed swing control or to use standard minimum jerk trajectories that do not consider the tripping hazard. The user was not aware of which controller would be used in the upcoming swing. The user completed a total of ten one minute walking trials.

We examined several outcomes for evaluating the control performance. First, we examined the distribution of knee angles at the beginning of stance. Large knee angles at the beginning of stance indicate premature landing due to toe-strike instead of heel strike. Ideally, the landing angle is close to the desired final angle of 2 degrees. Second, we checked the integral of the ground reaction force during swing. If this quantity is large, it indicates scuffing of the toe on the ground. Finally, we examined the relationship between the hip and toe heights during swing. If our controller is working as intended, the toe height during swing should have a decreased sensitivity to the hip height.

8.7 Planning Approach Results

Figure 8.10 shows the knee and ankle swing trajectories generated by the proposed control (blue) and by a standard jerk minimization control (red) during normal walking and trip elicitation. During undisturbed walking, the trajectories produced by both control strategies are similar. However, the proposed control strategy has a tendency to keep the knee flexed for longer and then extends it faster towards the end of swing. In addition, in a few steps, the proposed controller flexed the ankle significantly more than did the standard minimum jerk control. These trends are exaggerated during trip elicitation. There are more knee trajectories in which the knee stays flexed for longer, thereby creating more ground clearance. In addition, the ankle flexes earlier, which will help to create more foot clearance when the hip is suddenly lowered in early swing.

We used video and audio recordings of the trials, as well as data from the prosthesis, to manually classify trips as those swing trajectories that end with toe strike or during which the foot scuffed on the ground. We find that over the ten minutes of walking, the minimum jerk control produced 109 trips while the proposed approach

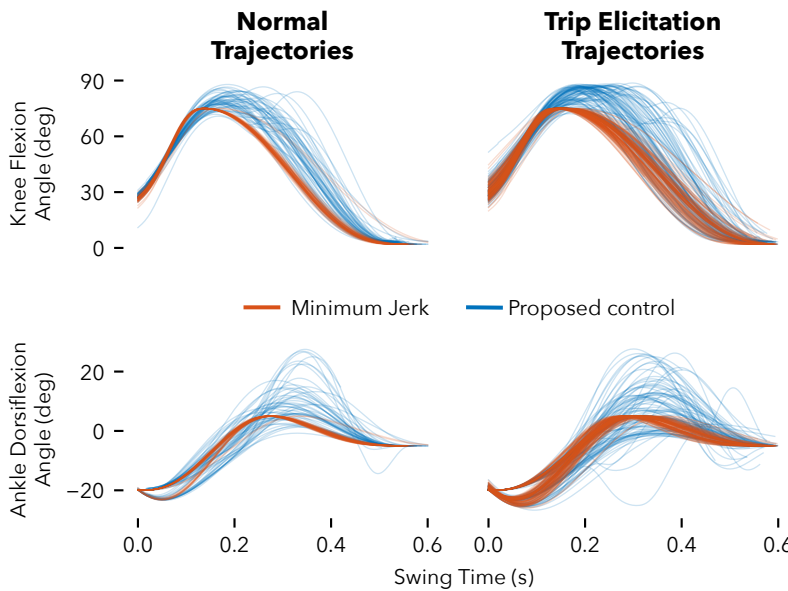


Figure 8.10: Knee and ankle trajectories produced during normal walking and while eliciting trips. To avoid tripping during trip elicitation trials, trajectories generated by the proposed approach often flex the knee to a greater degree and for longer before quickly extending at the end of swing. At the ankle joint we see overall greater variability in the generated trajectories during the trip elicitation condition versus normal walking.

produced 35 trips, reducing the trip rate by 68%.

To further examine the performance of the two control strategies, we used kernel density estimates of the landing knee flexion angle, a measure of the propensity for tripping, and integrated ground reaction force (GRF) during swing, a measure of the propensity for foot scuffing. Figure 8.11 shows the distributions of the landing angle of the prosthesis at the end of swing for the proposed swing control (blue) and for the standard minimum jerk swing control (red) during the trip elicitation condition. We observe the minimum jerk control is much more likely to generate a swing trajectory that ends prematurely with a large knee flexion angle, which is indicative of toe contact instead of heel contact at the end of swing. The distributions of the integrated GRFs suggests the minimum jerk control produced a larger percentage of swings with high ground reaction forces than the proposed control, indicating an increased frequency and severity of toe scuffing during swing (fig. 8.12).

We can also ask the question, “For steps during which the prosthesis used trajectories generated by the proposed control, would the user have tripped had the prosthesis used a minimum jerk trajectory?” To answer this question, we can use the kinematics model shown in fig. 8.6 along with ground truth hip height and hip angle data captured via a motion capture system, to estimate the location of the toe had the knee and ankle perfectly followed the desired trajectories produced by each control scheme. This analysis predicts that

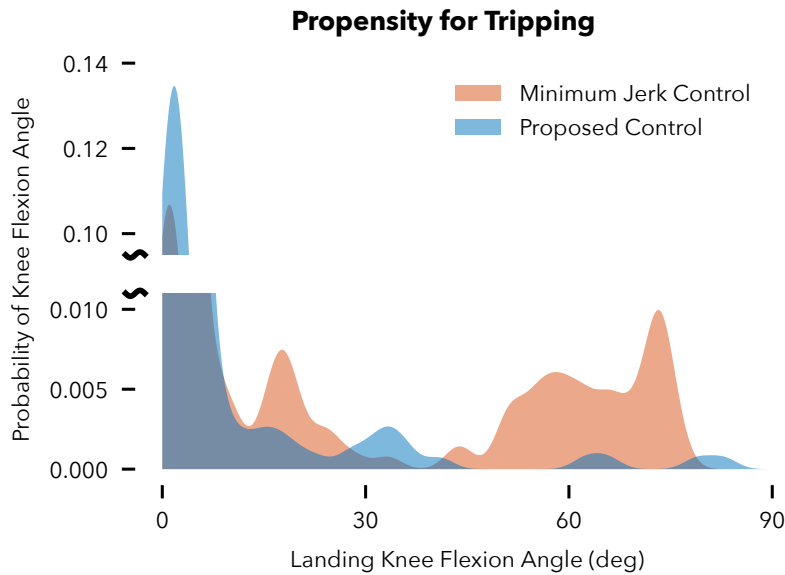


Figure 8.11: Kernel density estimate of the probability of various landing knee flexion angles with the proposed swing control (blue) and standard min-jerk swing control (red). Large landing knee angles indicate premature toe contact during swing.

the prosthesis would have tripped or scuffed the toe on the ground during 22% of the steps if we had used the minimum jerk trajectory. In contrast, it predicts a trip or scuff rate of 5% had we perfectly followed the trajectories generated by the proposed control.

Finally, fig. 8.13 shows the relationship between the average toe and hip heights during swing for both control schemes. The toe height of the prosthesis when controlled by the proposed control is less sensitive to decreases in the hip height than it is when using the standard minimum jerk control.

8.8 Planning Approach Discussion

We presented initial work toward a real-time reactive control of powered prostheses to help amputees avoid tripping in the swing phase of gait. At any time during swing, the proposed control uses a laser range finder and an inertial measurement unit to estimate the current pose of the prosthesis, predicts the future hip angle and height based on trained Gaussian process models, and then plans new knee and ankle joint trajectories that ensure neither the toe nor heel contacts the ground prematurely. Our results indicate the proposed control approach can substantially reduce the incidence of trips and reduce the severity and frequency of toe scuffing.

To the best of our knowledge, this work is the first demonstration of lower limb prosthetic control that integrates perception feedback

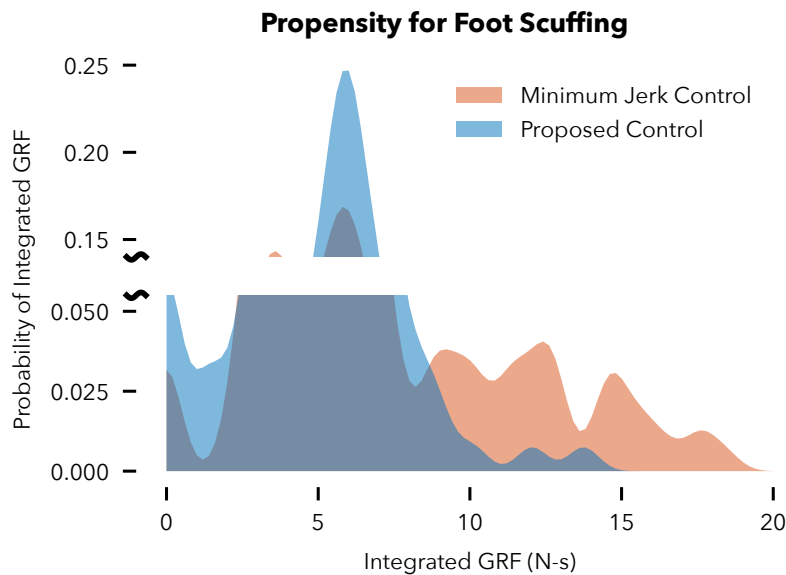


Figure 8.12: Kernel density estimate of the probability of various integrated ground reaction force values for the proposed swing control (blue) and standard min-jerk swing control (red). Large integrated GRF during the swing phase is indicative of the toe scuffing on the ground.

in real-time and that proactively ameliorates the falling hazard amputees face. Previous research in this area has largely focused on detecting stumbles *after* they have occurred. For example, Lawson et al. [2010] and Shirota et al. [2014] have proposed classifiers that can detect trips during swing and predict whether a lower or raising strategy should be used in response. Similarly, Zhang et al. [2011a] have proposed a method that can detect stumbles and classify them as trips during swing or slips during stance. However, these previous studies have not proposed concrete control actions to preempt stumbles or to properly react in the event that a stumble is detected. Our results motivate further research into such proactive and reactive approaches, closing the perception-action loop for improving gait robustness with robotic prostheses.

Several avenues for future work exist. First, in our current study only one able-bodied user tested the proposed control. Further experiments with amputee subjects are needed to verify the system provides benefits to this population. For instance, amputees accustomed to walking with passive prostheses show significantly altered hip kinematics [Jaegers et al., 1995], which could affect the control behavior. However, the proposed control should be able to properly adapt to these behavior differences, as the Gaussian process models are trained for specific users. Second, although trips during swing are one of the most common failure modes we encounter with our powered prostheses, these events are still rare and many hours of

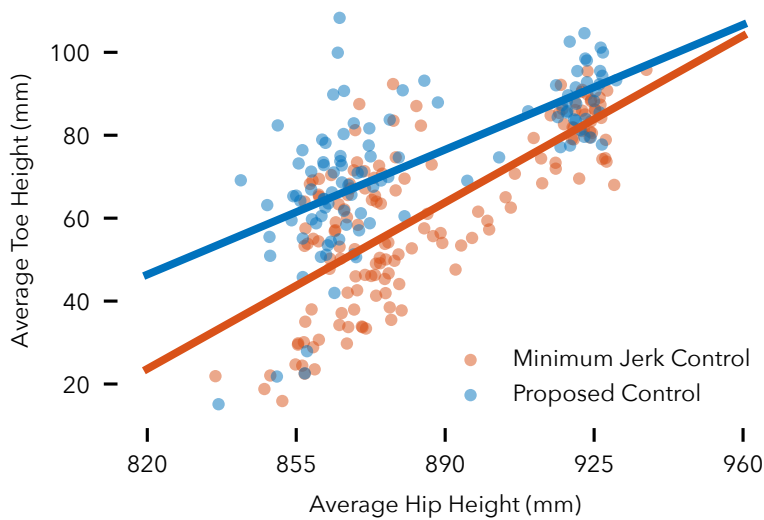


Figure 8.13: Average toe height vs average hip height for the proposed swing control (blue) and standard min-jerk swing control (red). The toe height during swing is less sensitive to the hip height when using the proposed swing control than when using the min-jerk swing control.

normal walking are required to observe a sufficient number of trips and compare controllers. As a result, we actively induced trips by sudden drops in hip height during swing, which does not exactly reflect the situations in which trips occur. Specifically, trips can happen due to subtle changes in leg kinematics, and it remains to be seen in experiments if our approach can avoid trips in these more subtle situations.

At the implementation level, there is also room for further exploration. To keep the computational costs low, and due to ease of implementation in the prosthesis' Simulink Real-Time™ environment, we plan trajectories using quadratic programs that iterate between finding solutions for the ankle and knee joints. While this iterative approach is fast when compared to trajectory optimization methods that deal with multiple joints simultaneously, the iterations occasionally get stuck when the planner for one joint trajectory cannot find a solution based on the assumed fixed trajectory of the other joint. Moreover, if a solution cannot be found, the current approach simply reuses the last identified trajectory, rather than moving the trajectory to be more safe, even if it cannot fully satisfy the bounds. It seems worthwhile to investigate whether non-convex trajectory optimization methods such as CHOMP [Ratliff et al., 2009], in which the bounds are represented as soft rather than hard constraints, can help solve for the knee and ankle trajectories simultaneously without sacrificing computational speed.

In addition, several technical simplifications can be considered

to bring this technology closer to commercialization. We used an accurate and expensive laser distance sensor, eyeing future research in obstacle scanning and avoidance capabilities. However, for simple ground plane avoidance, inexpensive infrared distance sensors such as those used by Scandaroli et al. [2009] are likely sufficient. It may also be possible to simplify the trajectory planning phase by, for example, forgoing formal guarantees on satisfying bounds and instead relying on heuristics to increase knee and ankle flexion and adjust timing in response to decreased hip height during swing.

9

Robust and Adaptive Stance Control via Extended Kalman Filter-based Phase Estimation

Material in this section based on Thatte et al. [2019]¹

9.1 Introduction

In chapter 7 we compared the neuromuscular and impedance controllers. The results showed that there were reasons for falls with the impedance controller that did not occur with neuromuscular control. Chief among the types of falls that occurred with impedance control were knee collapses caused by premature transitions to the third phase of stance and swing trips, which were often preceded by a missed transition to the third phase of stance. In contrast, the neuromuscular control did not suffer from this issue, likely due to its smooth torque output.

In the neuromuscular controller, the phase of gait is implicitly captured in the muscle states that emerge from the interplay between multi-segment limb dynamics, muscle dynamics, and reflexes. A downside to this approach, however, is that it relies on many parameters that may be difficult to tune, thus limiting clinical applicability. An alternative approach to achieving smooth phase estimation during stance is the controller proposed by Quintero et al. [2016]. This controller explicitly derives a continuous phase estimate by comparing the hip angle to its integral. However, as we show in section 9.2 this approach may be sensitive to step-to-step changes in gait due as it relies on the integral of the hip angle over a gait cycle. Recently, Rezazadeh et al. [2018] eliminated the reliance on the hip integral by re-introducing discrete state transitions based on thigh angle and velocity thresholds. However, this approach could face similar robustness issues as the previously described finite-state impedance control.

¹ Nitish Thatte, Nandagopal Srinivasan, and Hartmut Geyer. Real-time reactive trip avoidance for powered transfemoral prostheses. In *Proceedings of Robotics: Science and Systems*, 2019

Therefore, in this chapter, we propose a new control strategy for lower limb prostheses that is built on a robust and smooth estimate of the phase of gait and parameterizes the control outputs in an interpretable manner. We start by presenting our attempt at implementing the phase-based controller proposed by Quintero et al. [2016] (section 9.2). In section 9.3, we present an Extended Kalman Filter (EKF) that estimates the phase and its rate of change during the stance portion of gait based on a multitude of sensor measurements. We then use sparse Gaussian Process (GP) observation models to learn relationships between phase and sensor measurements for specific users and to choose the appropriate control actions for the prosthesis. In section 9.4, we evaluate the performance of the proposed controller with experiments on able-bodied subjects and a single amputee subject. Finally, in section 9.5 we discuss the results and highlight potential limitations of this study as well as avenues for future research.

9.2 Phase Based Control Implementation

In the experiment presented in this chapter 7, we compared neuromuscular control to the commonly used impedance control strategy. Our original intent, however, was to also compare both controllers to the continuous phase-based controller proposed by Quintero et al. [2016], which we described briefly in section 2.2. Here we show the results obtained with an implementation of this controller on our prosthesis.

In this control strategy the desired knee and ankle angles are parameterized with respect to a continuous phase variable, which should increase monotonically from zero at heel strike to one at the next heelstrike. To estimate phase, we draw phase portrait by plotting the hip angle $\phi(t)$ on the x -axis and integral of hip angle over a step $\Phi(t)$ on the y -axis. The phase angle is then computed as

$$v(t) = \text{atan2}(-z(\Phi(t) + \Gamma), -(\phi(t) + \gamma)), \quad (9.1)$$

where Γ , and γ are shift parameters that center the phase portrait about the origin, and z is a scaling parameter that makes the phase portrait circular. Specifically,

$$z = \frac{\phi_{\max} - \phi_{\min}}{\Phi_{\max} - \Phi_{\min}} \quad (9.2)$$

$$\gamma = -\frac{1}{2}(\phi_{\max} + \phi_{\min}) \quad (9.3)$$

$$\Gamma = -\frac{1}{2}(\Phi_{\max} + \Phi_{\min}) \quad (9.4)$$

where ϕ_{\max} , ϕ_{\min} , Φ_{\max} , Φ_{\min} are the estimated max and min hip angle and hip angle integral over the past few gait strides. In our implementation, we used the median max/min hip angle/angle integral over the past five steps to estimate these values. To avoid discontinuities in the phase angle estimate, the max/min hip angle terms are only allowed to update when the phase angle crosses 0° or 180° while the max/min hip angle integral terms are only allowed to update when the phase angle crosses 90° or 270° .

In addition to estimating the above parameters, we must also estimate the average hip angle over a stride. This is because in order for the hip angle to integrate to zero, its average must be zero as well. The hip angle integral term is then computed as the integral of hip angle minus its average

$$\Phi(t) = \int_0^t (\phi(\tau) - \mu_\phi) d\tau. \quad (9.5)$$

For the average hip angle over a stride, μ_ϕ we use the median value over the last five strides.

Figure 9.1 shows an example phase portrait from an eight second walking bout. From this figure, we see that towards the latter end of the trial, the integral term tends to drift towards the end of stance before being reset to zero at heel strike. These irregularities step from the sensitivity of the integral term to the hip angle trajectory and cause the phase angle to trace form a nonlinear curve in time.

Therefore, to prevent excessively unnatural phase trajectories, we also implemented time based upper and lower bounding of the phase. In this scheme, the normalized phase,

$$\bar{v}(t) = \frac{v(t) - v(0)}{2\pi}, \quad (9.6)$$

is lower and upper bound by third order polynomial functions of time. The lower bound polynomial intersects three points: $\phi(t = 0) = 0$, $\phi(t = T/2) = 1/4$ and $\phi(t = T) = 1$ while the upper bound polynomial intersects: $\phi(t = 0) = 0$, $\phi(t = T/2) = 3/4$ and $\phi(t = T) = 1$. The stride duration T was estimated as the median of the last five steps. Finally, the constrained phase variable estimate was low pass filtered by a 2nd order Butterworth filter with a cut off frequency of 10 Hz.

The phase estimate was used to look up the desired knee and ankle angles. PID control was then used to calculate the desired torque for the actuators which was then achieved by the low level torque control (section 3.2).

Row 1 of fig. 9.2 shows the unconstrained and constrained phase estimates in blue and purple respectively and the lower and upper bounds in black. The phase estimate only remained within the

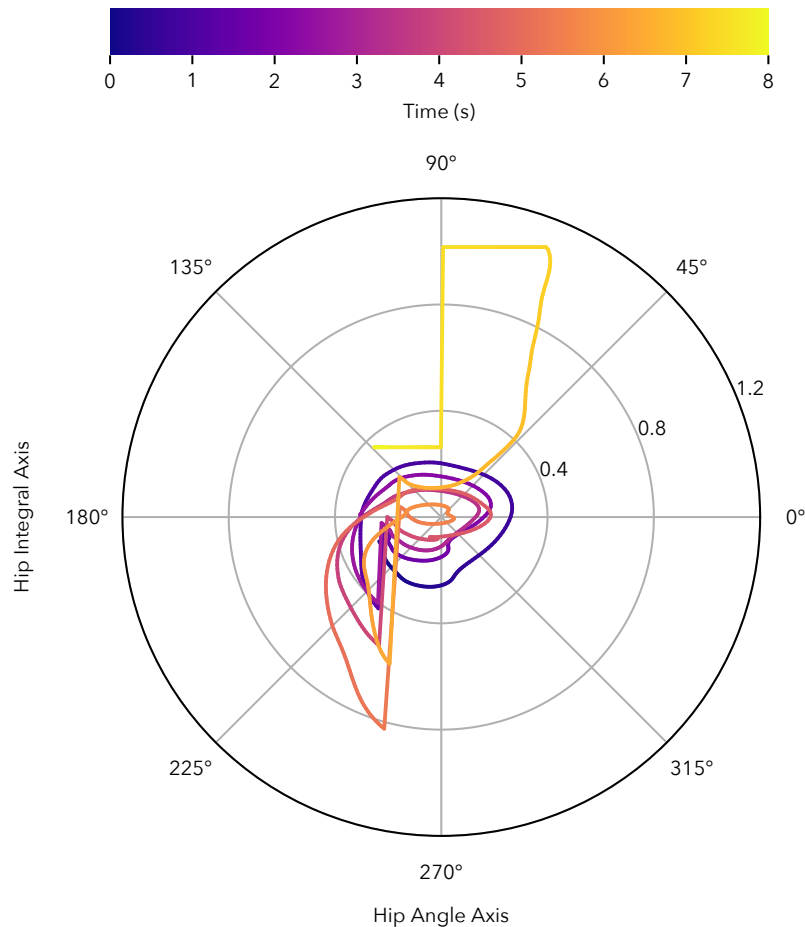
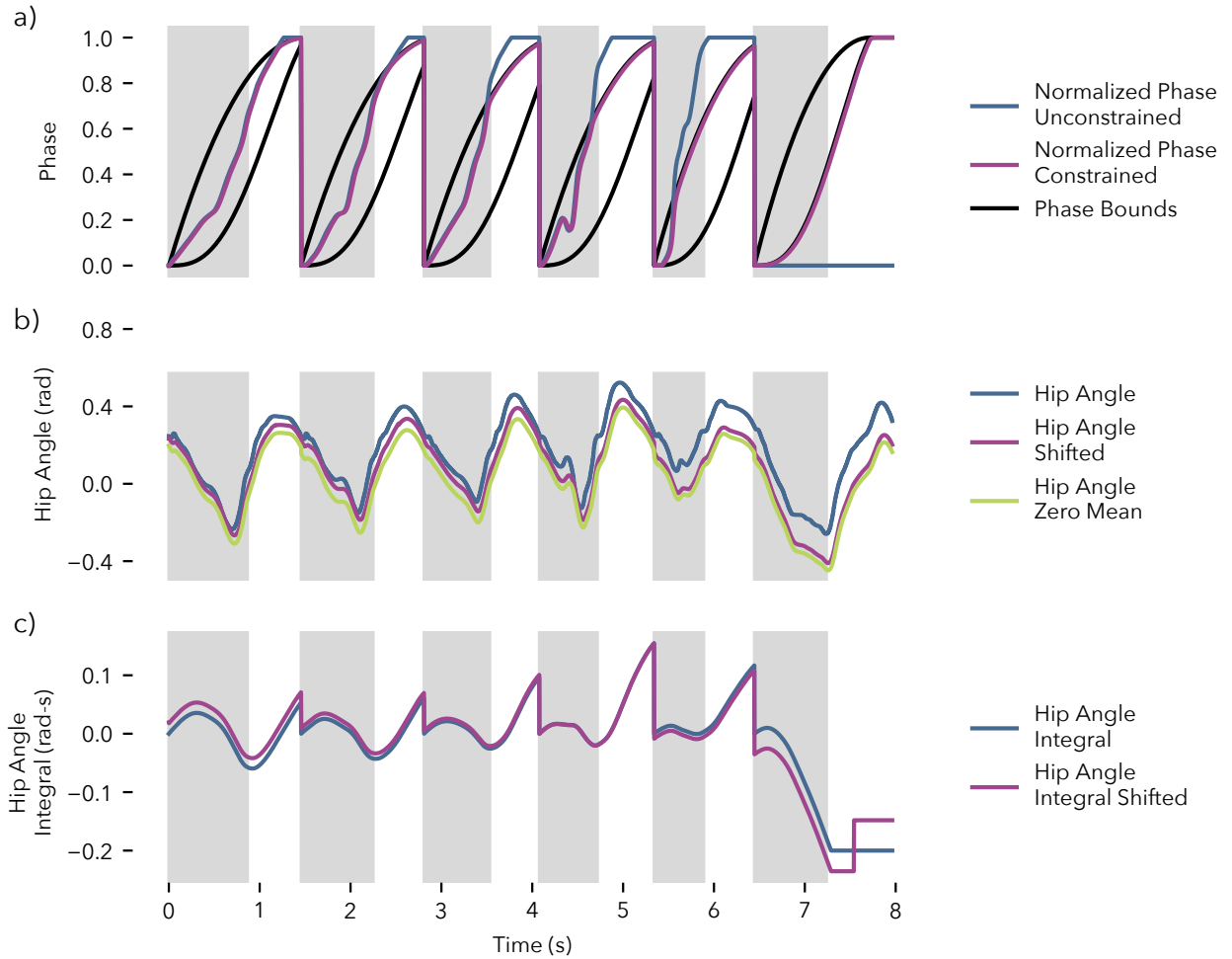


Figure 9.1: Phase angle over eight seconds of walking. Drift in the integral term caused irregularities in the phase angle plot.

bounds for the first step. After that, the phase estimate needed to be constrained by the upper bound earlier and earlier in each step.

The hip angle plot in the second row, shows there is significant variability in the hip angle trajectory from step to step. Consequently, the hip angle integral (row 3) does not reach zero at the beginning of each stance (stance phase designated by grey shaded regions). The drift in the integral term occurs despite updates to the shifted hip angle (purple row 2) and zero-mean hip angle (green row 2).

The resultant control action on the prosthesis, seemed to drive a positive feedback loop wherein increased phase angle in late stance drives knee flexion and ankle push off leading into swing. Increased knee flexion torque and ankle plantarflexion also flex the hip more, which further drives the phase estimate forward. Consequently, the gait was driven faster and faster, as shown by decreasing duration of stance (grey shaded regions). Also, a potential contributor to this



positive feedback loop was an over-reliance on integral action in the ankle, which is slow to build up the required plantarflexion torque; a feedforward torque term might be helpful for generating torque as a function of phase. The changing duration of stance also caused variation in hip integral leading to more gait instability. Due to these issues, we were not able to achieve hands free-walking for any duration of time, and only managed walking with hand rail support for a few seconds at a time.

While these problems could be rectified with tighter bounds on the phase, this would make the controller closer to a time-based strategy, which would make volitional control impossible. Therefore, in the following sections we propose using a more established method of state estimation, an extended Kalman filter, to estimate the phase during gait. Using a Kalman allows us to specify dynamics for the

Figure 9.2: Results from test of unified phase variable controller. Step to step variability causes significant divergence in the integral term, leading to an unstable phase estimate.

phase, which help keep its trajectory smooth. Furthermore, it allows us to incorporate information from more than two sources, while considering the intrinsic variation of each signal.

9.3 Methods

The proposed prosthesis controller consists of two components. The first is an Extended Kalman Filter (EKF) that estimates the gait phase, defined as the percent of stance completed so far (section 9.3.1). Ideally, the phase estimate starts at zero at heel strike and reaches one precisely at toe-off. The second component is a set of control surfaces, which are functions of phase and phase velocity, that provide desired knee and ankle angles, velocities, and feed forward torques for generating the prosthesis stance behavior (section 9.3.2).

9.3.1 GP-EKF for estimating phase

In contrast to the previously described phase variable approach for phase estimation in prostheses [Quintero et al., 2016], which uses a single source of information, we take a sensor-fusion approach and combine angle and velocity information from the hip, knee, and ankle joints of the prosthetic limb. An IMU mounted to the thigh portion of our powered knee-and-ankle prosthesis provides information about the user’s hip motion, and encoders on the prosthesis provide information about the knee and ankle joints. We use these observations in an Extended Kalman filter (EKF) to estimate the phase and phase velocity during stance. The EKF assumes the linear, discrete time phase dynamics

$$\begin{aligned} x_t = \begin{bmatrix} \phi_t \\ \dot{\phi}_t \end{bmatrix} &= \begin{bmatrix} 1 & \Delta t \\ 0 & 1 \end{bmatrix} \begin{bmatrix} \phi_{t-1} \\ \dot{\phi}_{t-1} \end{bmatrix} + w_t \\ &= Ax_{t-1}, \end{aligned} \quad (9.7)$$

where ϕ is the phase, $\dot{\phi}$ is the rate of change of phase, Δt is the integration time step and $w_t \sim \mathcal{N}(0, Q)$. We set

$$Q = \begin{bmatrix} 0 & 0 \\ 0 & \sigma_\phi^2 \end{bmatrix}, \quad (9.8)$$

with $\sigma_\phi^2 = 1e-7$. These dynamics encode the assumption that phase should evolve continuously, at a roughly constant rate.

Observations of the prosthesis-side hip, knee, and ankle angles and velocities inform the evolution of the above dynamics. For the joint angles, the observation models are of the form

$$z_t^{\theta_j} = h^{\theta_j}(x_t) + v_t^{\theta_j} = \text{GP}_{\mu}^{\theta_j}(\phi_t) + v_t^{\theta_j}, \quad (9.9)$$

where $\text{GP}_{\mu}^{\theta_j}$ is the mean of a learned Gaussian Process (GP) model of the angle of joint j as a function of the phase ϕ and $v_t^{\theta_j} \sim \mathcal{N}(0, \text{GP}_{\sigma^2}^{\theta_j}(\phi_t))$.

Here, $\text{GP}_{\sigma^2}^{\theta_j}$ is the variance of the same learned GP model.

Similarly, for the joint velocities we use an observation model of the form

$$\begin{aligned} z_t^{d\theta_j/d\phi} &= h^{d\theta_j/d\phi}(x_t) + v_t^{d\theta_j/d\phi} \dot{\phi}_t \\ &= \left(\text{GP}_{\mu}^{d\theta_j/d\phi}(\phi_t) + v_t^{d\theta_j/d\phi} \right) \dot{\phi}_t \end{aligned} \quad (9.10)$$

where $\text{GP}_{\mu}^{d\theta_j/d\phi}$ is the mean of a Gaussian Process model of the velocity of joint j (in units of $d\theta_j/d\phi$) as a function of ϕ . In addition, $v_t^{d\theta_j/d\phi} \sim \mathcal{N}(0, \text{GP}_{\sigma^2}^{d\theta_j/d\phi}(\phi_t))$, where $\text{GP}_{\sigma^2}^{d\theta_j/d\phi}$ is the variance of the same learned GP model for joint velocity.

To train the GP observation models, the algorithm maintains a training data set of stance gait data. The training data set includes the joint angles and velocities (in units of $d\theta_j/d\phi$) sampled at 100 Hz as well as the actual corresponding phases and phase velocities during stance. We assume that, in hindsight, the actual phase increased linearly from zero at heel strike to one at toe off and that the actual phase velocity was constant during stance and equal to $1/T_n$, where T_n is the duration of the completed stance phase. We retrain the GP models using this gait data after every five completed steps. To ensure that the test-time performance of the Gaussian Process models does not degrade as more training data accumulates, we employ the fully independent training conditional (FITC) approximation of the GP [Snelson and Ghahramani, 2007]. This approximation represents the GP using a fixed-size active set of training points. We use 25 points in our approximation.

With the learned GP observation models, we follow the GP-EKF procedure proposed by Ko and Fox [2009] to obtain an estimate of phase and phase velocity. In this procedure, we first *predict* the next state distribution by propagating the mean $\hat{x}_{t-1|t-1}$ and covariance $\Sigma_{t-1|t-1}$ of the state using the dynamics model provided by eq. (9.7),

$$\hat{x}_{t|t-1} = A\hat{x}_{t-1|t-1} \quad (9.11)$$

$$\Sigma_{t|t-1} = A\Sigma_{t-1|t-1}A^T + Q. \quad (9.12)$$

Next, we *update* the state distribution estimate given measurements z_t of the joint angles and velocities using the following equations and

the GP observation models $h_t(x_t)$.

$$K_t = \Sigma_{t|t-1} H_t^T \left(H_t \Sigma_{t|t-1} H_t^T + M_t R M_t^T \right)^{-1} \quad (9.13)$$

$$\hat{x}_{t|t} = \hat{x}_{t|t-1} + K_t \left(z_t - h(\hat{x}_{t|t-1}) \right) \quad (9.14)$$

$$\Sigma_{t|t} = (I - K_t H_t) \Sigma_{t|t-1} \quad (9.15)$$

where,

$$h(x_t) = \begin{bmatrix} \text{GP}_\mu^{\theta_h}(\phi_t) \\ \text{GP}_\mu^{\theta_k}(\phi_t) \\ \text{GP}_\mu^{\theta_a}(\phi_t) \\ \text{GP}_\mu^{d\theta_h/d\phi}(\phi_t)\dot{\phi}_t \\ \text{GP}_\mu^{d\theta_k/d\phi}(\phi_t)\dot{\phi}_t \\ \text{GP}_\mu^{d\theta_a/d\phi}(\phi_t)\dot{\phi}_t \end{bmatrix} \quad (9.16)$$

$$H_t = \frac{\partial h}{\partial x} \Big|_{\hat{x}_{t|t-1}} = \begin{bmatrix} \frac{\partial \text{GP}_\mu^{\theta_h}}{\partial \phi_t} \Big|_{\phi_t} & 0 \\ \frac{\partial \text{GP}_\mu^{\theta_k}}{\partial \phi_t} \Big|_{\phi_t} & 0 \\ \frac{\partial \text{GP}_\mu^{\theta_a}}{\partial \phi_t} \Big|_{\phi_t} & 0 \\ \frac{\partial \text{GP}_\mu^{d\theta_h/d\phi}}{\partial \phi_t} \Big|_{\phi_t} & \text{GP}_\mu^{d\theta_h/d\phi} \\ \frac{\partial \text{GP}_\mu^{d\theta_k/d\phi}}{\partial \phi_t} \Big|_{\phi_t} & \text{GP}_\mu^{d\theta_k/d\phi} \\ \frac{\partial \text{GP}_\mu^{d\theta_a/d\phi}}{\partial \phi_t} \Big|_{\phi_t} & \text{GP}_\mu^{d\theta_a/d\phi} \end{bmatrix} \quad (9.17)$$

$$M_t = \frac{\partial h}{\partial v_t} \Big|_{\hat{x}_{t|t-1}} = \begin{bmatrix} I_{3 \times 3} & 0 \\ 0 & \dot{\phi}_t I_{3 \times 3} \end{bmatrix} \quad (9.18)$$

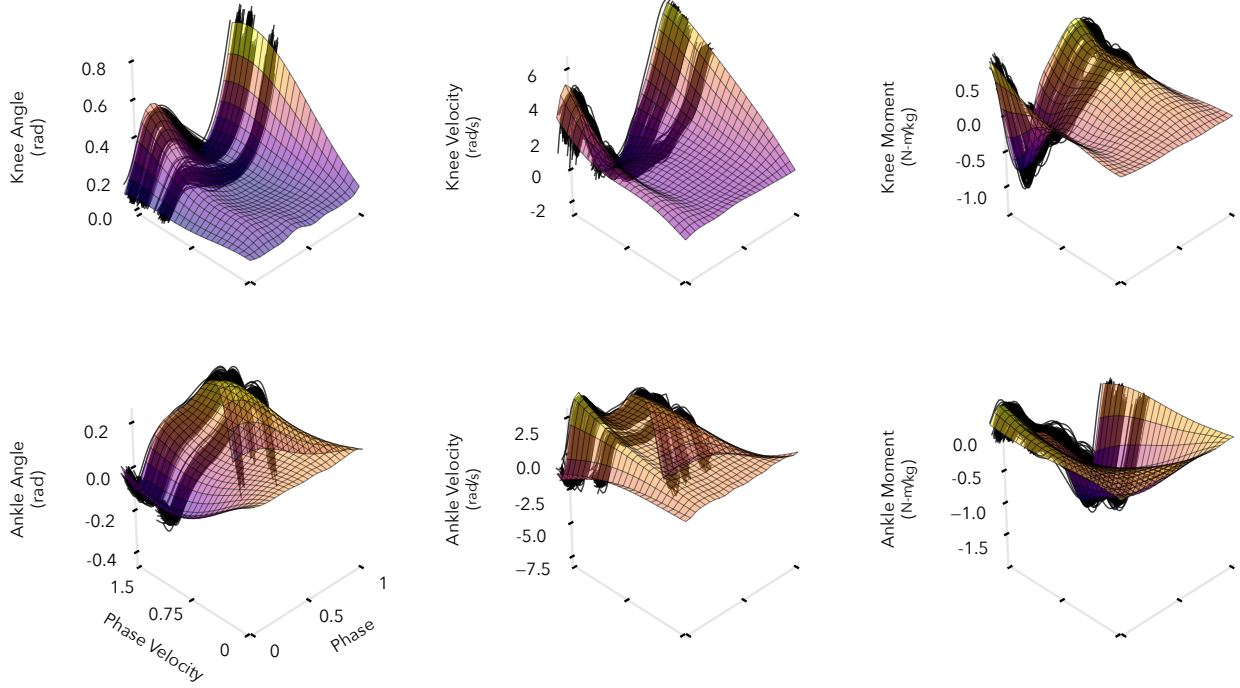
$$R_t = \text{blkdiag} \left(\text{GP}_{\sigma^2}^{\theta_h}(\phi_t), \text{GP}_{\sigma^2}^{\theta_k}(\phi_t), \text{GP}_{\sigma^2}^{\theta_a}(\phi_t), \text{GP}_{\sigma^2}^{d\theta_h/d\phi}(\phi_t), \text{GP}_{\sigma^2}^{d\theta_k/d\phi}(\phi_t), \text{GP}_{\sigma^2}^{d\theta_a/d\phi}(\phi_t) \right) \quad (9.19)$$

Due to the linearity of Gaussian processes and differentiation, we can analytically obtain derivatives required by eq. (9.17) using the methods provided by Solak et al. [2003].

Finally, we reset the state distribution at heel strike to

$$\hat{x}_0 = \begin{bmatrix} 0 \\ 1/T_{n-1} \end{bmatrix}, \quad \Sigma_0 = 0_{2 \times 2}, \quad (9.20)$$

where T_{n-1} is the duration of the previous stance.



9.3.2 Control Surfaces

We use the mean estimates of the phase ϕ and phase velocity $\dot{\phi}$ as the inputs into learned control surfaces that provide the desired knee and ankle angles, velocities, and feed-forward torques (Fig. 9.3). The final desired torques applied to the prosthesis are then given by

$$\tau_d = k_p(\theta_d(\phi, \dot{\phi}) - \theta) + k_d(\dot{\theta}_d(\phi, \dot{\phi}) - \dot{\theta}) + \tau_{ff}(\phi, \dot{\phi}), \quad (9.21)$$

where θ_d , $\dot{\theta}_d$, and τ_{ff} are the learned control surfaces as functions of the estimated phase and phase velocity, k_p and k_d are proportional and derivative gains, and θ and $\dot{\theta}$ are the actual joint angle and velocity.

We learned the control surfaces θ_d , $\dot{\theta}_d$ and τ_{ff} , by regressing the gait data provided by Moore et al. [2015] for several subjects walking at three speeds, 0.8, 1.2, and 1.6 m/s. We were able to learn the control surfaces using the data from nine subjects. For each subject, we split the gait data into individual stance phases and extracted the knee and ankle angles, velocities, and joint torques. We also assumed that during each stance, the actual phase increased linearly from zero at heel strike to one at toe off and the phase velocity during stance was constant and equal to $1/T$, where T is the duration of stance. We again used sparse GP regression with the FITC approximation to

Figure 9.3: Examples of learned control surfaces. We fit the surfaces to gait data from Moore et al. [2015]. This data includes information for three speeds, 0.8, 1.2, and 1.6 m/s, which are shown as the clustered trajectories in the above panels. For an automatic transition to standing, the surfaces are additionally fit to virtual data that causes the joint angles to approach 5 deg, the velocities to approach 0 deg/s, and the joint torques to approach 0 N-m as the phase velocity goes to zero.

regress the knee and ankle angles, velocities, and torques versus the phase and phase velocity. In this case, we used 100 active vectors to approximate each GP.

The gait data spans the whole range of phases ($[0, 1]$) but not the whole range of physiological phase velocities, as the gait speed only varies between 0.8 and 1.6 m/s. To ensure the control surfaces generate smooth behaviors at slower speeds and when standing still ($\dot{\phi} = 0$), we additionally trained the GPs on a grid spanning $\phi \in [0, 1]$ and $\dot{\phi} \in [0, \min(\dot{\phi}_{\text{data set}})]$ with *virtual* training values derived from interpolating between the average trajectory at 0.8 m/s and desired values at $\dot{\phi} = 0$. When $\dot{\phi} = 0$, the desired joint angles, velocities and torques were set to 5 deg, 0 deg/s, and 0 N-m, respectively, thereby creating a smooth transition to a standing mode. Figure 9.3 shows examples of the resulting control surfaces derived from one subject's data.

9.3.3 Experimental Protocol

We evaluated the naturalness of gait and the robustness of our proposed controller in experiments conducted with seven able-bodied subjects, and an amputee subject. We additionally present data from an experienced user of the prosthesis (first author of paper), whose gait characteristics induced a different response from the prosthesis. All subjects provided informed consent to IRB-approved protocols. The amputee subject used the powered prosthesis prototype through his personal socket adapter, as shown in fig. 9.4, while able-bodied subjects used a shortened version of the prosthesis attached to an L-shaped able-bodied adapter. All subjects had at least six hours of prior practice walking on the prosthesis. The able-bodied subjects walked without assistance from handrails, while the amputee subject used the handrails for balance.

We compared our proposed control method to a stance control based on a neuromuscular model of human neurophysiology [Thatte et al., 2018] and to finite state impedance control [Lawson et al., 2014]. For these controllers, we generated parameter sets by fitting control parameters to the same nine subjects' gait data used to generate the control surfaces described in section 9.3.2. For neuromuscular control, we used the black-box CMA-ES optimizer [Hansen, 2006] to fit the control parameters as described in [Thatte et al., 2018]. For impedance control, we used robust RANSAC linear regression [Fischler and Bolles, 1981] to fit the stiffness, damping, and angle offset parameters within the three discrete phases of stance. The transition between phases 1 and 2 was based on the knee angle crossing a threshold, while the transition between phases 2 and 3 was based

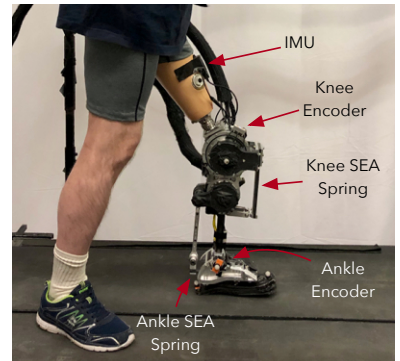


Figure 9.4: Powered prosthesis attached to amputee's personal socket

on the ankle angle crossing a threshold. We set these thresholds so that 95% of steps in the gait data transition through all three phases. Prior to beginning the experiments, subjects walked with each of the nine control surfaces (parameter sets) for each controller and indicated their preferred settings. All three stance control strategies were paired with the same swing control strategy, in which minimum jerk trajectories for the knee and ankle are generated at toe-off and tracked with PD-feedback combined with a model-based feed forward term as in [Lenzi et al., 2014b]. In total, we conducted four experiments:

(1) A test of the ability of each control strategy to reproduce a normal walking gait pattern. Able-bodied subjects walked without the use of handrails 0.8 m/s and the amputee subject used the handrails and walked at 0.6 m/s. All subjects walked with their preferred parameters for each controller for one minute. We compared the resulting prosthesis knee and ankle kinematics and kinetics to able-bodied gait data [Bovi et al., 2011] to determine the naturalness of gait.

(2) A comparison of the robustness of the three controllers to ground height disturbances. We simulated a ground disturbance by having subjects step on 3 cm blocks placed on the treadmill. We tested the controllers in a random order in an ABCCBA sequence. In each trial, the subjects stepped on blocks 20 times. We recorded the number of falls, defined as instances when subject needed support from either the handrails or a ceiling mounted harness to regain balance.

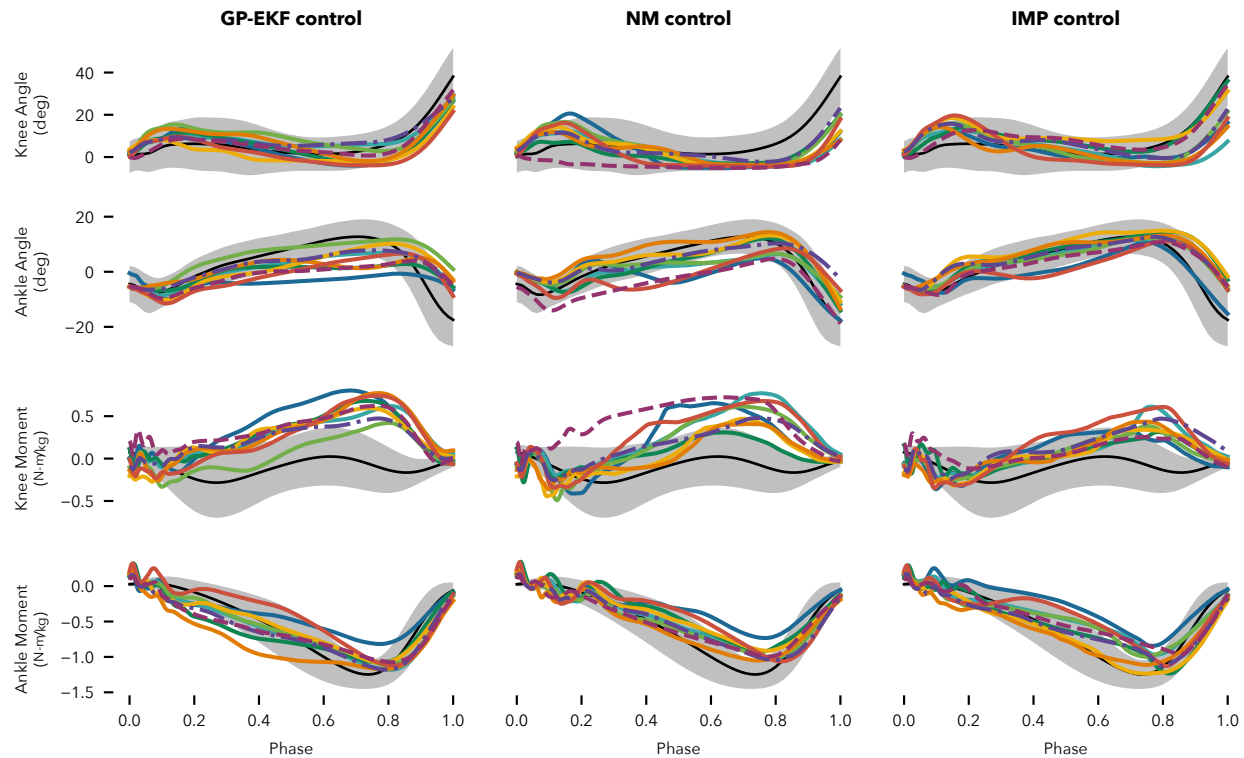
(3) A test of the adaptability of the phase estimate. To test the adaptability, we had subjects use the proposed GP-EKF control while the treadmill speed varied sinusoidally between 0.4 and 1.2 m/s with a 20 s period. We compared the phase and phase velocity estimates given by the EKF filter to the true phase, assumed to increase linearly from zero at heel strike to one at toe off, and the true phase velocity, assumed to equal $1/T_n$, where T_n is the duration of the current stance. As a baseline, we compared the EKF to time-based phase and phase velocity estimates, which assume the duration of the current stance will be the same as the previous stance, resulting in the phase and phase velocity estimates

$$\phi_{\text{time based}} = t_n / T_{n-1} \quad (9.22)$$

$$\dot{\phi}_{\text{time based}} = 1 / T_{n-1}, \quad (9.23)$$

where t_n is the time after heel-strike of the current stance and T_{n-1} is the duration of the last stance.

(4) Finally, a test of the ability of the GP-EKF control to respond to sudden treadmill stops. If the subject stops his or her gait, then



the phase estimate should stabilize and the phase velocity should trend towards zero. The corresponding desired joint angles should approach 5 deg as shown in fig. 9.3.

We assess significant differences between conditions via the two-sided paired Wilcoxon signed rank test [Gibbons and Chakraborti, 2011]. Experienced subject data was not considered for significance testing.

9.4 Results

9.4.1 Ability to Reproduce Normal Walking

Figure 9.5 shows the average knee and ankle angles as well as the corresponding joint moments generated by the prosthesis controllers during undisturbed walking at 0.8 m/s. All three control strategies produce knee angle trajectories that are similar to the able-bodied data (first row). The neuromuscular (NM) control, however, seems to suffer more from knee over extension during mid-stance and less knee flexion at the end of stance. For some able-bodied subjects, and to a substantial degree for the amputee subject, the knee over-

Figure 9.5: Ability to reproduce normal walking characteristics. Average knee angle (row 1), ankle angle (row 2), knee moment (row 3), and ankle moment (row 4) for the GP-EKF controller (column 1), neuromuscular controller (column 2), and impedance controller (column 3). Black traces and gray shaded areas show the mean and two standard deviations for very slow human walking data (from [Bovi et al., 2011]). Colored lines show individual subject data. Amputee gait data indicated by dashed lines and experienced user data indicated by dash-dot lines.

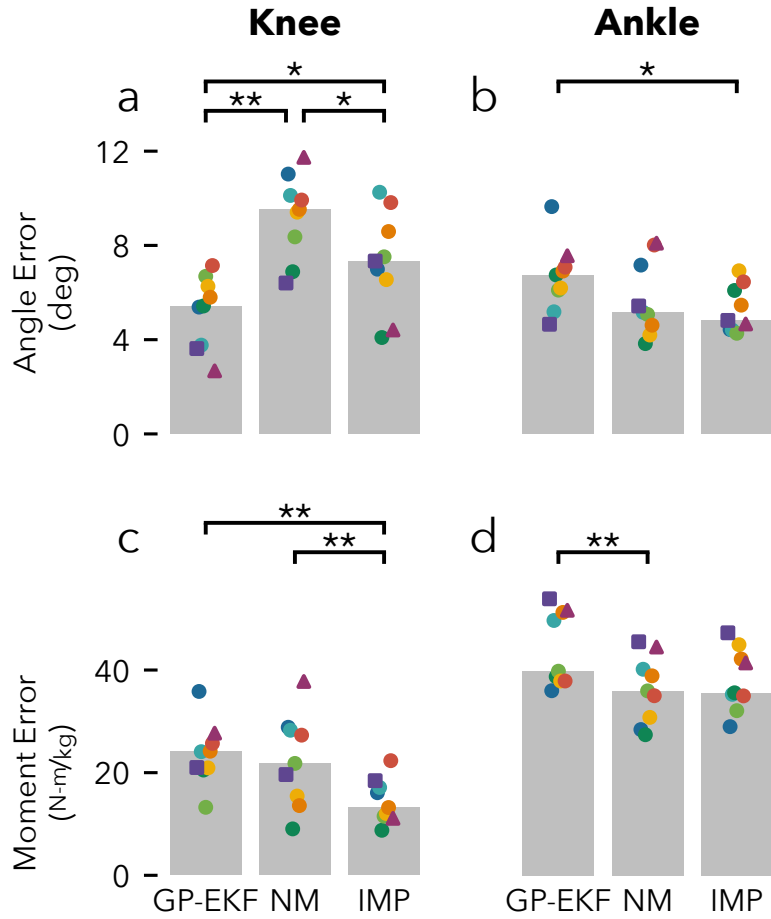


Figure 9.6: Average kinematic (a,b) and kinetic (c,d) errors produced by the three different controllers compared to able-bodied data. GP-EKF produces significantly more natural knee angles than NM or IMP control, but slightly less natural ankle angles and joint torques. Grey bars show median of subject data, circle markers indicate able-bodied subject data, triangle markers indicate amputee data, and square markers indicate experienced able-bodied user data.
 $* : p < 0.05$, $** : p < 0.01$.

extension causes the joint to engage the mechanical hard-stop on the prosthesis. This triggers a sudden rise in knee torque. Figure 9.6a summarizes the root-mean-squared (RMS) error between the mean able-bodied knee kinematics and the median knee kinematics of each subject. The GP-EKF control strategy produces significantly more kinematically natural knee angle trajectories, whereas the NM control produces the least kinematically natural knee trajectories.

The second row of fig. 9.5 shows the average ankle trajectories for each control strategy. In this case, the GP-EKF control produced the least accurate trajectories. As shown in fig. 9.6b, this trend reached statistical significance compared to impedance (IMP) control, which produced the most natural ankle angle trajectories. The unnaturalness of the GP-EKF control ankle trajectories is largely due to (1) a lack of plantar flexion in the push-off phase and (2) a lack of dorsiflexion during mid-stance for 3 out of 8 subjects, who all chose the

same control surface set.

Finally, the third and fourth row of fig. 9.5 show the knee and ankle moments for the three controllers. IMP control produced the most natural knee moments by a significant margin (fig. 9.6c), whereas the GP-EKF and NM controllers performed comparably. Although the GP-EKF control produced the least natural ankle moments, the absolute differences were small (fig. 9.6d).

9.4.2 Robustness to Ground Height Disturbances

Figure 9.7 shows the number of times able-bodied subjects fell with each control strategy when stepping on blocks. Subjects fell significantly more often with the IMP control compared to either the GP-EKF or NM controllers. However, when using the neuromuscular control the experienced user fell 8 times, more than any other subject in any condition.

9.4.3 Adaptability of Phase Estimate

The adaptability of the phase estimate was tested by sinusoidally varying the treadmill speed during walking. Figure 9.8 shows the average RMS errors of the EKF-based phase estimate and time-based phase estimate compared to the ground-truth phase obtained in hindsight. For all subjects, the EKF tracked the true phase significantly more accurately than did the time-based phase estimate.

For a more specific example, fig. 9.9 shows the phase estimates during the treadmill speed variation experiment for a single subject. Because the initial conditions of the EKF and the time-based phase estimates are identical (compare eq. (9.20) and eq. (9.23)), the phase estimates are similar in early stance. As the treadmill speed changes from one step to the next, the time-based phase estimate diverges significantly from the true phase. The EKF, on the other hand, is able to recover to the true phase towards the end of stance and more accurately predicts the toeoff event.

9.4.4 Response to Sudden Treadmill Stops

Finally, fig. 9.10 shows the phase (a), and phase velocity (b) estimates when the treadmill is suddenly stopped halfway through the stance phase. The EKF phase estimates (solid lines) reflect the fact that the gait cycle has halted, as they do not continue to progress to one. Moreover, when the treadmill stops, the knee (c) and ankle angles (d) approach 5 deg as desired for standing (compare fig. 9.3). In contrast, the time-based phase estimates (dashed lines in panels (a) and (b)) continue at their initial rate, with the phase reaching one.

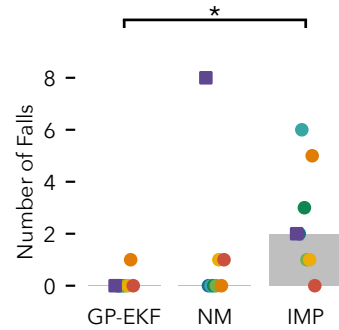


Figure 9.7: Robustness to ground height disturbances. Number of falls accrued for each controller during ground height disturbance trials. GP-EKF control significantly reduced the number of falls compared to IMP control.

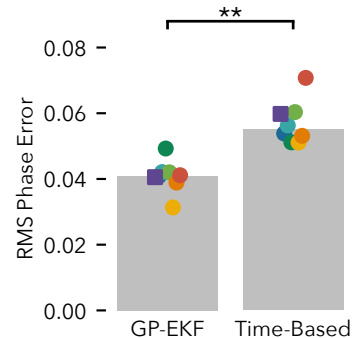


Figure 9.8: Adaptability of phase estimate. Mean phase error of EKF versus time-based phase estimation when walking with sinusoidally varying treadmill speed. The EKF significantly improves phase tracking compared to the time-based estimate.

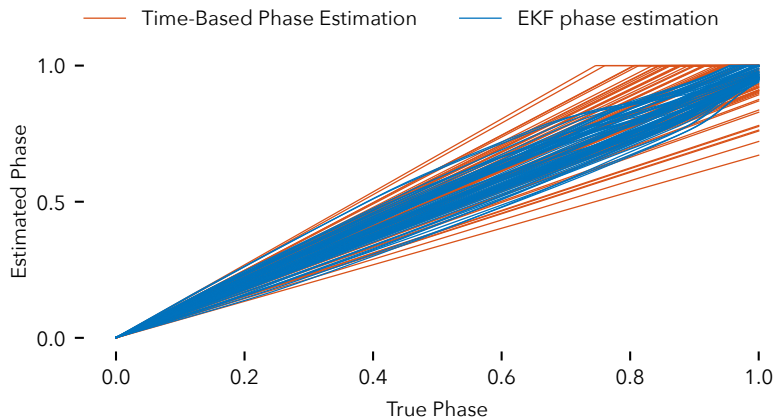


Figure 9.9: Example of EKF-based phase estimation (red) versus time-based phase estimation (blue) for one subject. Due to step-to-step speed variations caused by the sinusoidally varying treadmill speed, the time based phase estimation accrues significant errors. In contrast, the EKF-based phase estimate is able to respond to changes in gait within the gait cycle, thus reducing phase estimation errors.

9.5 Discussion

We proposed a new approach for the control of powered transfemoral prostheses. The approach uses a robust estimate of the gait phase derived from an EKF that integrates multiple sensor measurements to determine the desired knee and ankle angles, velocities and torques from trained control surfaces. The proposed approach improved knee kinematics over NM and IMP control, matched NM control and improves upon IMP control in terms of gait robustness to ground height disturbances, and adapted the phase estimate to both gradual and abrupt changes in speed more quickly than a time-based phase estimate.

We believe the robustness improvements of the proposed GP-EKF control scheme and the NM control over IMP control stem from the smoothness of the phase estimation in these two controllers. In NM control, the phase estimation is implicit and encoded in the internal states of virtual muscles, which are modulated by musculoskeletal dynamics and reflexes. In the proposed control presented here, the EKF directly infers a robust estimate of phase from multiple measurements. In either case, the resulting control commands are smooth and do not normally change abruptly from one moment to the next. In contrast, IMP control splits the stance phase into three discrete phases that are triggered by joint angle thresholds. Consequently, in the ground height disturbance experiments, subjects were occasionally caught off-guard by unexpected transitions, triggered by abnormal kinematics when stepping on a block, which then caused large, sudden changes in torque. Unexpected phase transitions between the mid-stance and late-stance phases were especially consequential, as in the late-stance phase, knee torque trends towards zero to allow for

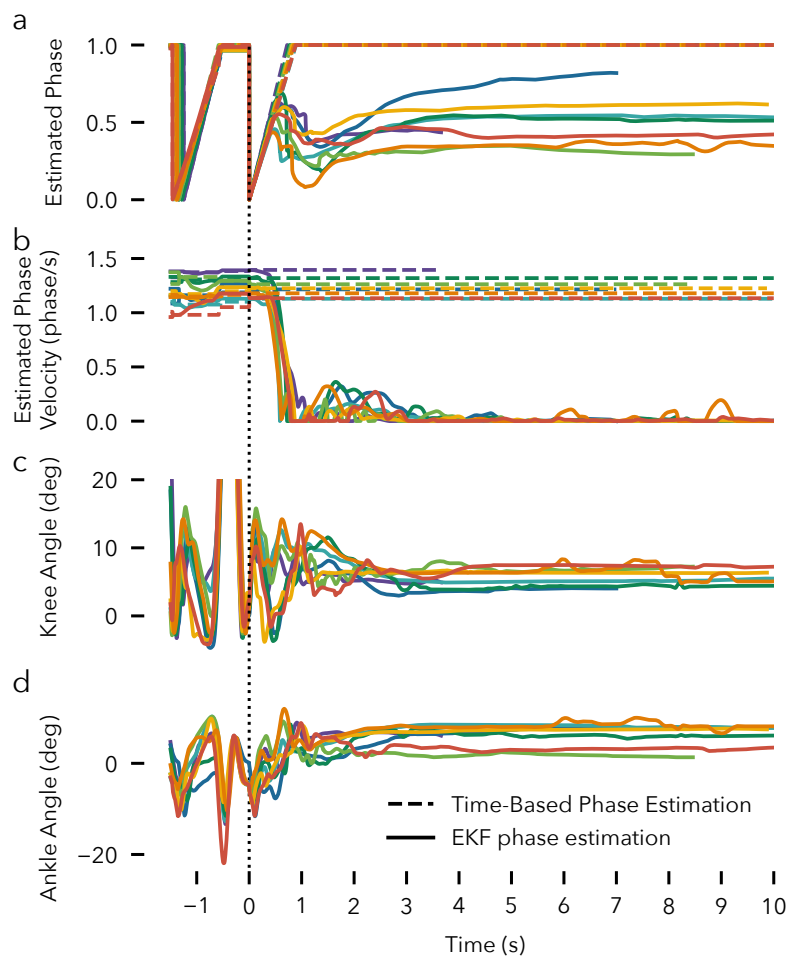


Figure 9.10: Response to sudden treadmill stops. Estimated phase (a) and phase velocity (b), and the measured knee (c) and ankle (d) angles when the treadmill is suddenly stopped half way through stance. When gait stops, the EKF-estimated phase stabilizes to a constant value (solid traces), phase velocity falls to zero, and the joint angles approach 5 deg as desired by the control surfaces (compare fig. 9.3). The time-based phase estimate fails to respond (dashed lines). Vertical black dotted line indicates heel strike of final stance phase.

passive knee flexion, while the ankle plantarflexes. If a user's center of mass is positioned incorrectly, this combination of joint torques can cause a sudden collapse of the knee, which was the cause for many of the observed falls with IMP control.

NM control too can result in unexpected falls due to incorrect phase estimation. The experienced user fell a total of eight times when stepping on blocks with the NM control (see square marker fig. 9.7). These falls were the result of a modelled reflex that reduces knee extensor muscle stimulation in late stance in proportion to ankle plantarflexion, thereby allowing for passive knee flexion leading into swing. In contrast to less experienced subjects, the experienced user was able to control the knee over-extension during stance and achieve more normal knee flexion in late-stance during normal walking (see fig. 9.5 row 1, column 2). However, this in-

creased knee flexion during normal walking may have increased the prosthesis' susceptibility to premature knee collapse when disturbed. While the modeled neuromuscular reflexes seem to work well during steady-state walking and during disturbed walking for inexperienced users, the large increase in falls for the experienced user, exposes the difficulty of relying on heuristic reflexes to obtain robust control across a range of gait characteristics. In contrast, the proposed EKF approach takes a principled approach to phase estimation and thus resulted in the fewest falls.

Some improvements can be made in the implementation of the proposed control. The normal walking experiments show that the ankle trajectories produced by the GP-EKF control are less natural than those produced by NM or IMP control (see fig. 9.6b). The GP-EKF ankle trajectories in fig. 9.5 show that peak ankle flexion is achieved later in stance and that the ankle insufficiently plantarflexes at toeoff. There were two reasons for these issues. First, in hindsight the cutoff between stance and swing in the data used to train the control surfaces was set too early in the gait cycle. Second, the ankle impedance, especially in the push off phase was too low. Figure 9.11 shows the trajectories for all 9 control surfaces with corrected control surfaces and with increased ankle stiffness (k_p eq. (9.21)) that is roughly double of that used for the previous results. These changes substantially improve the ankle kinematics in the push off phase.

However, increasing the ankle stiffness throughout stance may make an overly ridged controller that does not comply to rough terrain. Recent research has investigated how impedance varies continuously throughout gait [Lee et al., 2016]. These results could be used to parameterize impedance as a function of phase. Taking this step could help improve the naturalness of the knee and ankle torques produced by the GP-EKF controller, which currently trail those produced by the NM and IMP controllers (see figs. 9.6c and d).

There are several other avenues for future research to expand the proposed control approach. First, we only used prosthesis joint angles and velocities for the observation models. It is worth investigating if additional measurements such as ground reaction forces, accelerations, and EMG signals improve the state estimate. Second, we used a simple, two-state model to represent the entirety of the coupled human-prosthesis state during stance. Adding additional state variables may help capture important behaviors such as balance recovery actions taken by the upper body. To this end, dimensionality reduction techniques could help identify better state representations from gait data. New state representations need to satisfy two constraints that our current model satisfies: (1) The evolution of the state needs to approximately abide by some Markov dynamics model so

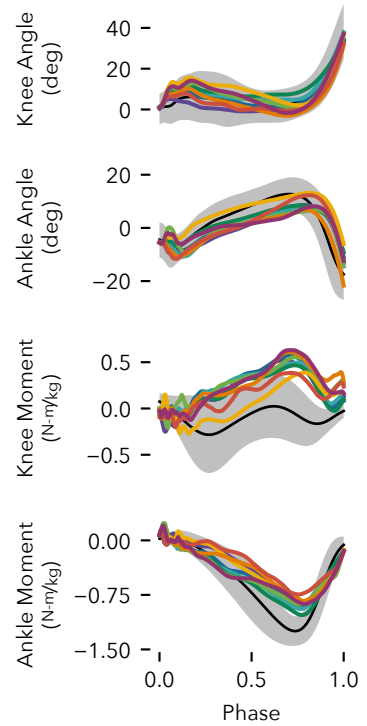


Figure 9.11: GP-EKF phase control with fixed control surfaces and increased ankle impedance.

we can perform the predict step of the EKF (eqs. (9.11) and (9.12)).

(2) The evolution of state throughout stance should be knowable in hindsight after a step is completed so that the observation model can be learned online. Finally, with more advanced state and observation models, more advanced forms of state estimation may be necessary, including unscented Kalman filters or particle filters such as the one proposed by Dhir et al. [2018], which allows for continuous gait phase estimation using discrete heel and toe contact sensors.

10

Conclusion

This thesis began with the goal of improving the robustness of gait with transfemoral prostheses so as to reduce amputees risk of falling and increase their quality of life. Towards the goal, we started by comparing a proposed neuromuscular strategy for transfemoral prosthesis control to the established impedance control strategy. We attempted to make this comparison as objective as possible by building a robotic prosthesis capable of accurate torque control (chapter 3) and developing methods that use the user's feedback to select prosthesis control parameters (chapter 6). While the experiment comparing neuromuscular and impedance control did not confirm our hypothesis that neuromuscular control would lead to a significant reduction in falls (chapter 7), it did clarify the importance of state estimation in prosthesis control. This insight motivated the development of swing and stance controllers with state estimation via an extended Kalman filter (EKF) at the core of each (chapters 8 and 9). The proposed swing controller uses an EKF to estimate the position and orientation of the hip, which is then used to plan knee and ankle swing trajectories that avoid trips. The proposed stance controller uses an EKF to estimate the phase of stance. This phase estimate made the gait robust to ground height disturbances and able to adapt to both sudden and gradual changes in gait speed.

In performing the work in this thesis we have assembled a substantial amount of practical knowledge and suggestions for future research in the field. First, when it comes to prosthesis design, in hindsight, we likely put too much emphasis on prosthesis performance, and did not consider enough whether the user would actually be able to make use of the performance. In our experiments, able-bodied users wore the prosthesis through a L-shaped adapter (fig. 3.12) while amputees used their own socket (fig. 9.4). Both of these interfaces are not very secure, limiting the weight of the prosthesis and the dynamism of movements. Therefore, while our prosthesis design, at 6 kg, is of comparable mass to a biological limb, it is too heavy to

use comfortably for an extended period of time. Future prosthesis designs should be mindful of the constraint the interface places on useable torque and comfortable prosthesis mass. One solution for a transfemoral prostheses design for research purposes, which achieves high performance and keeps weight to a minimum, is to create a knee-ankle prosthesis emulator, similar to the ankle emulator created by Caputo and Collins [2013].

A difficulty faced when conducting this research was the substantial time spent implementing various controllers from the literature on our transfemoral prosthesis prototype. This challenge would be significantly reduced with standardization of the interface between the low-level controls and the mid level behavior controls. Standardizing this interface would more easily allow researchers to share code and try controllers on their own prostheses. Standardizing the hardware design too would also help in this effort and substantially decrease the time required to make progress in this field. The recent development of open source knee and ankle prosthesis designs should help significantly in this regard [Azocar et al., 2018].

Another development that would help decrease the time required to improve prosthesis controls is better simulations of amputees and their interactions with hardware. In chapter 5, we presented results from one such simulation that predicted more falls for impedance control than neuromuscular control when walking on rough ground. Based on the experimental results on the real prosthesis that we have gathered, it seems these simulations may have overstated the potential improvement in gait robustness offered by neuromuscular control. We may be able to improve these sorts of simulations to better predict real-world results in two ways. First, through the course of conducting this research, we have recorded large amounts of motion capture data of users walking on the prosthesis. This data could be used to improve the neuromuscular model to better capture actual subject responses to disturbances. Second, in chapter 5, we used the shooting method and a genetic algorithm [Hansen, 2006] to optimize the control parameters of the prosthesis. These optimizations often required days to converge on a solution. In future work, more advanced simulation/trajectory optimization techniques should be considered such as using symbolic differentiation to derive the change in the control action with respect to parameters and using nonlinear programming and collocation to directly solve the optimal control problem [Hargraves and Paris, 1987].

Finally, an innovation provided by the planning-based swing control described in sections 8.5 to 8.8 is that it considers environmental information in real-time within the mid-level controller. The environmental information directly and precisely impacts the trajectories

that are generated during swing. In contrast, previous prosthesis controllers that have considered environmental information have primarily only done so at the high-level for gait mode recognition (see section 2.3). These high-level strategies switch the mid-level control parameters within a discrete set of options. Similarly, the phase-based stance control described in sections 8.5 to 8.8 can use information in real-time from multiple sensors on the prosthesis to reason about the appropriate control action to take. These results motivate further research into mid-level controllers that can directly act on more sources of information. Doing so may allow prostheses to adapt more appropriately to the user and environment and take a broader range of actions that are better suited to the specific situation at hand.

Bibliography

- Navid Aghasadeghi, Huihua Zhao, Levi J Hargrove, Aaron D Ames, Eric J Perreault, and Timothy Bretl. Learning impedance controller parameters for lower-limb prostheses. In *Intelligent robots and systems (IROS), 2013 IEEE/RSJ international conference on*, pages 4268–4274. IEEE, 2013.
- Riad Akrou, Marc Schoenauer, Michèle Sebag, and Jean-Christophe Souplet. Programming by feedback. In *International Conference on Machine Learning*, number 32, pages 1503–1511. JMLR.org, 2014.
- Brian DO Anderson and John B Moore. Optimal filtering. *Englewood Cliffs*, 21:22–95, 1979.
- Brenna D Argall, Sonia Chernova, Manuela Veloso, and Brett Browning. A survey of robot learning from demonstration. *Robotics and autonomous systems*, 57(5):469–483, 2009.
- Samuel K Au and Hugh M Herr. Powered ankle-foot prosthesis. *IEEE Robotics & Automation Magazine*, 15(3):52–59, 2008.
- Samuel K Au, Jeff Weber, and Hugh Herr. Biomechanical design of a powered ankle-foot prosthesis. In *2007 IEEE 10th International conference on rehabilitation robotics*, pages 298–303. IEEE, 2007.
- Vahid Azimi, Tony Shu, Huihua Zhao, Rachel Gehlhar, Dan Simon, and Aaron D Ames. Model-based adaptive control of transfemoral prostheses: Theory, simulation, and experiments. *IEEE Transactions on Systems, Man, and Cybernetics: Systems*, 2019.
- Alejandro F Azocar, Luke M Mooney, Levi J Hargrove, and Elliott J Rouse. Design and characterization of an open-source robotic leg prosthesis. In *2018 7th IEEE International Conference on Biomedical Robotics and Biomechatronics (Biorob)*, pages 111–118. IEEE, 2018.
- Ryan D Bellman, Matthew A Holgate, and Thomas G Sugar. Sparky 3: Design of an active robotic ankle prosthesis with two actuated degrees of freedom using regenerative kinetics. In *2008 2nd IEEE*

RAS & EMBS International Conference on Biomedical Robotics and Biomechatronics, pages 511–516. IEEE, 2008.

Gabriele Bovi, Marco Rabuffetti, Paolo Mazzoleni, and Maurizio Ferrarin. A multiple-task gait analysis approach: kinematic, kinetic and emg reference data for healthy young and adult subjects. *Gait & posture*, 33(1):6–13, 2011.

Eric Brochu, Nando D Freitas, and Abhijeet Ghosh. Active preference learning with discrete choice data. In *Advances in neural information processing systems*, pages 409–416, 2008.

Benjamin J Brown, Charlie G Crone, and Christopher E Attinger. Amputation in the diabetic to maximize function. In *Seminars in Vascular Surgery*, volume 25, pages 115–121. Elsevier, 2012.

Frank L Buczek and PETER R Cavanagh. Stance phase knee and ankle kinematics and kinetics during level and downhill running. *Med Sci Sports Exerc*, 22(5):669–677, 1990.

Roberto Calandra, Nakul Gopalan, André Seyfarth, Jan Peters, and Marc Peter Deisenroth. Bayesian gait optimization for bipedal locomotion. In *International Conference on Learning and Intelligent Optimization*, pages 274–290. Springer, 2014.

Joshua M Caputo and Steven H Collins. An experimental robotic testbed for accelerated development of ankle prostheses. In *Robotics and automation (ICRA), 2013 IEEE international conference on*, pages 2645–2650. IEEE, 2013.

Joshua M Caputo, Peter G Adamczyk, and Steven H Collins. Informing ankle-foot prosthesis prescription through haptic emulation of candidate devices. In *2015 IEEE International Conference on Robotics and Automation (ICRA)*, pages 6445–6450. IEEE, 2015.

Wei Chu and Zoubin Ghahramani. Preference learning with gaussian processes. In *Proceedings of the 22nd international conference on Machine learning*, pages 137–144. ACM, 2005.

Steve Collins, Andy Ruina, Russ Tedrake, and Martijn Wisse. Efficient bipedal robots based on passive-dynamic walkers. *Science*, 307(5712):1082–1085, 2005.

Ruta Desai and Hartmut Geyer. Robust swing leg placement under large disturbances. In *Robotics and Biomimetics (ROBIO), 2012 IEEE International Conference on*, pages 265–270. IEEE, 2012.

Neil Dhir, Houman Dallali, Evandro Maicon Ficanha, Guilherme Aramizo Ribeiro, and Mo Rastgaar. Locomotion envelopes

for adaptive control of powered ankle prostheses. In *2018 IEEE International Conference on Robotics and Automation (ICRA)*, pages 1488–1495. IEEE, 2018.

Edsger W Dijkstra. A note on two problems in connexion with graphs. *Numerische mathematik*, 1(1):269–271, 1959.

Max Donath. *Proportional EMG control for above knee prostheses*. PhD thesis, Massachusetts Institute of Technology, 1974.

Lin Du, Fan Zhang, Ming Liu, and He Huang. Toward design of an environment-aware adaptive locomotion-mode-recognition system. *IEEE Transactions on Biomedical Engineering*, 59(10):2716–2725, 2012.

Ran Duan, Shuangyue Yu, Guang Yue, Richard Foulds, Chen Feng, Yingli Tian, and Hao Su. Real-time robust 3d plane extraction for wearable robot perception and control. In *2018 Design of Medical Devices Conference*, pages Voo1To6A003–Voo1To6A003. American Society of Mechanical Engineers, 2018.

Michael F Eilenberg, Hartmut Geyer, and Hugh Herr. Control of a powered ankle-foot prosthesis based on a neuromuscular model. *Neural Systems and Rehabilitation Engineering, IEEE Transactions on*, 18(2):164–173, 2010.

Janice J Eng, David A Winter, and Aftab E Patla. Strategies for recovery from a trip in early and late swing during human walking. *Experimental Brain Research*, 102(2):339–349, 1994.

Martin A Fischler and Robert C Bolles. Random sample consensus: a paradigm for model fitting with applications to image analysis and automated cartography. *Communications of the ACM*, 24(6):381–395, 1981.

Woodie C Flowers. Use of an amputee-computer interactive facility in above-knee prosthesis research. In *Proceedings of the 1974 annual conference-Volume 1*, pages 335–339. ACM, 1974.

Christiane Gauthier-Gagnon, Marie-Claude Grisé, and Diane Potvin. Enabling factors related to prosthetic use by people with transtibial and transfemoral amputation. *Archives of physical medicine and rehabilitation*, 80(6):706–713, 1999.

Hartmut Geyer and Hugh Herr. A muscle-reflex model that encodes principles of legged mechanics produces human walking dynamics and muscle activities. *IEEE Transactions on neural systems and rehabilitation engineering*, 18(3):263–273, 2010.

Hartmut Geyer, Andre Seyfarth, and Reinhard Blickhan. Positive force feedback in bouncing gaits? *Proceedings of the Royal Society of London B: Biological Sciences*, 270(1529):2173–2183, 2003.

Hartmut Geyer, Andre Seyfarth, and Reinhard Blickhan. Compliant leg behaviour explains basic dynamics of walking and running. *Proceedings of the Royal Society of London B: Biological Sciences*, 273(1603):2861–2867, 2006.

Jean Dickinson Gibbons and Subhabrata Chakraborti. Nonparametric statistical inference. In *International encyclopedia of statistical science*, pages 977–979. Springer, 2011.

Claire C Gordon, Thomas Churchill, Charles E Clauser, Bruce Bradtmiller, and John T McConville. Anthropometric survey of us army personnel: methods and summary statistics 1988. Technical report, Anthropology Research Project Inc Yellow Springs OH, 1989.

Max Gordon, Nitish Thatte, and Hartmut Geyer. Online learning for proactive obstacle avoidance with powered transfemoral prostheses. In *Robotics and Automation (ICRA), 2019 IEEE International Conference on*. IEEE, 2019.

Mark D Grabiner, Timothy J Koh, Thomas M Lundin, and Dennis W Jahnigen. Kinematics of recovery from a stumble. *Journal of gerontology*, 48(3):M97–M102, 1993.

Robert D Gregg, Tommaso Lenzi, Levi J Hargrove, and Jonathon W Sensinger. Virtual constraint control of a powered prosthetic leg: From simulation to experiments with transfemoral amputees. *IEEE Transactions on Robotics*, 30(6):1455–1471, 2014.

DL Grimes, WC Flowers, and M Donath. Feasibility of an active control scheme for above knee prostheses. *Journal of Biomechanical Engineering*, 99(4):215–221, 1977.

Donald Lee Grimes. *An active multi-mode above knee prosthesis controller*. PhD thesis, Massachusetts Institute of Technology, 1979.

Jesse A Grimes. *ATRIAS 1.0 & 2.1: enabling agile biped locomotion with a template-driven approach to robot design*. PhD thesis, Oregon State University, 2013.

Michael Günther and Hanns Ruder. Synthesis of two-dimensional human walking: a test of the λ -model. *Biological cybernetics*, 89(2):89–106, 2003.

Nachi Gupta and Raphael Hauser. Kalman filtering with equality and inequality state constraints. *arXiv preprint arXiv:0709.2791*, 2007.

Kevin H Ha, Huseyin Atakan Varol, and Michael Goldfarb. Volitional control of a prosthetic knee using surface electromyography. *IEEE Transactions on Biomedical Engineering*, 58(1):144–151, 2011.

Nikolaus Hansen. The cma evolution strategy: a comparing review. In *Towards a new evolutionary computation*, pages 75–102. Springer, 2006.

Charles R Hargraves and Stephen W Paris. Direct trajectory optimization using nonlinear programming and collocation. *Journal of Guidance, Control, and Dynamics*, 10(4):338–342, 1987.

Levi J Hargrove, Aaron J Young, Ann M Simon, Nicholas P Fey, Robert D Lipschutz, Suzanne B Finucane, Elizabeth G Halsne, Kimberly A Ingraham, and Todd A Kuiken. Intuitive control of a powered prosthetic leg during ambulation: a randomized clinical trial. *JAMA*, 313(22):2244–2252, 2015.

Philipp Hennig and Christian J Schuler. Entropy search for information-efficient global optimization. *The Journal of Machine Learning Research*, 13(1):1809–1837, 2012.

José Miguel Hernández-Lobato, Matthew W Hoffman, and Zoubin Ghahramani. Predictive entropy search for efficient global optimization of black-box functions. In *Advances in Neural Information Processing Systems*, pages 918–926, 2014.

Hugh M. Herr and Alena M. Grabowski. Bionic ankle–foot prosthesis normalizes walking gait for persons with leg amputation. *Proceedings of the Royal Society of London B: Biological Sciences*, 279(1728):457–464, 2011. ISSN 0962-8452. DOI: 10.1098/rspb.2011.1194. URL <http://rspb.royalsocietypublishing.org/content/279/1728/457>.

A Vo Hill. The heat of shortening and the dynamic constants of muscle. *Proceedings of the Royal Society of London B: Biological Sciences*, 126(843):136–195, 1938.

Joseph K Hitt, Ryan Bellman, Matthew Holgate, Thomas G Sugar, and Kevin W Hollander. The sparky (spring ankle with regenerative kinetics) project: Design and analysis of a robotic transtibial prosthesis with regenerative kinetics. In *ASME 2007 International Design Engineering Technical Conferences and Computers and Information in Engineering Conference*, pages 1587–1596. American Society of Mechanical Engineers, 2007.

Matthew A Holgate, Joseph K Hitt, Ryan D Bellman, Thomas G Sugar, and Kevin W Hollander. The sparky (spring ankle with regenerative kinetics) project: Choosing a dc motor based actuation

- method. In *2008 2nd IEEE RAS & EMBS International Conference on Biomedical Robotics and Biomechatronics*, pages 163–168. IEEE, 2008.
- Neil Houlsby, Ferenc Huszar, Zoubin Ghahramani, and Jose M Hernández-lobato. Collaborative gaussian processes for preference learning. In *Advances in Neural Information Processing Systems*, pages 2096–2104, 2012.
- He Huang, Todd A Kuiken, Robert D Lipschutz, et al. A strategy for identifying locomotion modes using surface electromyography. *IEEE Transactions on Biomedical Engineering*, 56(1):65–73, 2009.
- He Huang, Fan Zhang, Levi J Hargrove, Zhi Dou, Daniel R Rogers, and Kevin B Englehart. Continuous locomotion-mode identification for prosthetic legs based on neuromuscular-mechanical fusion. *IEEE Transactions on Biomedical Engineering*, 58(10):2867–2875, 2011.
- He Huang, Dustin L Crouch, Ming Liu, Gregory S Sawicki, and Ding Wang. A cyber expert system for auto-tuning powered prosthesis impedance control parameters. *Annals of Biomedical Engineering*, 44(5):1613–1624, 2016.
- CL Hubley and RP Wells. A work-energy approach to determine individual joint contributions to vertical jump performance. *European Journal of Applied Physiology and Occupational Physiology*, 50(2):247–254, 1983.
- Amanda M Huff, Brian E Lawson, and Michael Goldfarb. A running controller for a powered transfemoral prosthesis. In *2012 Annual International Conference of the IEEE Engineering in Medicine and Biology Society*, pages 4168–4171. IEEE, 2012.
- Sonja MHJ Jaegers, J Hans Arendzen, and Henry J de Jongh. Prosthetic gait of unilateral transfemoral amputees: a kinematic study. *Archives of physical medicine and rehabilitation*, 76(8):736–743, 1995.
- Ashesh Jain, Brian Wojcik, Thorsten Joachims, and Ashutosh Saxena. Learning trajectory preferences for manipulators via iterative improvement. In *Advances in neural information processing systems*, pages 575–583, 2013.
- Jennifer L Johansson, Delsey M Sherrill, Patrick O Riley, Paolo Bonato, and Hugh Herr. A clinical comparison of variable-damping and mechanically passive prosthetic knee devices. *American journal of physical medicine & rehabilitation*, 84(8):563–575, 2005.
- Donald R Jones, Matthias Schonlau, and William J Welch. Efficient global optimization of expensive black-box functions. *Journal of Global Optimization*, 13(4):455–492, 1998.

Shuuji Kajita, Fumio Kanehiro, Kenji Kaneko, Kazuhito Yokoi, and Hirohisa Hirukawa. The 3d linear inverted pendulum mode: A simple modeling for a biped walking pattern generation. In *Intelligent Robots and Systems, 2001. Proceedings. 2001 IEEE/RSJ International Conference on*, volume 1, pages 239–246. IEEE, 2001.

W Bradley Knox and Peter Stone. Interactively shaping agents via human reinforcement: The tamer framework. In *Proceedings of the fifth international conference on Knowledge capture*, pages 9–16. ACM, 2009.

W Bradley Knox, Peter Stone, and Cynthia Breazeal. Training a robot via human feedback: A case study. In *Social Robotics*, pages 460–470. Springer, 2013.

Jonathan Ko and Dieter Fox. Gp-bayesfilters: Bayesian filtering using gaussian process prediction and observation models. *Autonomous Robots*, 27(1):75–90, 2009.

Nili Eliana Krausz, Tommaso Lenzi, and Levi J Hargrove. Depth sensing for improved control of lower limb prostheses. *IEEE Transactions on Biomedical Engineering*, 62(11):2576–2587, 2015.

J Kulkarni, S Wright, C Toole, J Morris, and R Hirons. Falls in patients with lower limb amputations: prevalence and contributing factors. *Physiotherapy*, 2(82):130–136, 1996.

Brian E Lawson, H Atakan Varol, Frank Sup, and Michael Goldfarb. Stumble detection and classification for an intelligent transfemoral prosthesis. In *Engineering in medicine and biology society (EMBC), 2010 annual international conference of the IEEE*, pages 511–514. IEEE, 2010.

Brian E Lawson, Jason Mitchell, Don Truex, Amanda Shultz, Elissa Ledoux, and Michael Goldfarb. A robotic leg prosthesis: Design, control, and implementation. *IEEE Robotics & Automation Magazine*, 21(4):70–81, 2014.

Brian Edward Lawson, Huseyin Atakan Varol, Amanda Huff, Erdem Erdemir, and Michael Goldfarb. Control of stair ascent and descent with a powered transfemoral prosthesis. *IEEE Transactions on Neural Systems and Rehabilitation Engineering*, 21(3):466–473, 2013.

Hyunglae Lee, Elliott J Rouse, and Hermano Igo Krebs. Summary of human ankle mechanical impedance during walking. *IEEE journal of translational engineering in health and medicine*, 4:1–7, 2016.

T Lenzi, LJ Hargrove, and JW Sensinger. Minimum jerk swing control allows variable cadence in powered transfemoral prostheses. In

Conference Proceedings IEEE Engineering in Medicine and Biology Society, pages 2492–2495, 2014a.

Tommaso Lenzi, Levi Hargrove, and Jonathon Sensinger. Speed-adaptation mechanism: Robotic prostheses can actively regulate joint torque. *IEEE Robotics & Automation Magazine*, 21(4):94–107, 2014b.

David R Lide. *CRC handbook of chemistry and physics*, volume 85. CRC press, 2004.

Ming Liu, Fan Zhang, Philip Datseris, and He Helen Huang. Improving finite state impedance control of active-transfemoral prosthesis using dempster-shafer based state transition rules. *Journal of Intelligent & Robotic Systems*, 76(3-4):461–474, 2014.

Ming Liu, Ding Wang, and He Helen Huang. Development of an environment-aware locomotion mode recognition system for powered lower limb prostheses. *IEEE Transactions on Neural Systems and Rehabilitation Engineering*, 24(4):434–443, 2016.

Jared Markowitz, Pavitra Krishnaswamy, Michael F Eilenberg, Ken Endo, Chris Barnhart, and Hugh Herr. Speed adaptation in a powered transtibial prosthesis controlled with a neuromuscular model. *Philosophical Transactions of the Royal Society of London B: Biological Sciences*, 366(1570):1621–1631, 2011.

Ernesto C Martinez-Villalpando, Jeff Weber, Grant Elliott, and Hugh Herr. Design of an agonist-antagonist active knee prosthesis. In *2008 2nd IEEE RAS & EMBS International Conference on Biomedical Robotics and Biomechatronics*, pages 529–534. IEEE, 2008.

Ernesto C Martinez-Villalpando, Luke Mooney, Grant Elliott, and Hugh Herr. Antagonistic active knee prosthesis. a metabolic cost of walking comparison with a variable-damping prosthetic knee. In *2011 Annual International Conference of the IEEE Engineering in Medicine and Biology Society*, pages 8519–8522. IEEE, 2011.

Yerzhan Massalin, Madina Abdurakhmanova, and Huseyin Atakan Varol. User-independent intent recognition for lower-limb prostheses using depth sensing. *IEEE Transactions on Biomedical Engineering*, 2017.

Tad McGeer. Passive dynamic walking. *The international journal of robotics research*, 9(2):62–82, 1990.

Michael D McKay, Richard J Beckman, and William J Conover. A comparison of three methods for selecting values of input variables

- in the analysis of output from a computer code. *Technometrics*, 42(1):55–61, 2000.
- R McNeill Alexander. Energetics and optimization of human walking and running: the 2000 raymond pearl memorial lecture. *American journal of human biology*, 14(5):641–648, 2002.
- William C Miller, Mark Speechley, and Barry Deathe. The prevalence and risk factors of falling and fear of falling among lower extremity amputees. *Archives of physical medicine and rehabilitation*, 82(8):1031–1037, 2001.
- Simon Mochon and Thomas A McMahon. Ballistic walking. *Journal of biomechanics*, 13(1):49–57, 1980.
- Jason K Moore, Sandra K Hnat, and Antonie J van den Bogert. An elaborate data set on human gait and the effect of mechanical perturbations. *PeerJ*, 3:e918, 2015.
- Maxon Motor. Mason ec-4pole, Apr 2016a. URL http://www.maxonmotorusa.com/medias/sys_master/root/8821066268702/16-274-en.pdf.
- Maxon Motor. Maxon flat motor, Apr 2016b. URL http://www.maxonmotorusa.com/medias/sys_master/root/8821068005406/16-304-en.pdf.
- Sylvie Nadeau, Bradford J McFadyen, and Francine Malouin. Frontal and sagittal plane analyses of the stair climbing task in healthy adults aged over 40 years: what are the challenges compared to level walking? *Clinical Biomechanics*, 18(10):950–959, 2003.
- Andrew Y Ng, Stuart J Russell, et al. Algorithms for inverse reinforcement learning. In *ICML*, pages 663–670, 2000.
- Tom F Novacheck. The biomechanics of running. *Gait & posture*, 7(1):77–95, 1998.
- Aftab E Patla and Stephen D Prentice. The role of active forces and intersegmental dynamics in the control of limb trajectory over obstacles during locomotion in humans. *Experimental Brain Research*, 106(3):499–504, 1995.
- Jacquelin Perry and Judith M Burnfield. *Gait analysis: normal and pathological function*. Slack Thorofare, NJ, 2 edition, 2010.
- Mirjam Pijnappels, Maarten F Bobbert, and Jaap H van Dieën. How early reactions in the support limb contribute to balance recovery after tripping. *Journal of biomechanics*, 38(3):627–634, 2005.

Patrick M Pilarski, Michael R Dawson, Thomas Degris, Farbod

Fahimi, Jason P Carey, and Richard S Sutton. Online human training of a myoelectric prosthesis controller via actor-critic reinforcement learning. In *2011 IEEE International Conference on Rehabilitation Robotics*, pages 1–7. IEEE, 2011.

Dean A Pomerleau. Efficient training of artificial neural networks for autonomous navigation. *Neural Computation*, 3(1):88–97, 1991.

Gill A Pratt and Matthew M Williamson. Series elastic actuators. In *Intelligent Robots and Systems 95.'Human Robot Interaction and Cooperative Robots', Proceedings. 1995 IEEE/RSJ International Conference on*, volume 1, pages 399–406. IEEE, 1995.

Jerry Pratt and Ben Krupp. Design of a bipedal walking robot. In *SPIE defense and security symposium*, pages 69621F–69621F. International Society for Optics and Photonics, 2008.

Jerry Pratt, John Carff, Sergey Drakunov, and Ambarish Goswami. Capture point: A step toward humanoid push recovery. In *2006 6th IEEE-RAS international conference on humanoid robots*, pages 200–207. IEEE, 2006.

David Quintero, Dario J Villarreal, and Robert D Gregg. Preliminary experiments with a unified controller for a powered knee-ankle prosthetic leg across walking speeds. In *Intelligent Robots and Systems (IROS), 2016 IEEE/RSJ International Conference on*, pages 5427–5433. IEEE, 2016.

Marc H Raibert. *Legged robots that balance*. MIT press, 1986.

Jack Alan Rall. Energetic aspects of skeletal muscle contraction: implications of fiber types. *Exercise and sport sciences reviews*, 13: 33–74, 1984.

Carl Edward Rasmussen. Gaussian processes in machine learning. In *Advanced lectures on machine learning*, pages 63–71. Springer, 2004.

Nathan Ratliff, Matt Zucker, J Andrew Bagnell, and Siddhartha Srinivasa. Chomp: Gradient optimization techniques for efficient motion planning. In *Robotics and Automation, 2009. ICRA'09. IEEE International Conference on*, pages 489–494. IEEE, 2009.

Nathan D Ratliff, J Andrew Bagnell, and Martin A Zinkevich. Maximum margin planning. In *Proceedings of the 23rd international conference on Machine learning*, pages 729–736. ACM, 2006.

Nathan D Ratliff, J Andrew Bagnell, and Martin A Zinkevich. (online) subgradient methods for structured prediction. *Robotics Institute*, page 55, 2007.

Siavash Rezazadeh, David Quintero, Nikhil Divekar, and Robert D Gregg. A phase variable approach to volitional control of powered knee-ankle prostheses. In *2018 IEEE/RSJ International Conference on Intelligent Robots and Systems (IROS)*, pages 2292–2298. IEEE, 2018.

Stephen N Robinovitch, Fabio Feldman, Yijian Yang, Rebecca Schonnop, Pet Ming Leung, Thiago Sarraf, Joanie Sims-Gould, and Marie Loughin. Video capture of the circumstances of falls in elderly people residing in long-term care: an observational study. *The Lancet*, 381(9860):47–54, 2013.

David William Robinson. *Design and analysis of series elasticity in closed-loop actuator force control*. PhD thesis, Massachusetts Institute of Technology, 2000.

Elliott J Rouse, Luke M Mooney, and Hugh M Herr. Clutchable series-elastic actuator: Implications for prosthetic knee design. *The International Journal of Robotics Research*, page 0278364914545673, 2014.

Elliott J Rouse, Nathan C Villagary-Carski, Robert W Emerson, and Hugh M Herr. Design and testing of a bionic dancing prosthesis. *PloS one*, 10(8):e0135148, 2015.

Gregory S Sawicki, Cara L Lewis, and Daniel P Ferris. It pays to have a spring in your step. *Exercise and sport sciences reviews*, 37(3):130, 2009.

Glauco Garcia Scandaroli, Geovany Araújo Borges, João Yoshiyuki Ishihara, Marco Henrique Terra, Adson Ferreira da Rocha, and Francisco Assis de Oliveira Nascimento. Estimation of foot orientation with respect to ground for an above knee robotic prosthesis. In *Intelligent robots and systems, 2009. IROS 2009. IEEE/RSJ international conference on*, pages 1112–1117. IEEE, 2009.

Stefan Schaal. Is imitation learning the route to humanoid robots? *Trends in cognitive sciences*, 3(6):233–242, 1999.

Alexander Schepelmann, Michael D Taylor, and Hartmut Geyer. Development of a testbed for robotic neuromuscular controllers. *Robotics: Science and Systems VIII*, 4, 2012.

Stephen H Scott and David A Winter. Biomechanical model of the human foot: kinematics and kinetics during the stance phase of walking. *Journal of biomechanics*, 26(9):1091–1104, 1993.

Fabrizio Sergi, Dino Accoto, Giorgio Carpino, Nevio Luigi Tagliamonte, and Eugenio Guglielmelli. Design and characterization of

- a compact rotary series elastic actuator for knee assistance during overground walking. In *Biomedical Robotics and Biomechatronics (BioRob), 2012 4th IEEE RAS & EMBS International Conference on*, pages 1931–1936. IEEE, 2012.
- Andre Seyfarth, Hartmut Geyer, Michael Günther, and Reinhard Blickhan. A movement criterion for running. *Journal of biomechanics*, 35(5):649–655, 2002.
- Camila Shirota, Ann M Simon, and Todd A Kuiken. Recovery strategy identification throughout swing phase using kinematic data from the tripped leg. In *Engineering in Medicine and Biology Society (EMBC), 2014 36th Annual International Conference of the IEEE*, pages 6199–6202. IEEE, 2014.
- Camila Shirota, Ann M Simon, and Todd A Kuiken. Transfemoral amputee recovery strategies following trips to their sound and prosthesis sides throughout swing phase. *Journal of neuroengineering and rehabilitation*, 12(1):79, 2015.
- Amanda H Shultz, Jason E Mitchell, Don Truex, Brian E Lawson, Elissa Ledoux, and Michael Goldfarb. A walking controller for a powered ankle prosthesis. In *2014 36th Annual International Conference of the IEEE Engineering in Medicine and Biology Society*, pages 6203–6206. IEEE, 2014.
- Amanda H Shultz, Brian E Lawson, and Michael Goldfarb. Running with a powered knee and ankle prosthesis. *IEEE Transactions on Neural Systems and Rehabilitation Engineering*, 23(3):403–412, 2015.
- Amanda H Shultz, Brian E Lawson, and Michael Goldfarb. Variable cadence walking and ground adaptive standing with a powered ankle prosthesis. *IEEE Transactions on Neural Systems and Rehabilitation Engineering*, 24(4):495–505, 2016.
- Ann M Simon, Kimberly A Ingraham, Nicholas P Fey, Suzanne B Finucane, Robert D Lipschutz, Aaron J Young, and Levi J Hargrove. Configuring a powered knee and ankle prosthesis for transfemoral amputees within five specific ambulation modes. *PloS one*, 9(6):e99387, 2014.
- Edward Snelson and Zoubin Ghahramani. Local and global sparse gaussian process approximations. In *Artificial Intelligence and Statistics*, pages 524–531, 2007.
- E Solak, R Murray Smith, WE Leithead, D Leith, and CE Rasmussen. Derivative observations in gaussian process models of dynamic systems. *Advances in Neural Information Processing Systems*, pages 1057–1064, 2003.

Seungmoon Song and Hartmut Geyer. Generalization of a muscle-reflex control model to 3d walking. In *2013 35th Annual International Conference of the IEEE Engineering in Medicine and Biology Society (EMBC)*, pages 7463–7466. IEEE, 2013.

Seungmoon Song and Hartmut Geyer. A neural circuitry that emphasizes spinal feedback generates diverse behaviours of human locomotion. *The Journal of physiology*, 593(16):3493–3511, 2015.

Seungmoon Song, Ruta Desai, and Hartmut Geyer. Integration of an adaptive swing control into a neuromuscular human walking model. In *2013 35th Annual International Conference of the IEEE Engineering in Medicine and Biology Society (EMBC)*, pages 4915–4918. IEEE, 2013.

JA Spanias, AM Simon, SB Finucane, EJ Perreault, and LJ Hargrove. Online adaptive neural control of a robotic lower limb prosthesis. *Journal of neural engineering*, 15(1):016015, 2018.

Frank Sup, Amit Bohara, and Michael Goldfarb. Design and control of a powered knee and ankle prosthesis. In *Robotics and Automation, 2007 IEEE International Conference on*, pages 4134–4139. IEEE, 2007.

Frank Sup, Amit Bohara, and Michael Goldfarb. Design and control of a powered transfemoral prosthesis. *The International journal of robotics research*, 27(2):263–273, 2008.

Frank Sup, Huseyin Atakan Varol, Jason Mitchell, Thomas J Withrow, and Michael Goldfarb. Preliminary evaluations of a self-contained anthropomorphic transfemoral prosthesis. *IEEE/ASME Transactions on mechatronics*, 14(6):667–676, 2009.

Frank Sup, Huseyin Atakan Varol, and Michael Goldfarb. Upslope walking with a powered knee and ankle prosthesis: initial results with an amputee subject. *IEEE Transactions on Neural Systems and Rehabilitation Engineering*, 19(1):71–78, 2011.

Matthew Tesch, Jeff Schneider, and Howie Choset. Using response surfaces and expected improvement to optimize snake robot gait parameters. In *2011 IEEE/RSJ International Conference on Intelligent Robots and Systems*, pages 1069–1074. IEEE, 2011.

Nitish Thatte and Hartmut Geyer. Towards local reflexive control of a powered transfemoral prosthesis for robust amputee push and trip recovery. In *2014 IEEE/RSJ International Conference on Intelligent Robots and Systems*, pages 2069–2074. IEEE, 2014.

Nitish Thatte and Hartmut Geyer. Toward balance recovery with leg prostheses using neuromuscular model control. *IEEE Transactions on Biomedical Engineering*, 63(5):904–913, 2016.

Nitish Thatte, Helei Duan, and Hartmut Geyer. A sample-efficient black-box optimizer to train policies for human-in-the-loop systems with user preferences. *IEEE Robotics and Automation Letters*, 2017.

Nitish Thatte, Helei Duan, and Hartmut Geyer. A method for online optimization of lower limb assistive devices with high dimensional parameter spaces. In *Robotics and Automation (ICRA), 2018 IEEE International Conference on*. IEEE, 2018.

Nitish Thatte, Nandagopal Srinivasan, and Hartmut Geyer. Real-time reactive trip avoidance for powered transfemoral prostheses. In *Proceedings of Robotics: Science and Systems*, 2019.

Miles A Townsend. Biped gait stabilization via foot placement. *Journal of biomechanics*, 18(1):21–38, 1985.

Brian R Umberger, Karin GM Gerritsen, and Philip E Martin. A model of human muscle energy expenditure. *Computer methods in biomechanics and biomedical engineering*, 6(2):99–111, 2003.

Heike Vallery, Rainer Burgkart, Cornelia Hartmann, Jürgen Mitternacht, Robert Riener, and Martin Buss. Complementary limb motion estimation for the control of active knee prostheses. *Biomedizinische Technik/Biomedical Engineering*, 56(1):45–51, 2011.

Vassilios G Vardaxis, Paul Allard, Régis Lachance, and Morris Duhaime. Classification of able-bodied gait using 3-d muscle powers. *Human Movement Science*, 17(1):121–136, 1998.

Huseyin Atakan Varol, Frank Sup, and Michael Goldfarb. Powered sit-to-stand and assistive stand-to-sit framework for a powered transfemoral prosthesis. In *2009 IEEE International Conference on Rehabilitation Robotics*, pages 645–651. IEEE, 2009.

Huseyin Atakan Varol, Frank Sup, and Michael Goldfarb. Multiclass real-time intent recognition of a powered lower limb prosthesis. *IEEE Transactions on Biomedical Engineering*, 57(3):542–551, 2010.

Jing Wang, Oliver A Kannape, and Hugh M Herr. Proportional emg control of ankle plantar flexion in a powered transtibial prosthesis. In *Rehabilitation Robotics (ICORR), 2013 IEEE International Conference on*, pages 1–5. IEEE, 2013.

RL Waters, Jacqueline Perry, DANIEL Antonelli, and Helen Hislop. Energy cost of walking of amputees: the influence of level of amputation. *J Bone Joint Surg Am*, 58(1):42–46, 1976.

- Yue Wen, Ming Liu, Jennie Si, and He Helen Huang. Adaptive control of powered transfemoral prostheses based on adaptive dynamic programming. In *Engineering in Medicine and Biology Society (EMBC), 2016 IEEE 38th Annual International Conference of the*, pages 5071–5074. IEEE, 2016.
- Yue Wen, Jennie Si, Andrea Brandt, Xiang Gao, and He Huang. Online reinforcement learning control for the personalization of a robotic knee prosthesis. *IEEE transactions on cybernetics*, 2019.
- Michael James Whitley. *Maximum Absolute and Relative Joint Torques during Recovery from a Simulated Trip*. PhD thesis, Virginia Polytechnic Institute and State University, 2008.
- Christopher KI Williams and Carl Edward Rasmussen. *Gaussian processes for machine learning*, volume 2. MIT Press Cambridge, MA, 2006.
- Aaron Wilson, Alan Fern, and Prasad Tadepalli. A bayesian approach for policy learning from trajectory preference queries. In *Advances in neural information processing systems*, pages 1133–1141, 2012.
- David A Winter. *Biomechanics and motor control of human movement*. John Wiley & Sons, 2009.
- Albert Wu and Hartmut Geyer. The 3-d spring–mass model reveals a time-based deadbeat control for highly robust running and steering in uncertain environments. *IEEE Transactions on Robotics*, 29(5):1114–1124, 2013.
- Huasen Wu and Xin Liu. Double thompson sampling for dueling bandits. In *Advances in Neural Information Processing Systems*, pages 649–657, 2016.
- Sai-Kit Wu, Garrett Waycaster, and Xiangrong Shen. Electromyography-based control of active above-knee prostheses. *Control Engineering Practice*, 19(8):875–882, 2011.
- Linfeng Xu and X Rong Li. Estimation and filtering of gaussian variables with linear inequality constraints. In *Information Fusion (FUSION), 2010 13th Conference on*, pages 1–6. IEEE, 2010.
- Tingfang Yan, Yuxiang Sun, Tingting Liu, Chi-Hong Chcung, and Max Qing-Hu Meng. A locomotion recognition system using depth images. In *2018 IEEE International Conference on Robotics and Automation (ICRA)*, pages 6766–6772. IEEE, 2018.
- KangKang Yin, Kevin Loken, and Michiel Van de Panne. Simbicon: Simple biped locomotion control. In *ACM Transactions on Graphics (TOG)*, volume 26, page 105. ACM, 2007.

Aaron J Young, Ann M Simon, Nicholas P Fey, and Levi J Hargrove.

Intent recognition in a powered lower limb prosthesis using time history information. *Annals of biomedical engineering*, 42(3):631–641, 2014a.

Aaron J Young, Ann M Simon, and Levi J Hargrove. A training method for locomotion mode prediction using powered lower limb prostheses. *IEEE Transactions on Neural Systems and Rehabilitation Engineering*, 22(3):671–677, 2014b.

Yisong Yue, Josef Broder, Robert Kleinberg, and Thorsten Joachims.

The k-armed dueling bandits problem. *Journal of Computer and System Sciences*, 78(5):1538–1556, 2012.

Fan Zhang, Susan E D’Andrea, Michael J Nunnery, Steven M Kay, and He Huang. Towards design of a stumble detection system for artificial legs. *IEEE Transactions on Neural Systems and Rehabilitation Engineering*, 19(5):567–577, 2011a.

Fan Zhang, Zheng Fang, Ming Liu, and He Huang. Preliminary design of a terrain recognition system. In *Engineering in medicine and biology society, EMBC, 2011 annual international conference of the IEEE*, pages 5452–5455. IEEE, 2011b.

Juanjuan Zhang, Pieter Fiers, Kirby A Witte, Rachel W Jackson, Katherine L Poggensee, Christopher G Atkeson, and Steven H Collins. Human-in-the-loop optimization of exoskeleton assistance during walking. *Science*, 356(6344):1280–1284, 2017.

Huihua Zhao, Jonathan Horn, Jacob Reher, Victor Paredes, and Aaron D Ames. First steps toward translating robotic walking to prostheses: a nonlinear optimization based control approach. *Autonomous Robots*, pages 1–18, 2016.

Brian D Ziebart, Andrew L Maas, J Andrew Bagnell, and Anind K Dey. Human behavior modeling with maximum entropy inverse optimal control. In *AAAI Spring Symposium: Human Behavior Modeling*, page 92, 2009.

Kathryn Ziegler-Graham, Ellen J MacKenzie, Patti L Ephraim, Thomas G Travison, and Ron Brookmeyer. Estimating the prevalence of limb loss in the united states: 2005 to 2050. *Archives of physical medicine and rehabilitation*, 89(3):422–429, 2008.